

GP4 - Modeling and experimental investigation of the microstructural changes in the interdiffusion zone of leadfree solder joints

Participants

N. Moelans¹, J. Botsis², R. Čička³, J. Cugnoni², A. Durga¹, M. Danielewski⁴, J. Drápala⁵, M. Drienovský³, Y. Guan¹, P. Harcuba⁵, J. Janczak-Rusch⁴, J. Janovec³, A.A. Kodentsov⁶, A. Kroupa⁷, P. Kubíček⁵, A. Kudyba^{8,9}, M. Maleki², *M. Martinkovič*³, R. Novakovic¹⁰, R. Nowak^{8,9}, M. Ožvold³, M. Pawelkiewicz⁴, K. Pietrzak^{8,9}, K. Pocisková Dimová³, L. Rízeková Trnková³, *M. Scheller*⁴, E. Sienicki^{8,9}, N. Sobczak^{8,9}, K.K. Sosnowska⁴, *G. Toporek*⁴, V. Vodárek⁵, A. Zemanová⁷, *P. Zolliker*⁴

¹ KU Leuven, Department of Metallurgy and Materials Engineering, Belgium

² LMAF-EPFL-Lausanne, The Switzerland

³ Slovak University of Technology, Faculty of Materials Science and Technology, Trnava, Slovakia

⁴ Empa, Swiss Federal Laboratories for Materials Science and Technology

⁵ Vysoká škola báňská – Technical University of Ostrava; Faculty of Metallurgy and Materials Engineering, Czech Republic

⁶ Laboratory of Materials and Interface Chemistry, Eindhoven University of Technology, The Netherlands

⁷ Institute of Physics of Materials, AS CR, Brno, Czech Republic

⁸ Foundry Research Institute, Krakow, Poland

⁹ Motor Transport Institute, Warsaw, Poland

¹⁰ NRC, Inst. for Energetics and Interphases (CNR-IENI), Genoa, Italy

1 Introduction

The main purpose of this group project was the development of theoretical models and simulation techniques that predict the microstructural changes in the interdiffusion zone in lead-free solder joints. Different modeling techniques such as the phase field method, finite element elastic and viscoplastic modeling and the CALPHAD-method were combined to describe processes at different length scales. The modeling was highly supported by experimental studies, such as diffusion couple and annealing experiments, phase structure and composition characterization, 3D microstructure characterization techniques and mechanical testing to obtain the needed information for the simulations on the sequence of phase formation, diffusion and phase stability properties and the mechanical behavior, and for validation of the modelling approaches. Different phenomena important in the life cycle of a solder joint have been considered, e.g. solidification of the solder, growth of the intermetallic layers and precipitates, Kirkendal voiding, and microstructural changes and viscoplastic deformation during loading.

Due to the complexity of the processes and to enhance the exchange of information between different participants, most of the work focused on the system Ag-Cu-Sn for which the thermodynamic, kinetic and mechanical properties have been studied extensively, amongst others in COST 531 [[REF071ps](#)]. The techniques

developed within this group project are however generally applicable to high-temperature lead-free solder alloys. Moreover, the effect of small additions of rare earth elements on the phase stabilities and microstructure as well as microstructure evolution in nanoparticle reinforced solders was studied.

In this part, a number of characterization and modelling techniques developed and/or applied within this group project are discussed. It is also discussed how information was exchanged between different groups and different research projects.

[07Ips] Ipsen, H.: *J. Mining and Metallurgy*, 2007, **43B**, 109-112.

Formatted: Indent: Left: 1 cm, First line: 0 cm

Formatted: Font: Bold

2 The kinetic study of interfacial growth of the Cu_6Sn_5 and Cu_3Sn intermetallic phases during the formation and service of the SnAgCu lead free solder joints

M. Pawelkiewicz, J. Janczak-Rusch, K.K. Sosnowska and M. Danielewski

Empa. Swiss Federal Laboratories for Materials Science and Technology, The Switzerland

The kinetics of the formation of Cu-Sn intermetallic compounds (IMCs) in the Sn-Ag-Cu ternary system was studied using diffusion multiple technique (DM) extended by reflow soldering experiments. In this way the kinetic rate constants and the respective activation energies of the Cu-Sn intermetallic phases (Cu_6Sn_5 , Cu_3Sn) compounds (IMCs) in the temperature range between 150-200°C were determined for the solid state (DM) and liquid state (reflow soldering) reactions.

The most important binary system from the point of view of the lead-free soldering is Cu-Sn. The metallurgical bond of the Cu-Sn system during soldering is created through the formation of the Cu-Sn IMC. The respective binary systems involving Ni and Ag were prepared in view of a general interest in Ni and Ag IMCs with Sn in the field of soldering. Even though main emphasis on Cu-Sn the results of the Ag-Sn system are also presented and the kinetic rate constants for Ag_3Sn are calculated as well. The results of Ni-Sn system are discussed elsewhere.

Diffusion multiple technique

The diffusion multiples (DM) technique is an extended version of the diffusion couple/triplet technique. It requires only a single sample to study several materials phenomena such as phase diagrams, diffusion coefficients, precipitation kinetics, etc. The diffusion multiple method [01Zha,05Zha,07Zha][01Zha,05Zha,07Zha,10Tho,07Zha,03Zha,05Cam] is used to create composition gradients and intermetallic phases through long-term annealing of metal/metal junctions of three or more phases or alloys below the melting point of the lowest melting compound. Technically the diffusion multiple is an assembly of three or more different material blocks brought into close interfacial contact by a hot isostatic pressing (HIP) process. Typically this treatment is done at elevated temperatures to speed up thermal interdiffusion, thus creating solid solution compositions and intermetallics compounds (IMCs). Since multiple interfaces are formed simultaneously, localized property measurements of a number of different compounds can easily be mapped and compared. This technique provides access to a number of compositions and compounds in parallel in a single experiment or sample specimen, allowing many properties to be studied systematically as a function of composition or phase structure [05Zho1][05Zho].

The design of the samples used in this work is presented in Figure 2.1. Four kinds of pure element metal rods were used: Cu, Ni, Ag and Sn with a rhombic cross section. The rhombic metal bars were placed inside a Ti cylinder, than sealed and subjected to a HIP treatment ($T = 210^\circ\text{C}$, $p = 180 \text{ MPa}$, 1h). Finally, the cylinder was cut into 2mm thick slices, which were isothermally annealed for 3, 30, 100 and 336h at 150, 180 and 200°C.

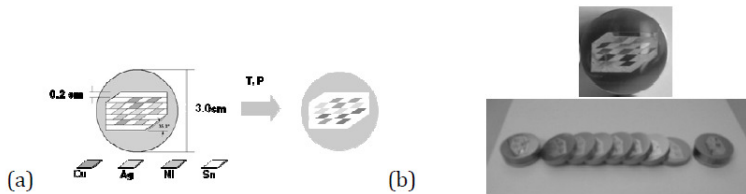


Fig. 2.1: Schema of the diffusion multiples sample fabrication, (a) HIP of the Ti cylinder and (b) Cutting the Ti cylinder into slices.

Reflow soldering technique

In reflow soldering, a mixture of solder and flux called solder paste is applied to every joint to be made in the assembly. Then, heat is applied by means of radiation, conduction or convection in a controlled environment. The assembly is heated and held at a temperature above the melting temperature of the solder for some time and then allowed to cool. During the process the solder melts and fills the gaps in between the work pieces and components thus forming the joint. The operational sequence of a reflow soldering processes (Figure 2.2) are applying the solder paste (solder and flux) to the joint, applying heat according to reflow profile curve and cooling to the room temperature. Reflow soldering samples were fabricated according to the schematic presented in Figure 2.2a. Two different kinds of commonly used lead free solder alloys (Sn-4,0Ag-0,5Cu (SAC405) and Sn-3,5Ag eutectic) and pure Sn metal were reflow soldered in a way to connect two metallic Cu plates. Reflow solder joints were prepared in a ZelFlow R04 reflow oven (LPKF Inc., USA). A complete list of the exact experimental conditions together with the materials used for the reflow soldered samples is shown in Table 2.1.

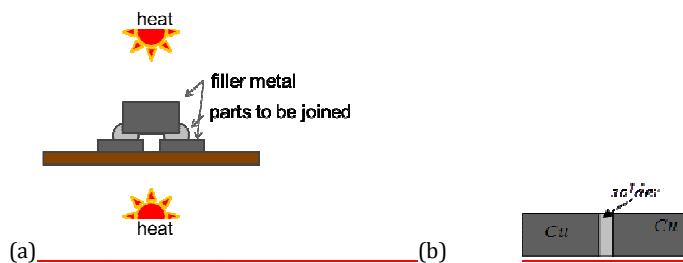


Fig. 2.2: Schematic diagram of reflow soldering (a) principle of reflow soldering and (b) scheme of the reflow sample.

Comment [AK1]: Is this figure copyright free, or do we have the rights to use it? Figure is replaced by figures without copyright.

Kinetic study

For kinetic study of interfacial Cu-Sn IMC, the DM and reflow soldered samples were diffusion multiple diffusion samples and reflow soldered samples were heat

treated in a Nabertherm LH 15/14 furnace at a constant temperature (150, 180 and 200°C) for different times (3, 30, 100, 176 and 336h). Annealed samples were polished and selectively etched. The microstructure of the cross sections was analyzed by scanning electron microscopy (FEI/Philips XL30 FEG-ESEM) in high-vacuum mode. Energy dispersive spectroscopy (EDS) was used for chemical analysis. The respective thicknesses of the IMC layers were measured on cross-sectional images obtained in back - scattered electron (BSE) mode of detection. The Image-Pro Plus software was used to integrate the area of Cu_3Sn and Cu_6Sn_5 IMC layers.

Table 2.1: EDS analysis of the samples at selected positions shown in Figure 2.3.

Position	Chemical composition, %at.			phase	Position	Chemical composition, %at.		Phase
	Cu	Sn	Ag			Cu	Sn	
A	75.7	24.3		Cu_3Sn	F	76.6	23.4	Cu_3Sn
B	55.6	44.4		Cu_6Sn_5	G	56.5	43.5	Cu_6Sn_5
C	54.9	45.1		Cu_6Sn_5	H	55.6	44.4	Cu_6Sn_5
D		35.9	64.1	Ag_3Sn	I	75.8	24.2	Cu_3Sn
E		100.0		Sn	J	100.0		Cu

The measurements of the interfacial IMCs thicknesses as a function of annealing time are presented in [11Paw,12Paw,11Paw1][11Paw, 11Paw1, 11Paw2, 11Paw3]. The parabolic rate constants, k_p , and activation energies, E_a , of the IMC growth are presented therein as well. The growth rate of the IMCs (DM samples) between Cu|Sn and Ag|Sn match a parabolic law. Obtained kinetic data are expressed by the following Arrhenius relations for:

Cu|Sn interface: $k_p^{\text{Cu}_3\text{Sn}}=1.7*10^{-11}\exp(-22.4\text{kJ}/\text{RT})$ and $k_p^{\text{Cu}_6\text{Sn}_5}=2.0*10^{-5}\exp(-69.3\text{kJ}/\text{RT})$;
 Ag|Sn interface: $k_p^{\text{Ag}_3\text{Sn}}=8.1*10^2\exp(-112.3\text{kJ}/\text{RT})$.

The growth rates of the IMCs for all reflow soldered samples are approximated by a parabolic law. The kinetic data obtained in this study can be described by the following Arrhenius relations:

Cu|Sn (reflow): $k_p^{\text{Cu}_3\text{Sn}}=2.4*10^{-9}\exp(-36.2\text{kJ}/\text{RT})$ and $k_p^{\text{Cu}_6\text{Sn}_5}=5.9*10^{-12}\exp(-9.07\text{kJ}/\text{RT})$;

Cu|Sn3.5Ag (reflow):

$k_p^{\text{Cu}_3\text{Sn}}=5.0*10^{-3}\exp(-94.5\text{kJ}/\text{RT})$ and $k_p^{\text{Cu}_6\text{Sn}_5}=6.2*10^{-11}\exp(-22.1\text{kJ}/\text{RT})$;

Cu|SAC405(reflow):

$k_p^{\text{Cu}_3\text{Sn}}=3.8*10^{-6}\exp(-67.4\text{kJ}/\text{RT})$ and $k_p^{\text{Cu}_6\text{Sn}_5}=2.3*10^{-7}\exp(-50.8\text{kJ}/\text{RT})$.

The microstructures of the solder phases show IMC islands inside the bulk solder. In the case of SAC405 and the Sn-Ag eutectic, two kinds of IMCs are visible: Cu_6Sn_5 originating from the reaction with the Cu substrate and Ag_3Sn which is already present in the bulk. Two IMCs: Cu_6Sn_5 and Cu_3Sn can be found at the bonding

interface for all fabricated joints as identified by SEM/EDS measurements. In the case of the joints obtained by HIP no formation of IMC in Sn bulk metal phases is expected nor was observed experimentally. The thermal history of the DM samples never involved heating above melting. On the contrary, the reflow soldering involves rapid dissolution of Cu into the liquid solder (heterogeneous solid-liquid reaction). The liquid phase is present until it is completely consumed by the growing IMCs. In this work the reactions involving the liquid phase were terminated after ~ 4 min (end of reflow). The first stage of the reflow soldering is rapid interstitial diffusion of Cu into the liquid Sn-based solder. The solubility of the Cu in liquid Sn is limited by maximum saturation of Cu in the solder or by interfacial continuous IMCs formation (diffusion barrier). The diffusion of Cu into liquid solder results in the nucleation of IMCs in the bulk of the solder material [05Lau, 96Kim] which leading to: (i) supersaturation of the Cu in Sn-based alloy caused by cooling, and (ii) consumption of the Sn by interfacial IMC formation, resulting in an increase of the degree of supersaturation of Cu in the Sn-based alloy. Gagliano [02Gag] observed that the growth rate of IMC precipitates during reflow is initially very fast as a result of supersaturation. In other words, the local concentrations of Cu dissolved in the molten Sn, decrease as IMC islands are formed. Figure 2.3 shows the Cu_6Sn_5 precipitates formed during the reflow process inside the nonreacted solder. In the case of the SAC405 and Sn-3.5Ag, beside the Cu_6Sn_5 precipitates, the primary Ag_3Sn grains are still present. Given the nature of the reflow process and the thermodynamics of the ternary systems, the coexistence of Cu_6Sn_5 and of Ag_3Sn precipitates is likely. The microstructure of the reflow sample which was made from pure Sn metal shows no evidence of Cu_6Sn_5 precipitates.

However, significant differences in the size of the IMC precipitates are observed for the two solder alloy systems. Sn-3.5Ag displays both large and small grains, and in other words a bimodal size distribution of Cu_6Sn_5 ($\sim 7\text{-}8\mu\text{m}$) and Ag_3Sn ($\sim 4\text{-}5.5\mu\text{m}$) while in the SAC405 solder only small Ag_3Sn precipitates ($1.5\text{-}2.5\mu\text{m}$) are visible. The different dimensions of the Ag_3Sn primary grains can be related to the solder composition that affects both the nucleation and growth processes. The distribution of Cu_6Sn_5 precipitates in the matrix of the Sn-3.5Ag solder alloy is uniform. In the case of the large precipitates, the EDS point analysis matches the stoichiometry of the Cu_6Sn_5 and Ag_3Sn phases, Figure 2.3 and Table 2.1.

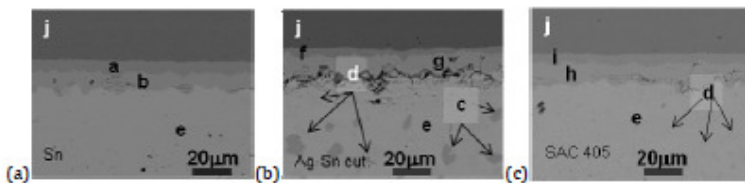


Fig. 2.3: Microstructure (BSE) of reflow samples (a)Sn, (b)Sn-3.5Ag and (c) SAC405 after 336h annealing at 200°C.

According to Gong at el. [09Gon] the main components of the eutectic SAC alloy under equilibrium solidification conditions are Ag_3Sn and Cu_6Sn_5 IMC precipitates in a

β -Sn matrix leading to a uniform eutectic microstructure. These observations are in good agreement with previous studies of the ternary Sn-Ag-Cu system [08Yoo, 04Yoo, 07Cha, 06Jay, 01Kim]. The interfaces identified by the SEM/EDS measurements between Cu and IMC, and between the various IMCs themselves at any stage of the annealing are linear because the interfacial processes take place in the solid state and the Cu_3Sn grows out of the Cu_6Sn_5 phase. The exception is the interface between initially liquid solder and a Cu_6Sn_5 layer (escalloped like morphology) formed during the early stage of annealing [02Gag, 95Bad, 05Goe].

The rate of the Gibbs free energy gain is much faster in the scallop-type growth when compared to the layer type growth, because it is controlled by the rapid diffusion of Cu into the molten solder. The rate of the free energy change, rather than the free energy gradient itself, favours the scallop-type IMC growth and the morphology of these scallops has enabled the overall process to proceed much faster. According to Gong [08Gon] the scallop morphology of Cu_6Sn_5 is controlled by both, the heterogeneous dissolution into the molten solder phase and the growth behaviour under typical reflow temperature profile conditions i.e. heating, holding and cooling down. The scallops have a larger surface area than a flat surface. This morphology is unfavourable because of the high interfacial energy between solid solder and Cu_6Sn_5 . In the wetting reaction, the rapid gain in compound formation energy may compensate the surface energy spent in growing the scallops. During solid state aging, the gain disappears, and the morphology of the interface changes to a layer-type morphology with a flat surface because of the high interfacial energy between solid solder and Cu_6Sn_5 [07Wan]. According to Sonwoo [92Sun] and Zeng [05Zen] this behaviour is driven by the surface tension and can occur relatively rapidly, particularly when assisted by surface diffusion at the interface. Here, we clearly observe a flattening of the scallop - like Cu_6Sn_5 interface during annealing [11Paw,12Paw],[11Paw, 11Paw1].

~~In [11Paw,12Paw] the activation energies are calculated for the Sn-Cu-Ag system and compared with values from other authors. The activation energies are calculated and summarized for Sn-Cu-Ag system in [11Paw, 11Paw1] and was compared with values from other authors [04Yoo, 95Bad, 82Tu, 96Tu, 75Oni, 64Sta, 92Mei, 00Cho, 03Mad, 75Lub, 95Dre, 03Yoo, 06Lia].~~ E_A values for the Cu_3Sn growth in Cu|Sn DM and reflow samples range from 22.4 and 94.54 kJ/mol, respectively and for Cu_6Sn_5 from 9.1 to 69.3 kJ/mol. The remarkable scatter of the activation energy values obtained by previous studies compared to this work may result from the difficulty of measuring an accurate layer thickness. Particularly, for very thin layers the interface between the two IMC layers: are often ill-defined (non-planar), develop scallop morphology, or are not clearly visible. It is known, that the differences in the initial conditions arising from the sample preparation also affect the reaction rate. The methodology used here (DM) for sample preparation and thickness determination may present an advantage over previous work. According to Onishi [75Oni] and Yoon [04Yoo] the differences between reported activation energy data are caused by the different soldering methods, diffusion couple preparation, aging time and temperature and analytical artifacts. Choi [00Cho] suggested temperature dependent activation energy for Cu_6Sn_5 and Cu_3Sn growth (non-Arrhenius behavior). However, the Gibbs free energy of IMC formation in the Cu-Sn system, DG_f , barely changes with temperature [96Shi,07Fla]. The arguments of Choi, that different mechanisms control

the reactions at high and low temperatures are not supported by the results presented here. The data in Table 2.2 and 2.3 for Cu-Sn-Ag kinetic system [11Paw, 11Paw1] indicated that the IMC growth in the Cu|Sn system is always diffusion controlled in the temperature range from 150°C to 200°C.

Table 2.2: Parabolic rate constant of IMC growth in the temperature range 150-200°C.

Type of sample	$k(Cu_3Sn)$, cm ² /s			$k(Cu_6Sn_5)$, cm ² /s		
	150	180	200	150	180	200
Cu Sn (DM)	3.07 10 ⁻¹⁴	4.21 10 ⁻¹⁴	6.14 10 ⁻¹⁴	7.02 10 ⁻¹⁴	1.07 10 ⁻¹³	6.63 10 ⁻¹³
Cu Sn reflow	2.72 10 ⁻¹⁴	1.44 10 ⁻¹⁴	2.58 10 ⁻¹³	6.94 10 ⁻¹³	5.23 10 ⁻¹³	4.30 10 ⁻¹³
Cu SAC405 reflow	2.01 10 ⁻¹⁴	4.91 10 ⁻¹⁴	1.63 10 ⁻¹³	1.08 10 ⁻¹³	4.29 10 ⁻¹³	4.60 10 ⁻¹³
Cu Sn-3.5Ag reflow	1.19 10 ⁻¹⁴	4.86 10 ⁻¹⁴	2.18 10 ⁻¹³	1.12 10 ⁻¹³	1.86 10 ⁻¹³	5.10 10 ⁻¹³

Table 2.3: Activation energy of Cu-Sn IMC's growth in 150-200°C temperature range.

Type of sample	$E_A(Cu_3Sn)$, kJ/mol	$E_A(Cu_6Sn_5)$, kJ/mol	T , °C
Cu Sn (DM)	22.37	69.28	150-200
Cu Sn (reflow)	36.22	9.07	150-200
Cu Sn-3.5Ag (reflow)	94.50	22.15	150-200
Cu Sn-4.0Ag-0.5Cu (reflow)	67.36	50.83	150-200

References

- [01Zha] Zhao, J.-C.. *Advence: Engineering Materials* 2001, **3**, 143.
- [05Zha] Zhao, J.-C., Zheng, X., Cahill, D.G.: *Materials Today*, 2005, October, 28-37.
- [07Zha] Zhao, J.-C. *editor*. "Methods for Phase Diagram Determination". Elsevier Ltd.; 2007.
- [10Tho] Thompson, R.J., Zhao, J.-C., Hemker, K.J.: *Intermetallics*, 2010, **18**, 796-802.
- [07Zha] Zhao, J.-C., Jackson, M.R., Peluso, L.A.: *Mater. Sci. Engn. A* 2004, **372**, 21-27.
- [03Zha] Zhao, J.-C., Jackson, M.R., Peluso, L.A.: *Acta Materialia*, 2003, **51**, 6395-6405.
- [05Cam] Campbell, C.E., Zhao, J.-C., Henry, M.F.: *Mater. Sci. Engn. A*, 2005, **407**, 135-146.
- [05Zha1] Zhao, J.-C.: *Progress Prog. in Material Mater. ScienceSci*, 2006, **51**, 557-631.

- [11Paw] Pawelkiewicz, M.: PhD Dissertation AGH-University of Science and Technology, Krakow, January 2011.
- [12Paw] Pawelkiewicz M, Wierzba B, Danielewski M, Janczak-Rusch J, *Defect and Diffusion Forum Vols. 323-325 (2012) 127-132*
- [11Paw1] Pawelkiewicz, M., Danielewski, M., Janczak-Rusch, J.: *Acta Mater.*, 2011, submitted.
- [11Paw2] Pawelkiewicz, M., Danielewski, M., Janczak-Rusch, J., Wierzba, B.: *DIMAT 2011, 4-8 July 2011, Dijon, France.*
- [11Paw13] Pawelkiewicz, M., Danielewski, M., Janczak-Rusch, J., Wierzba B.: *EUROMAT 2011, 12-15 September, Montpellier, France.*
- [05Lau] Lauria, T., Vuorinen, V., Kivilahti, J.K.: *Mater. Sci. Engn. R*, 2005, **38**, 1-60.
- [96Kim] Kim, H.K., Tu, K.N.: *Physical Phys. Review Rev. B*, 1996, **53**, 16027-16034.
- [02Gag] Gagliano, R.A., Ghosh, G., Fine, M.E.: *J. of Electronics-Electron. Materials Mater.*, 2002, **31**, 1195-1202.
- [09Gon] Gong, J., Liu, C., Conway, P.P., Silberschmidt, V.V.: *Scripta Mater.*, 2009, **61**, 682-685.
- [08Yoo] Yoon, J.-W., Jung, S.-B.: *Journal of Alloys and Compounds Compd.*, 2008, **458**, 200-207.
- [04Yoo] Yoon, J.-W., Lee, Y.-H., Kim, D.-G., Kang, H.-B., Suh, S.-J., Yang, C.-W., Lee, C.-B., Jung, J.-M., Yoo, C.-S., Jung, S.-B.: *Journal of Alloy and compounds compd.*, 2004, **381**, 151-157.
- [07Cha] Chao, B., Chae, S.-H., Zhang, X., Lu, K.-H., Im, J., Ho, P.S.: *Acta Materialia Mater.*, 2007, **55**, 2805-2814.
- [06Jay] Jayaganthan, R., Mohankumar, K., Sekhar, V.N., Tay, A.A.O., Kripesh, V.: *Materials Mater. Letters Lett.*, 2006, **60**, 1089-1094.
- [01Kim] Kim, K.S., Huh, S.H., Sukanuman, K.: *J. Alloys and Compound Compd.* 2003, **352**, 226-236.
- [95Bad] Bader, S., Gust, W., Hieber, H.: *Acta Metallurgica-Metall. et Materialia Mater.*, 1995, **43**, 329-337.
- [05Goe] Goerlich, J., Schmitz, G., Tu, K.N.: *Applied Appl. Physics Phys. Letters Lett.*, 2005, **86**, 053106.
- [08Gon] Gong, J., Liu, C., Conway, P.P., Silberschmidt, V.V.: *Acta Mater.*, 2008, **56**, 4291-4297.
- [07Wan] Wang, F.-J., Yu, Z.-S., Qi, K.: *Journal of Alloys and Compounds Compd.*, 2007, **438**, 110-115.
- [92Sun] Sunwoo, A.J., Morris, Jr. J.W., Lucey, Jr. G.K.: *Met. Trans. A*, 1992, **23**, 1323-1332.
- [05Zen] Zeng, K., Stierman, R., Chiu, T.-C., Edwards, D., Ano, K., Tu, K.N.: *Journal of Applied Appl. Physics Phys.*, 2005, **97**, 024508.
- [82Tu] Tu, K.N., Thompson, D.: *Acta Metallurgica*, 1982, **30**, 947-952.
- [96Tu] Tu, K.N.: *Materials Chemistry and Physics*, 1996, **46**, 217-223.
- [75Oni] Onishi, M., Fujibuchi, H.: *Trans.: JIM*, 1975, **16**, 539-547.
- [64Sta] Starke, E., Wever, H.: *Zeitschrift Fur Metallkunde*, 1964, **55**, 107-116.
- [92Mei] Mei, Z., Sunwoo, A., Morris, Jr. J.W.: *Metallurgical Transactions A*, 1992, **23**, 857-864.
- [00Cho] Choi, S., Lucas, J.P., Subramanian, K.N., Bieler, T.R.: *Journal of Science: Materials in Electronics*, 2000, **11**, 497-502.
- [03Mad] Madeni, J., Liu, S., Siewert, T.: *2nd International Brazing and Soldering Conference (ISBC) San Diego, California: February 17-19, 2003.*
- [75Lub] Lubyova, Z., Fellner, P., Matiasovsky, K.: *Z. Metallkunde*, 1975, **66**, 179-182.
- [95Dre] Dreyer, K.F., Neils, W.K., Chronik, R.R., Grosman, D., Cotts, E.J.: *Applied Physics Letters*, 1995, **67**, 2795-2797.

Formatted: Dutch (Belgium)

Formatted: Dutch (Belgium)

Formatted: Dutch (Belgium)

[03Yoo] Yoon, J.W., Lee, C.B., Kim, D.U., Jung, S.B.: Metals and Materials International, 2003, **9**, 193.

[06Lia] Liao, C.N., Wei, C.T.: Thin Solid Films, 2006, **515**, 2781-2785.

[96Shi] Shim, J.-H., Oh, C.-S., Lee, B.-J., Lee, D.N.: Z. MetallkundeMetallkd., 1996, **87**, 205-212.

[07Fla] Flandorfer, H., Saeed, U., Luef, C., Sabbar, A., Ipser, H.: Thermochemica Thermochim. Acta, 2007, **459**, 34-39.

[92Sun] Sunwoo AJ, Morris Jr IW, Lucey Jr GK. Metallurgical Transactions A 1992,**23**,1323-1332

[05Zen] Zeng K, Stierman R, Chiu T-Ch, Edwards D, Ano K, Tu KN. Journal of Applied Physics. 2005,**97**,024508

3 Volumetric description of lead-free solder microstructure

M. Pawelkiewicz, G. Toporek, J. Janczak-Rusch, P. Zolliker, M. Scheller, K.K. Sosnowska

Empa, Swiss Federal Laboratories for Materials Science and Technology, The Switzerland

With the extensive research in the field of lead-free solder alloys in recent years, several promising candidates have been identified for different soldering applications. The major solder alloys are based on the Sn-Ag-Cu ternary system. The overall microstructure of the solder joint has a notable impact on its mechanical properties, nevertheless not each of the microstructural components have the same impact. Especially intermetallic compounds as Ag_3Sn and Cu_6Sn_5 forming at the solder-based material interface or reinforcing particles used for the production of composite lead-free solders have a significant effect on the mechanical properties of the solder joints. The phases that play the most important role from mechanical point of view are: interfacial intermetallic compounds (IMC), IMC participation in the microstructure - Ag_3Sn and Cu_6Sn_5 and in the case of the composite solder alloys – reinforcing particle, ie. μm or nm -Cu particles [09Siv]. The information about the volume of each of the phases present in the microstructure is important to determinate the mechanical properties of the solder joint. The target of this study was to formulate an image recognition method for the phases present in the lead-free solder joint microstructure and implement an algorithm for phase segmentation. The volumetric description obtained with the proposed algorithm provides an input for further finite-element based modelling of mechanical response of the joints.

Materials

The investigation was performed on the microstructures of reflow solder joints: SAC405 (Sn-4.0Ag-0.5Cu) and composite SAC405 with 1.6 vol% nmCu particles. The cross section of each sample was prepared in a traditional metallographic way. Scanning Electron Microscopy (SEM), Computed Tomography (CT) and Optical Microscopy (OM) data were obtained and analysed. The segmentation algorithm has been verified with optical images, having in mind that the optical microscopy is the simplest and industrially most common technique of the microstructure characterisation.

In the bulk microstructure of the Sn-Ag-Cu solder alloy, the mixture of few phases is expected: dendritic β -Sn, pallet-like Ag_3Sn , precipitates of Cu_6Sn_5 and eutectic mixture of Sn-Ag-Cu. The micrographs of the microstructure of the SAC405 solder joints exhibit a group of β -Sn dendritic structures surrounded by a network of small, periodic, dot-like structures – eutectic mixture consisting of β -Sn, Ag_3Sn , and Cu_6Sn_5 . Apart from that, one can observe large IMC structures: Ag_3Sn (Ag-rich phase), Cu_6Sn_5 (Cu-rich phase) and interfacial IMCs - Cu_6Sn_5 and Cu_3Sn at the boundary between Cu substrate and solder (Figure 3.1) [09Siv,98Yos]. Additionally, in case of composite solders the Cu particles partly or fully transferred in Cu_6Sn_5 are presented.

Comment [AK2]: Because of the overall extent of the charter – I would recommend to drop this section – it does not bring anything new, it is just description of method; I prefer to keep it, since it is important to obtain input for simulations;

Formatted: Dutch (Belgium)

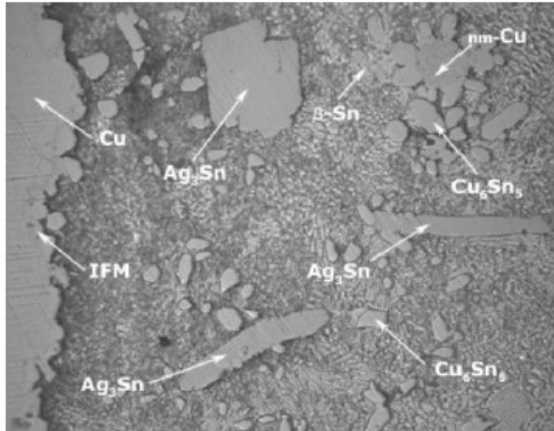


Fig. 3.1.: SAC405 with nm-Cu particles solder joint microstructure

Phase segmentation algorithm

Image segmentation is a process of separation of image regions in order to get unique, non-overlapping visual segments of the picture. The phase segmentation algorithm identifies areas of pixels (with similar brightness) in the image and does not require any information or labelling of existing phase domains in the system. The approach requires distinguishing pixels without any prior user knowledge and interaction, labelling them and using for specific purposes in a computed manner. There is no single segmentation method valid for any type of image; therefore the successful algorithm has to be purpose specific.

All analyzed images were captured with Leica DC500 digital camera on Leica DM RX optical microscope and transferred by software Leica Firecam Version 1.1.1 on Mac. The captured images were examined closely and general idea about the present phase in the microstructure was doneacquired. Additionally, the photometric measurement of different phases in the microstructure was performed by Leica MPV spectrometer; a reflectivity of phases was estimated. Due to mirror-like, well-polished surface of solder alloy, a specular reflection from phases was observed compared to diffuse reflection from white standard. In specular reflection a light from incoming direction is reflected into a single outgoing direction. This is accordingly to law of reflection where both rays have the same angle with respect to surface normal. In diffuse reflection light would reflect into wide range of directions creating hemisphere around this surface. High volume of light returning to spectrometer sensor influences high reflectivity of solder alloy phases, therefore low volume of light, which was spread around surface, influences low reflectivity of white standard. Each phase presented in the microstructure, except for Cu, showed peaks at wavelength 575 nm. This leads to clarification about the same hue and saturation of the phase image. Thus, only Cu (with a peak at wavelength 598 nm) can be distinguished by its colour. The differences in brightness between the phases are too

Comment [AK3]: „in computerized manner“
maybe this expression is more suitable

small to be used as the only criterion; however they are enough for the algorithm to work on the grey-scale image once Cu is excluded. Since the solder background microstructure (β -Sn and eutectic mixture) shows high level of non-uniformity and complexity the possible approach to separate IMCs from background is to compute local variation in brightness. The smooth and homogenous IMC regions with low local variation and the background appearing rough with high local variation allow for this approach. However, the algorithm has to distinguish β -Sn from IMCs. Using this regularity, RGB image is normalized and the difference in colour planes is computed. The main advantage of this part is high precision. Finally, those approaches were established as most appropriate ones and segmentation algorithm was implemented into Matlab. The algorithm used in the developed software is shown schematically in Figure 3.2.

Results of Image Analysis of lead-free solders

A code for segmentation was implemented into Matlab. To evaluate algorithm a ground truth data was collected. The training set of twelve microscopic images was chosen and presented to the human experts for comparison between original images with the proposed segregation. A typical result of the segmentation is shown in Figure 3.3.

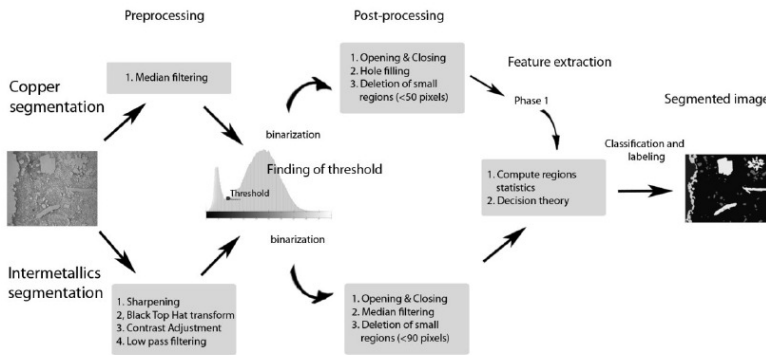
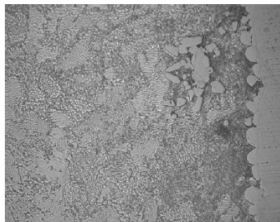


Fig. 3.2: Segmentation algorithm diagram

Comment [AK4]: Copyright?



(a)

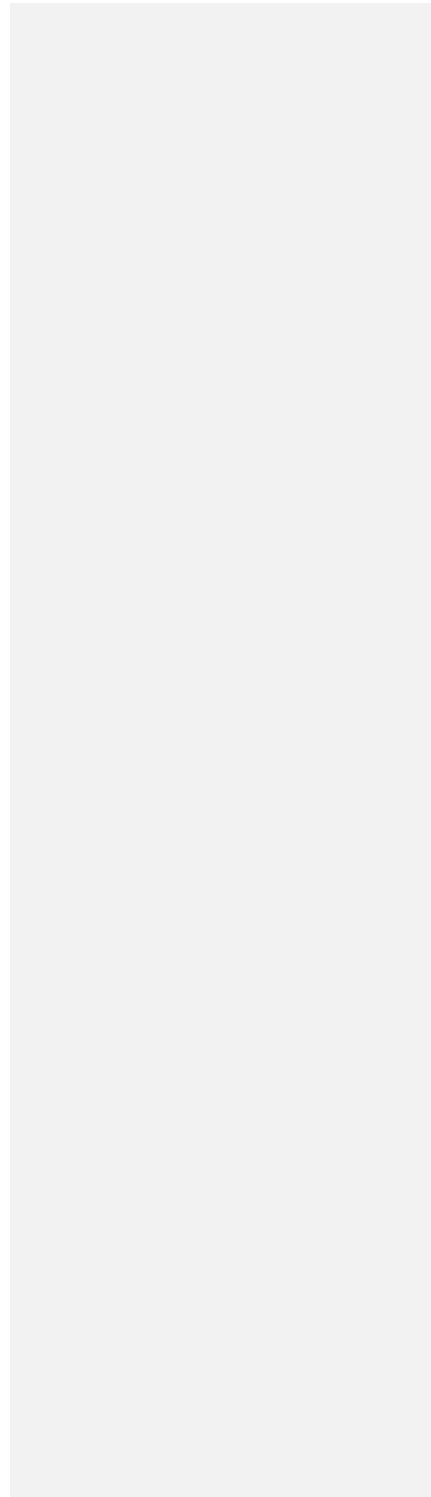


(b)

Fig. 3.3: An example of image segregation (a) original image and (b) proposed segregation.

References:

- [09Svi] Sivasubramaniam, V., Galli, M., Cugnoni, J., Janczak-Rush, J., Botsis, J.: *Journal of Electronic Materials*, 2009, **38**, 2122-2131.
- [98Nak] Nakamura, Y., Sakakibara, Y., Watanabe, Y., Amamoto, Y.: *Soldering and Surface Mount Technology*, 1998, **10**, 10-12.



4 Contribution to thermodynamic description of Ag-Ce-Sn system

R. Čička¹, A. Kroupa², A. Zemanová², M. Drienovský¹, J. Janovec¹

¹Slovak University of Technology, Faculty of Materials Science and Technology.,
Trnava, Slovakia

²Institute of Physics of Materials AS CR, Zizkova 22, Brno., Czech Republic

Outline

Recently much effort was done in the investigation of systems based on Sn-Ag-Cu (SAC) with the intention to improve their solderability and properties. These systems seem to be suitable for replacement of lead-containing solders traditionally used in electronic industry [07Mhi, 06Tia]. In the last years, effects of rare earth addition (e.g. Ce, La) on microstructure, solderability and mechanical properties of SAC systems were experimentally investigated [04Wu, 07Zha, 09Wan]. The results indicate that small additions of Ce and La result in the refinement of microstructure as well as in improving the tensile strength, the creep behaviour, and the wettability. However, some important aspects are still not clear. The principle task is to include rare earth elements in thermodynamic databases of lead-free solder systems.

The samples of Ce-Sn with compositions 5 at.%Ce (sample 1), 10 at.%Ce (sample 2), 15 at.%Ce (sample 3), and 20 at.%Ce (sample 4) were prepared in vacuum furnace Degussa using induction heating in Ar atmosphere. Experimental techniques of light microscopy (Neophot 32 with CCD camera), scanning electron microscopy and energy-dispersive spectroscopy (JEOL JSM 7600 F), X-ray diffraction (Phillips PW 1710 with Co anode) and differential thermal analysis (NETZSCH STA 409 CD) in Ar atmosphere were used for characterization of samples.

In the computational part, the parameters of the Ce-Sn system were optimized using PARROT module of Thermocalc software.

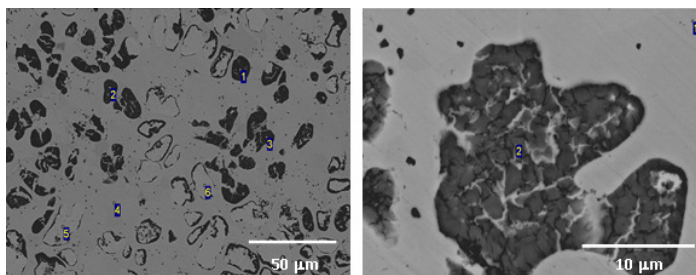


Fig. 4.1: Micrograph of sample 2 using scanning electron microscopy (left), detail of dark particle (right); numbers denote the points of EDS analysis

Thermodynamic description of Ag-Ce, Ag-Cu and Ce-Sn binary systems and Ag-Ce-Sn ternary system

4.1.1 Ag-Sn system

Thermodynamic database of Ag-Sn system was accepted from SOLDERS database of lead-free solder systems [08Din].

4.1.2 Ag-Ce system

Thermodynamic assessment of Ag-Ce system was done by Yin et al [02Yin]. They optimized the thermodynamic parameters of all solution phases (bcc, fcc, liquid) and stoichiometric intermetallic compounds (Ag_4Ce , $\text{Ag}_{51}\text{Ce}_{14}$, Ag_2Ce , AgCe), using experimental data related to phase equilibria in phase diagram and thermochemical data related to mixing enthalpy and enthalpies of forming of intermetallic compounds.

4.1.3 Ce-Sn system

The following experimental data on phase diagram Ce-Sn are available:

- phase diagram [98Ria]
- enthalpy of mixing in melt at 1870K, in composition range Sn–30%Ce [96Heu]
- forming enthalpies of intermetallic phases at room temperature [82Bor]

Based on these data, we proposed the thermodynamic database of Ce-Sn system and optimized the thermodynamic parameters using PARROT module of Thermo-Calc. The comparison with experimental data is shown in Figure 4.2. Because of the differences between the experimental and calculated liquidus curve near to Sn corner, this part of the phase diagram was verified experimentally, and we confirmed the correction of liquidus curve according to calculated curve.

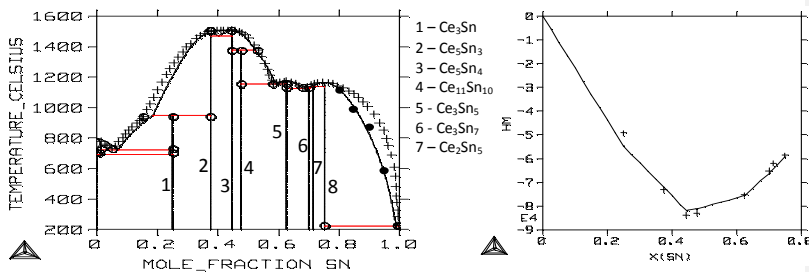


Fig. 4.2: Calculated phase diagram of Ce-Sn system (left) and forming enthalpies of intermetallic phases at room temperature (right), compared to experimental data taken from phase diagram of Riani [98Ria] (liquidus line +, invariant reactions o) and Borzone [82Bor] (forming enthalpies +); calculated liquidus line at Sn-rich corner is in agreement with measured liquidus temperatures of our samples (●)

Comment [AKS]: The compound 8 is not described in the legend and the format of the figure could be better – I will contact Cicka to discuss better figure with him

4.1.4 Ag-Ce-Sn system

The isothermal section of the Ag-Ce-Sn system at 750 °C was published by Boulet et al [99Bou]. They found three ternary phases in this system, τ_1 ($Ce_3Ag_4Sn_4$), τ_2 ($CeAgSn$) and τ_3 (Ce_5AgSn_3). For the thermodynamic assessments of the Ag-Ce-Sn system we created the thermodynamic database of Ag-Ce-Sn system by using binary assessments of Ag-Sn, Ag-Ce, Ce-Sn system, and the assessment was finalized using the experimental solubilities and phase equilibria given by Boulet at 750 °C. The comparison between calculated isothermal section of Ag-Ce-Sn system at 750 °C and that from Boulet is shown in Figure 4.3. Clearly, it can be seen, that it was not possible to set all ternary parameters to achieve agreement with the experimental phase diagram. The reason is that there is an insufficient amount of experimental data, mainly enthalpy of mixing, forming enthalpies of ternary phases τ_1 , τ_2 , τ_3 , and experimental phase equilibria at some other temperatures.

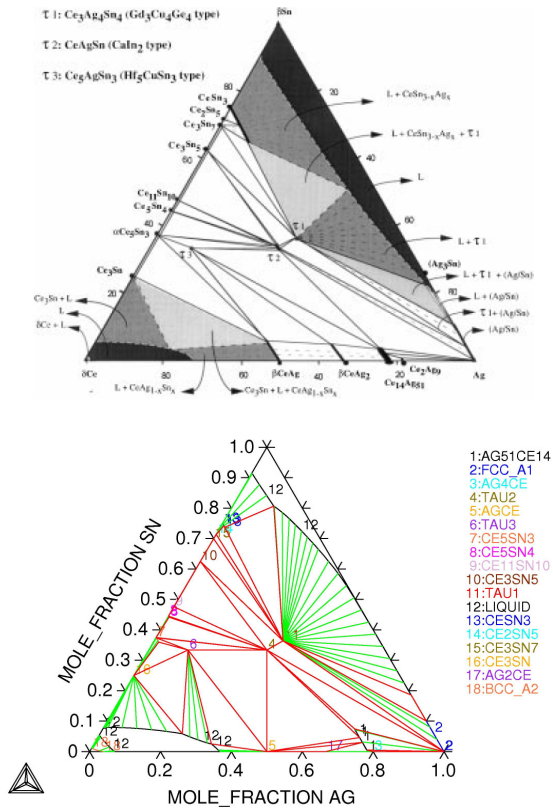


Fig. 4.3: Comparison between experimental isothermal section of Ag-Ce-Sn system at 750 °C [99Bou] (upper) and calculated diagram (lower)

Comment [AK6]: Again, the figures has to be redone, I will discuss it with Cicka, also copyright here

References

- [07Mhi] Mhiaoui, S., Sar, F., Gasser, J.G.: *J. Non-Cryst Solids*, 2007, **353**, 3628.
- [06Tia] Tian, Y.H., Wang, C.Q., Zhou, W.F.: *Acts Metall. Sin. (Engl. Lett.)*, 2006, **19**, 301.
- [04Wu] Wu, C.M.L., Yu, D.Q., Law, C.M.T., Wang, L.: *Mat. Sci. Eng. R*, 2004, **44**, 1.
- [07Zha] Zhao, X.Y., Zhao, M.Q., Cui, X.Q., Xu, T.H., Tong, M.X.: *Transf. Nonferrous Met. Soc. China*, 2007, **17**, 805.
- [09Wan] Wang, J.X, Xue, S.B, Han, Z.J., Yu, S.L, Chen, Y., Shi, Y.P., Wan, H.: *JAC*, 2009, **467**, 219.
- [06Chu] Chuang, T.H.: *Scripta Materialia*, 2006, **55**, 983.
- [08Din] Dinsdale, A., Watson, A., Kroupa, A., Vrestal, J., Zemanova, A., Vizdal, J.: *Atlas of Phase Diagrams for Lead-Free Soldering, COST 531*, 2008.
- [02Yin] Yin, F., Huang, M., Su, X., Zhang, P., Li, Z., Shi, Y.: *J. Alloys Comp.*, 2002, **334**, 154.
- [98Ria] Riani, P., Mazzone, D., Zanicchi, G., Marazza, R., Ferro, R.: *J. Phase Equilibria*, 1998, **19**, 239.
- [96Heu] Heuzey, M.C, Pelton, A.D.: *Metallurgical and Mat. Trans. B*, 1996, **27B**, 810.
- [82Bor] Borzone, G., Borsese, A., Ferro, R.: *J. Less Common Metals*, 1982, **85**, 195.
- [99Bou] Boulet, P., Mazzone, D., Noël, H., Riani, P., Rogl, P., Ferro, R.: *Intermetallics*, 1999, **7**, 931.

5 Reactions in liquid- and solid-states of Sn/Ag/Cu/Ce solders with Cu-substrate

Milan Ožvold, Katarína Pocisková Dimová, Lýdia Rízeková Trnková, and Jozef Janovec

Slovak University of Technology, Faculty of Materials Science and Technology, Trnava, Slovakia

Impact of Ce on microstructure of solders

When a small amount of rare earth element (e.g. Ce) is added into lead-free Sn-Ag-Cu solders, the solder microstructure becomes finer as a rule. It is documented in Fig. 5.1 for eutectic SnAg3.5Cu0.7, SnCu0.7, and SnAg3.5 solders. The solder microstructures were found to be finer with increasing the bulk Ce content, except for the SnCu0.7 eutectic solder showing the finest microstructure without the Ce addition.

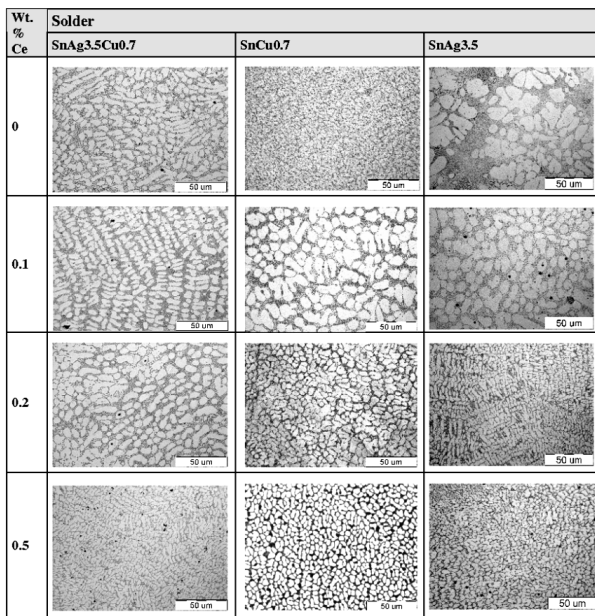


Fig. 5.1: Microstructures of solders with different contents of Ce

As shown in Fig. 5.2, the ultimate tensile strength of the solders may be influenced significantly by adding tiny amounts of Ce. The highest strengthening effect is obtained for solders with Ag and a concentration of Ce of about 0.125 wt.%.

Comment [AK7]: The figure needs more kontrast. Generally, there are too many small figures in all figures in the text. I strongly recommend to show only few of the sets in bigger sizes as an examples.

In this study, the influence of the solder original microstructure on both solderability and aging of the Cu-substrate was investigated. The solder reacts with the Cu-substrate during soldering (i.e. dipping the Cu-substrate into the molten solder) and forms an IMC (intermetallic compound) layer at the joint interface. The IMC layer is a requisite of required to achieve a good metallurgical joint. However, an excessive growth of the IMC layer may have a negative impact on the soldered joint.

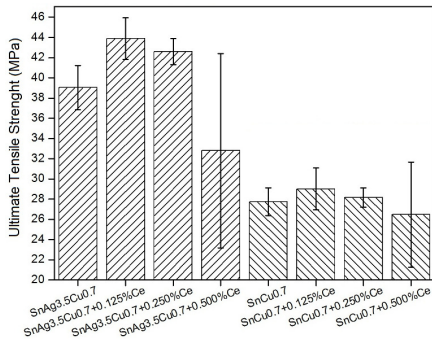


Fig. 5.2: Ultimate Tensile Strength of solders with different contents of Ce

Solder preparation

The solders used for the experiments were prepared in two steps from pure Sn, Ag, Cu, and Ce components. The purity of basic metals was 99.99 wt.%, and the Ce purity was 99.9 wt.%. In the first step, SnAgCu, SnCu and SnAg alloys were prepared having the eutectic compositions. Then, Sn-Ce alloys with the bulk Ce contents from 2 to 5 wt. % were prepared by melting at 500°C for 5 hours under vacuum. The alloys with a final concentrations of 0.1, 0.2 and 0.5 wt.% Ce [11] compositions (Table 5.1) were then prepared by re-melting of the above master alloys. The dissolution of cerium in the precursor was verified using the energy dispersive X-ray spectroscopy (EDX). The melting behaviour of solders, as one of the most important characteristics, was determined by means of differential scanning calorimetry (DSC). The solder microstructures and interfaces were observed by the light microscopy and scanning electron microscopy (SEM). The EDX was used to determine Sn, Ag, Cu contents of in the analysed areas.

Table 5.1: Chemical compositions of investigated solders (wt.%)

SnAg3.5	SnCu0.7	SnAg3.5Cu0.7
Sn 96.48 Ag 3.42 Ce 0.1	Sn 99.22 Cu 0.68 Ce 0.1	Sn 95.83 Ag 3.39 Cu 0.68 Ce 0.1
Sn 96.47 Ag 3.34 Ce 0.2	Sn 99.13 Cu 0.67 Ce 0.2	Sn 95.86 Ag 3.28 Cu 0.66 Ce 0.2
Sn 96.41 Ag 3.09 Ce 0.5	Sn 98.91 Cu 0.59 Ce 0.5	Sn 95.95 Ag 2.96 Cu 0.59 Ce 0.5

Formatted: Font: 11 pt, Bold

Formatted: Normal, Centered, Indent: First line: 0 cm, Space Before: 0 pt, After: 0 pt, Don't adjust space between Latin and Asian text

Formatted: Font: 11 pt

DSC measurements were conducted in the inert gas atmosphere. The calorimeter (Perkin Elmer) was calibrated prior to testing using the standard high-purity tin sample. Solder samples of 20 to 40 mg in weight were placed into the aluminium pan. An empty aluminium pan was used as a reference. The heating/cooling rate was either 10°C/min or 2°C/min. The melting points of alloys have been extracted from DSC heating curves of the second run of totally three runs applied. The melting points of alloys containing 0.5 wt. % Ce were almost the same as those for the samples free of Ce, 227°C and 227.2°C for SnCu0.7 and SnCu0.7+0.5Ce alloys, respectively, 221.3°C for the SnAg3.5 alloy, and 217°C for SnAg3.5Cu0.7 alloys.

Reaction of solders in liquid state

The formation of IMC layers on Cu-substrate was analysed using solders without and with 0.5 wt. % of cerium. The ground and polished Cu plates with the dimensions of 20×10×1 mm were ultrasonically cleaned, etched in the 10% aqueous solution of HCl to remove the oxide film, and rinsed with ethanol. Prior to soldering, the Cu plates were preheated on the hot plate, and a small amount of flux (solution of resin in ethanol) was applied. The effect of a flux residuum was probably eliminated on the preheating. After the flux application, the specimens were dipped into the liquid solder sustained at the temperature of 40°C above the solder melting point. The dipping times were 2, 4, 16 and 256 seconds. The samples for the microstructural analysis were prepared by usual metallographic procedure consisting of polishing and etching (5% HNO₃ + 2% HCl + methanol, etching time 2-5 seconds).

Microstructures of the interfaces are shown in Figure 5.23. The Cu₆Sn₅ IMC layer positioned at the interface between the solder and the Cu-substrate reveals a typical scallop-type shape. The thickness of IMC layer increased with increasing the time of soldering. The scallops joined together and grew with increasing time. Small parts of IMC were observed to be separated from the Cu₆Sn₅ layer.

Comment [AK8]: Why was the flux applied, when it was presumably eliminated before the experiment? For better wetting ?

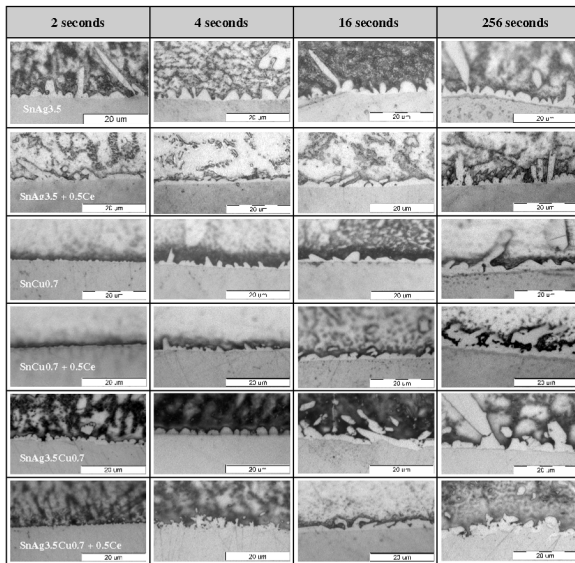
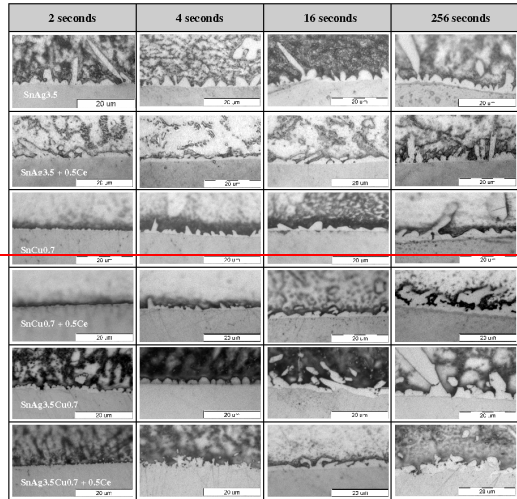


Fig. 5.23: Microstructures at interfaces between investigated solders and the Cu-substrate for various soldering times

Comment [AK9]: Again, is it possible to add contrast to the figure? This is a new figure, but it seems it was not possible to generate a figure with more contrast.

A continuous IMC layer was observed at interfaces of the Sn-Ag based alloys already after 2 s of soldering. The layers showed a thickness of about 3 μm and scallops of the Cu_6Sn_5 phase with size up to the 15 μm . The IMC layer in solders containing Cu was found to be thinner after 2 s of soldering. The uniform Cu_3Sn layer was also observed in SnCu0.7, SnCu0.7+0.5Ce, and SnAg3.5 solders after 256 s.

The soldered joints containing SnAg3.5Cu0.7 and SnAg3.5Cu0.7+0.5Ce alloys revealed differences in morphology of the IMC layer created after 256 seconds of soldering. The layer is not continuous and shows a cracked relief. This effect was already observed for the soldering time of 4 seconds. The long needles of the Cu_6Sn_5 intermetallics were not observed. Similar effects can be seen at interfaces between the SnCu0.7+0.5Ce solder and the Cu-substrate.

After 2 seconds of soldering the thickness of the Cu_6Sn_5 IMC layer at the Cu/SnAg3.5Cu0.7 interface becomes lower if Ce is added, Fig. 5.23. Many authors [04Wu, 07Zha, 10Zha, 05Shi, 06Law, 07Zho, 04Yu] described this inhibitory effect of Ce on growth of the IMC layer. No quantification of it has been published till now. We believe that this effect is neither striking nor unambiguous. Owing to the short time, the result can be seriously influenced by the processing procedure. After 4 s dipping this inhibitory effect was not observed. During the soldering, small amount of a rare earth element may barely influence the growth of the thin IMC layer at the solid-liquid interface. Dudek et al. [06Dud] interpreted the reason for lowering the thickness of the Cu_6Sn_5 layer in the SnAgCu alloy containing La in the way that LaSn_3 contributes to the heterogeneous nucleation of Sn, so that the Sn dendrites solidify more quickly. Thus, the solder remains in a liquid state for a shorter time which equates to less time for the reaction with the Cu-substrate, and lowers in this way the thickness of the intermetallic layer. From the solders used in the present investigation, the deepest changes in the undercooling temperature after adding Ce (up to 20°C determined by DSC) were observed for the SnCu alloy. The change did not show any evident effect of the IMC thickness. The solder solidification probably starts at the solder / IMC layer interface and it is not controlled by the solder bulk solidification. The refinement of the solder microstructure was found to influence the growth of thicker layers and the formation of long scallops, when their dimensions are comparable with the grain sizes of the refined solder. It is well observable for Ce containing solders after 256 seconds of soldering (Fig. 5.23); the layers are discontinuous and long scallops are cracked.

Reaction of solders in solid state

Samples for the annealing experiment in solid state were prepared in the same way as described above, except ~~for that the soldering temperature was now 30°C above the solder melting temperature. It was lower by 10°C to obtain the start with an IMC layer thickness as thin as possible at the starting point.~~ Soldered samples were then annealed at temperatures 80, 120 and 150°C for 50, 200, 500 and 1000 hours and then investigated by light microscopy. As reported earlier, the soldered joints were ruined after 24 h exposure at 170°C due to the formation of a thick IMC layer [08Ozv].

Comment [AK10]: With respect to which temperature?

In Figure 5.34, the interface microstructures are shown between the eutectic SnCu0.7 [11Poc] and SnAg3.5Cu0.7 Ce-free solders and the Cu-substrate after annealing at 150°C. The Cu_6Sn_5 IMC layers can be seen after longer annealing times.

The time-dependent growth of the IMC layer at the Cu-substrate/Ce-containing solder interfaces is illustrated in Figures 5.4-5 and 5.56. The results showed that already a small amount of Ce in the SnCu0.7 solder contributes to both the microstructure refinement and the thinner IMC layer. Uneven and rapidly growing IMC protuberances were observed for Ce-free SnAgCu solder (Fig. 5.34).

To characterise the influence of annealing time on thickness of the IMC layer, experimental measurements were performed on 3-4 places at the solder/Cu-substrate interfaces using the Image-Pro program. The results illustrated in Figure 5.6-7 for 150°C demonstrate the character of the diffusion growth. **It was observed that a thinner IMC layer is formed in the Ce-containing SnAgCu solders for a Ce content below 0.5 wt.%. The effect of the IMC layer thinning was observed when the bulk Ce content did not exceed 0.5 wt.%.** The same effect was also observed in Ce-containing SnCu solders. However, **diffusion** along the grain boundaries affected by the solder microstructure (and also by annealing conditions) can influence the IMC layer growth. It was shown that Ce acts also as an inhibitor for the Cu_3Sn and Cu_6Sn_5 layer growth on prolonged annealing at 150°C (Fig. 5.67).

Comment [AK11]: Ambiguous sentence. Does the Ce content cause really the thinning of the layer after longer time or do you mean that the IMC layer grows more slowly and therefore is thinner?

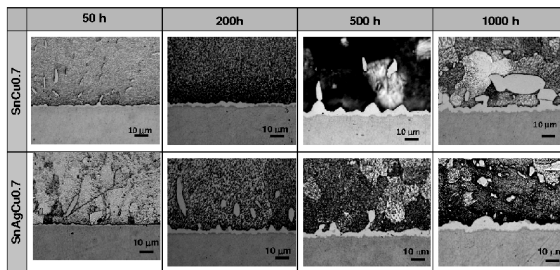


Fig. 5.34: Microstructures of Ce-free solder / Cu-substrate interfaces at 150°C for various annealing times

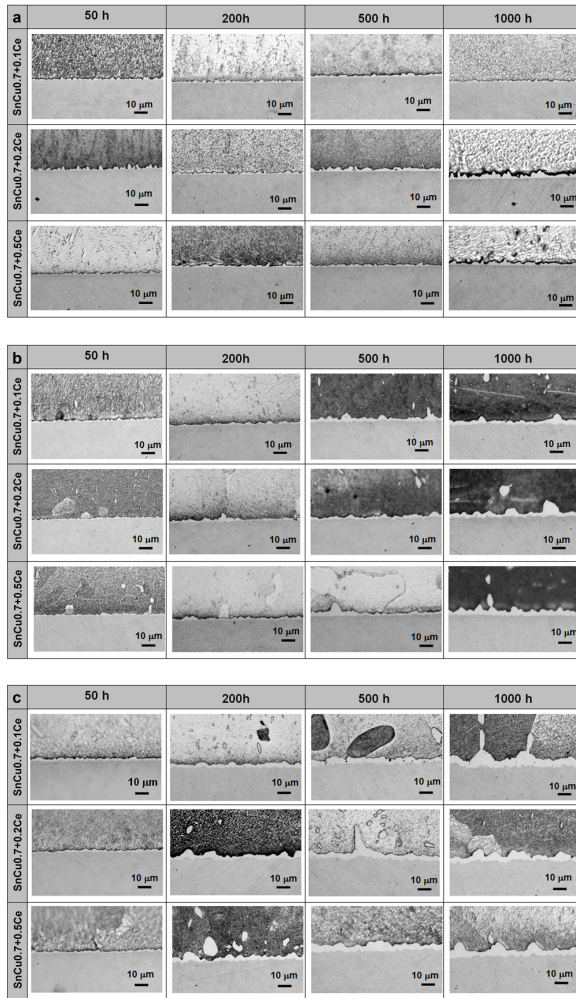


Fig. 5.5: Microstructures of solder / Cu-substrate interfaces for SnCu-base solders after annealing for various times at a) 80°C b) 120°C c) 150°C

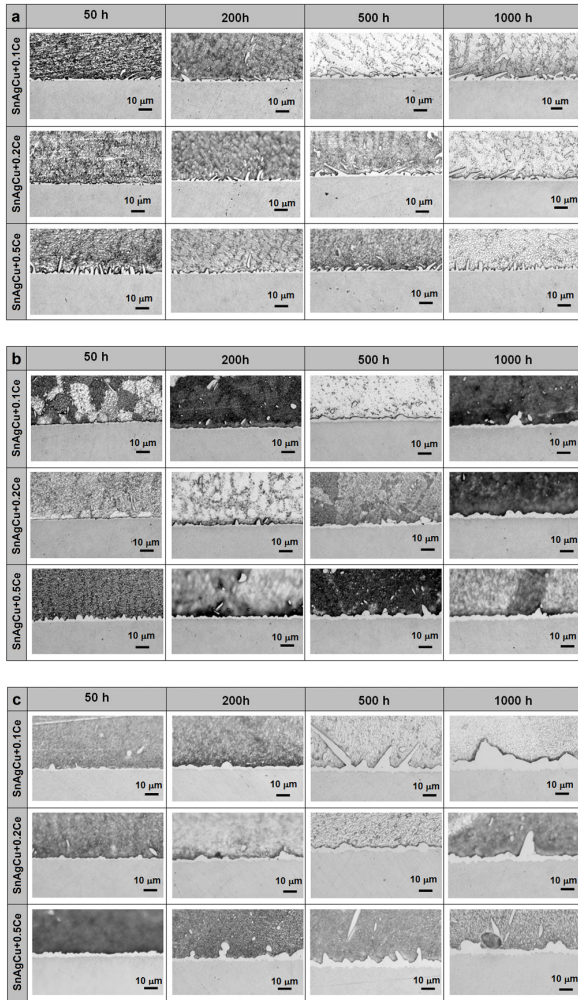
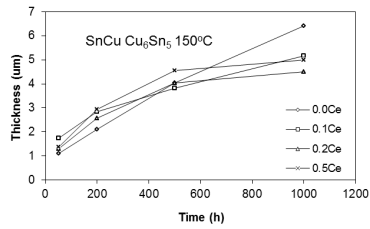
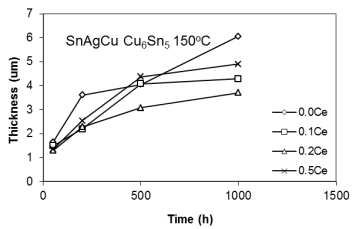
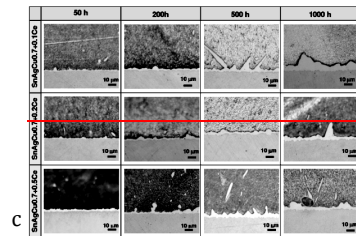
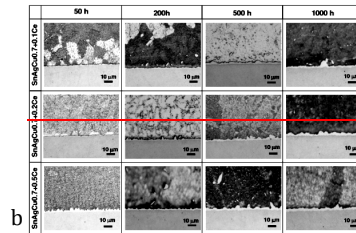
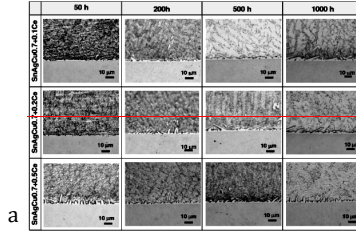
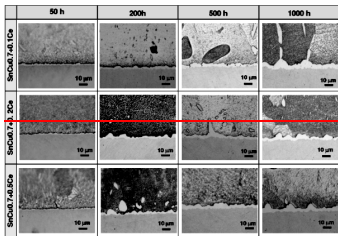
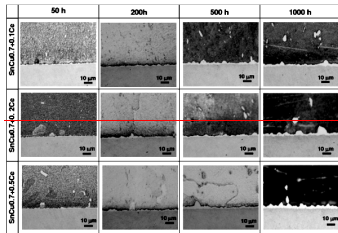
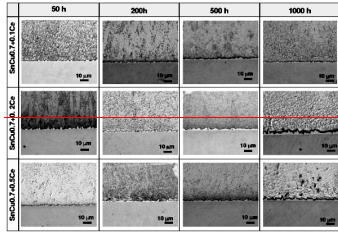


Fig. 5.6: Microstructures of solder / Cu-substrate interfaces for SnAgCu-base solders after annealing for various times at a) 80°C b) 120°C c) 150°C

Comment [AK12]: This is extreme. The figures will be very difficult to read in B5 format. Select only few of them as examples.



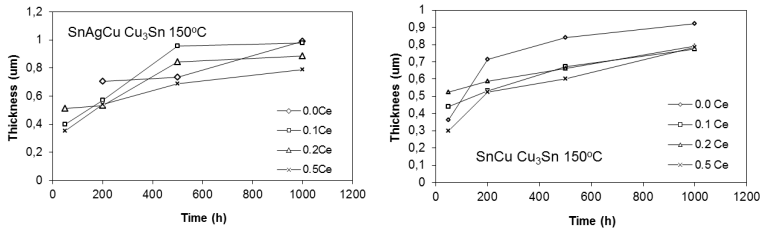


Fig. 5.67: Average thicknesses of Cu₃Sn and Cu₆Sn₅ layers formed at 150°C in dependence on both bulk Ce content and annealing time

References

- [04Wu] Wu, C. M. L., Yu, D. Q., Law, C. M. T., Wang, L.: Mater. Sci. Eng. R, 2004, **44**, 1-44.
- [07Zha] Zhao, X., Zhao, M., Cui, X., Xu, T., Tong, M.: Trans. Nonferrous Met. Soc. China, 2007, **17**, 805-810.
- [02Wan] Wang, L., Yu, D. Q., Zhao, J., Huang, M. L.: Materials Letters, 2002, **56**, 1039-1042.
- [10Zha] Zhang, L., Xue, S., Gao, L., Sheng, Z., Zeng, G., Chen, Y., Yu, S.: J. Mater. Sci.: Mater. Electron, 2010, **21**, 635-642.
- [05Shi] Li, B., Shi, Y., Lei, Y., Guo, F., Xia, Z., Zong, B.: J. of Electronic Mater., 2005, **34**, 217-224.
- [06Law] Law, C. M. T., Wu, C. M. L., Yu, D. Q., Wang, L., Lai, J. K. L.: J. of Electronic Mater., 2006, **35**, 89-93.
- [09Zha] Zhang, L., Xue, S. B., Gao, L. L., Zeng, G., Sheng, Z., Chen, Y., Yu, S. L.: J. Mater. Sci: Mater. Electron, 2009, **20**, 685-694.
- [06Dud] Dudek, M. A., Sidhu, R. S., Chawla, N., Renavikar, M.: J. Electron. Mater., 2006, **35**, 2088-2097.
- [07Zho] Zhou, Y. Ch., Pan, Q. L., He, Y. B., Liang, W. J., Li, W. B., Li, Y. Ch., Lu, C. G.: Trans. Nonferrous Met. Soc. China, 2007, **17**, 1043-1048.
- [04Yu] Yu, D. Q., Zhao, J., Wang, L.: J. Alloys. Compd., 2004, **376**, 170-175.
- [08Ozv] Ožvold, M., Hodúlová, E., Chrišťelová, J., Janovec, J., Turňa, M.: Lead-free solders: comparative study of thermal and wetting properties, In: METAL 2008: 17th International Conference on Metallurgy and Materials, May 13th-15th 2008 Roznov pod Radhostem, Czech Republic.
- [11Poc] Pocisková Dimová, K., Rízeková Trnková, L., Ožvold, M., Turňa, M.: In: METAL 2011, 20th anniversary of International Conference on Metallurgy and Materials, May 18th-20th, Brno, Czech Republic.
- [11Chr] Chrišťelová, J., Rízeková Trnková, L., Pocisková Dimová, K., Ožvold, M.: J. Electron. Mater., 2011, **40**, 1956-1960.

6 The effect of Ni additives in the Cu-Substrate on the interfacial reaction with Sn

A.A. Kodentsov

Laboratory of Materials and Interface Chemistry, Eindhoven University of Technology, The Netherlands

Until fairly recently, people dealing with the packaging technology thought that they had a reasonable notion about the influence of nickel, present in the soldered assembly, on interaction of Cu-substrates with Sn-based alloys and the role of the Kirkendall effect in microstructural development of the solder interconnect. ~~Then, Later, however,~~ elementary, ~~but~~ carefully controlled, experiments ~~disabused them. It~~ led to a series of surprising discoveries and to a new picture of the reaction behaviour of the Sn-Cu(Ni) system [04Pau.01Obe].

In Fig. 6.1 a representative microstructure of the reaction zone developed in the Cu/Sn diffusion couple after annealing at 215 °C in vacuum. One can see two product phases are formed. This is exactly what was expected from the binary Cu-Sn phase diagram (Fig. 6.2). The product layers in the reaction zone are bound by somewhat wavy interfaces. This might be attributed to the influence of ~~short-circuit (mainly grain boundary diffusion)~~ and diffusion anisotropy on the overall mass-transport across the intermetallic layers, although absolute proof is lacking.

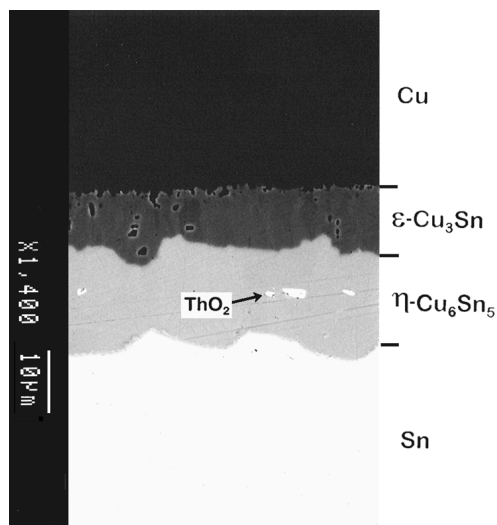


Fig. 6.1: Back-scattered Electron Image (BEI) of the diffusion zone developed between Cu and Sn after reaction at 215 °C in vacuum for 225 hours. ThO₂-particles (“white contrast”) were used as Kirkendall markers.

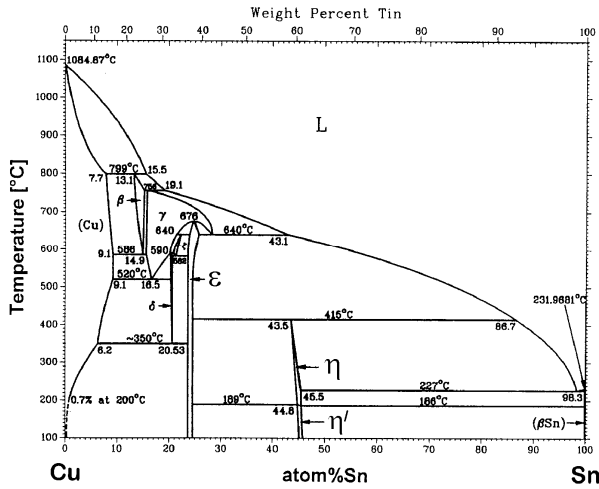


Fig. 6.2: The binary Cu-Sn phase diagram.

~~From the position of the Kirkendall markers (ThO_2 particles), the ratio of the volume intrinsic fluxes of the components in the $\eta\text{-Cu}_6\text{Sn}_5$ layer can be found graphically using the procedure explained in Fig. 6.3.~~

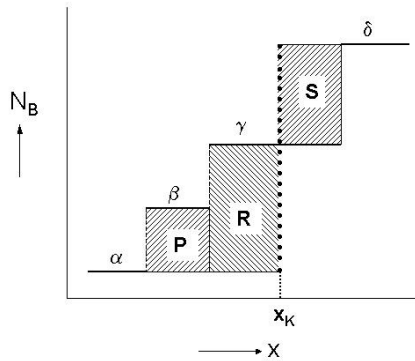


Fig. 6.3: Distribution of component B across the diffusion zone of a hypothetical reaction couple of a binary A-B system (schematically) with product layers of the stoichiometric β - and γ - phases growing between the line-compounds α and δ (x_K is the position of the Kirkendall plane).

The ratio of intrinsic diffusivities of the species in an intermetallic compound can be determined using the diffusion couple technique. If, after interaction, the

Kirkendall plane is found inside a layer of a stoichiometric phase growing in a semi-infinite diffusion couple, this ratio can readily be ~~again~~ obtained by a graphical method as explained in Fig. 6.3.

$$\frac{|J_B|}{|J_A|} = \frac{D_B V_A}{D_A V_B} = \frac{N_B^+ \left[\frac{P}{V_m^\beta} + \frac{R}{V_m^\gamma} \right] - N_B^- \left[\frac{S}{V_m^\gamma} \right]}{-N_A^+ \left[\frac{P}{V_m^\beta} + \frac{R}{V_m^\gamma} \right] + N_A^- \left[\frac{S}{V_m^\gamma} \right]}$$

where P, R and S are the hatched areas in Fig. 6.3. V_m^β, V_m^γ are the molar volumes of the product phases β and γ , and N_i is the molar fraction of the component i. The superscripts + and - refer to the molar fraction of component i in the end-members of the diffusion couple. In the case shown in Fig. 6.3, $N_i^+ = N_B(\delta)$ and $N_i^- = N_B(\alpha)$.

It was calculated that in the η -Cu₆Sn₅ layer $\frac{|J_{Sn}|}{|J_{Cu}|} = \frac{D_{Sn} V_{Cu}}{D_{Cu} V_{Sn}} \approx 1.6$, i.e. Sn diffuses (intrinsically!) almost two times faster than Cu does!

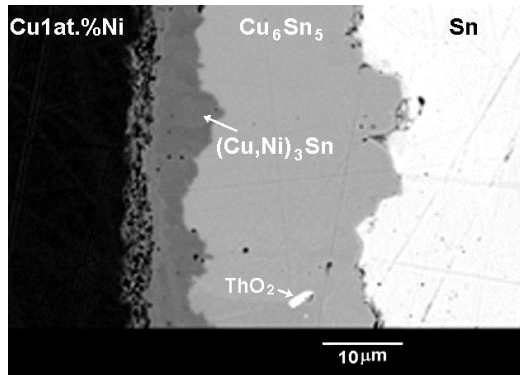


Fig. 6.4: Reaction zone developed between Sn and Cu 1at.% Ni alloy after annealing in vacuum at 215 °C for 400 hrs (BEI).

When 1 at % of Ni is introduced in the Cu-substrate, interfacial interaction at 215 °C resulted in a product pattern (Fig. 6.4) similar to that observed in the annealed binary Cu/Sn couples (Fig. 6.1). From the location of the Kirkendall plane, it is also concluded that the relative (intrinsic) mobilities of the diffusing species in the η -Cu₆Sn₅-product phase layer is not much different from the binary case. However, when 5 at % of Ni is introduced in the Cu-substrate, interfacial interaction at 215 °C

resulted in a completely different reaction product (Fig. 6.5)! No ϵ -Cu₃Sn was detected in the reaction zone, and rather uniform layer of (Cu,Ni)₆Sn₅-phase is generated upon interdiffusion. It is remarkable, that growth kinetics of the (Cu,Ni)₆Sn₅-phase layer is an order of magnitude faster that of η -Cu₆Sn₅-product phase layer in the binary couples.

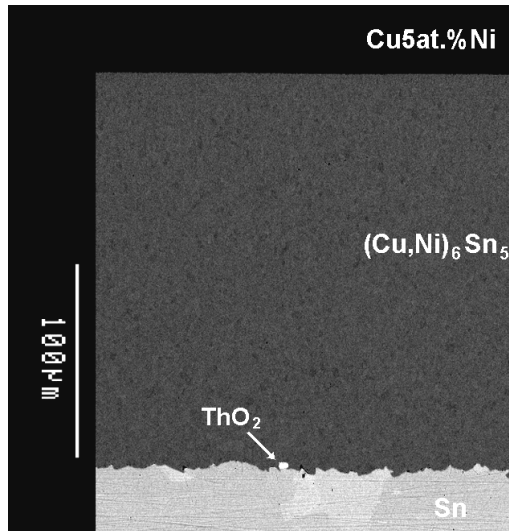


Fig. 6.5: Reaction zone developed between Sn and Cu 5at.% Ni alloy after annealing in vacuum at 215 °C for 400 hrs (BEI).

Another important feature that can be seen from the last micrograph is that after interaction the ThO₂-(Kirkendall) markers end up in the (Cu,Ni)₆Sn₅-phase very close to the reaction product/Sn interface. This implies that contrary to the binary case described above a total intrinsic flux of Sn across the product layer of (Cu,Ni)₆Sn₅-phase is much higher than that of Cu.

Similar reaction behaviour was also observed in the annealed (215 °C) diffusion couples when Ni-content in the Cu-based substrate was between 5 and 25 at.%. This type of reaction behaviour cannot be explained using diffusion path concept. However, it is plausible that the presence of Ni in the “super-lattice” of the Cu₆Sn₅ can stabilize a low-temperature modification (η ’-phase), which is a so-called “long-range period superstructure”. The last statement has to be proved by TEM (Electron Diffraction study).

Any references?

[04Pau] [Paul, A. Doctoral dissertation. Eindhoven University of Technology. 2004.](#)

[01Obe] Oberdorff, P. Doctoral dissertation. Eindhoven University of Technology. 2001.

7 Reactive diffusion at the contact of a solid phase with the melt of solder

J. Drápala, P. Kubíček, P. Harcuba and V. Vodárek

Vysoká škola báňská – Technical University of Ostrava; Faculty of Metallurgy and Materials Engineering, Czech Republic

Problems of reactive diffusion at the ~~contact of interface~~ between solid and liquid phases

~~We will~~This section deals with the problems of ~~dissolving-dissolution~~ of the solid phase A in the melt B, diffusion of atoms of the melt into the solid phase accompanied by creating new phases and/or chemical reactions and finally by diffusion of atoms from the solid phase into the melt. This process usually proceeds at the presence of convections in the melt. During those processes a significant movement of the ~~boundary-interface~~ between the solid phase and the melt takes place, the rate of which depends on the properties of atoms A and B and their interaction, temperature T and time t of the process in question. Furthermore, it depends on the geometric arrangement, on the volume of the melt and conditions enabling or restricting convections in the melt. The relevant phase diagram provides a ~~prediction of newly appearing phases~~~~image of creating phases~~. ~~At-During~~ the reactive diffusion, due to the rate of the solid phase dissolving in the melt, conditions of the equilibrium state do not have to be always met because of non-stationary processes. ~~At-During~~ the diffusion of the melt B atoms into the solid phase A new phases form and grow, i.e. the diffusion processes take place in areas with moving interface boundaries. When new phases ~~create-appear~~ in the course of reactive diffusion, surface and subsurface layers of material of various compositions, properties and thickness also form.

Comment [A13]: This two expressions do not fit well together. Do you mean accompanied by chemical reactions – it also means that new phase is created.

Comment [A14]: Does this sentence describe free different independent processes or free part of one process with free different stages during the time running?

Convection processes in the melt ~~at the dissolving~~ during the dissolution of solid phase

Let us consider an interface between solid phase A and melt B at time $t = 0$ in point $x = 0$ – see Fig. 7.1. A planar interface will be assumed for simplicity, in experiments a cylindrical geometry is often used. Let us suppose that during the ~~dissolution of the solid phase~~ ~~dissolving into~~ the melt ~~with time t~~ the interface ~~boundary~~ moves to the left ~~with time t~~. The rate of this interface movement is usually considerably greater than the growth of newly ~~created-nucleating~~ phases with the melt B atoms in the solid metal A. ~~At the interface boundary~~ a diffusion layer will form in the melt, whose thickness is δ and depends on the size of convections in the melt close to this interface.

Comment [A15]: How many phases grow? One or more?

Comment [A16]: I do not understand this sentence – how can the interface move faster than the new phase grows

Planar dissolving

For the planar interface boundary when the ~~boundary-interface~~ shift ~~during the dissolution~~~~at the dissolving~~ is perpendicular to the interface, the relation is obtained

Comment [A17]: There should be a reference to the paper, where the equations (1,2) are developed.

$$\chi(t) = \frac{\rho_2}{\rho_1} \frac{1 - e^{-K_o t}}{1 - c_o + e^{-K_o t}} l_o, \tag{1}$$

where l_o is the height of the melt column at time $t = 0$, ρ_2, ρ_1 are the solid phase and melt densities, $\chi(t)$ is the shift of the interface boundary at dissolving during dissolution and c_o is the saturated concentration of the metal A in the melt B. The following holds for the time dependence $c(t)$ of the metal A in the melt

$$c(t) = \frac{\chi(t)}{a + \chi(t)}, \quad a = \rho_2 l_o / \rho_1 \tag{2}$$

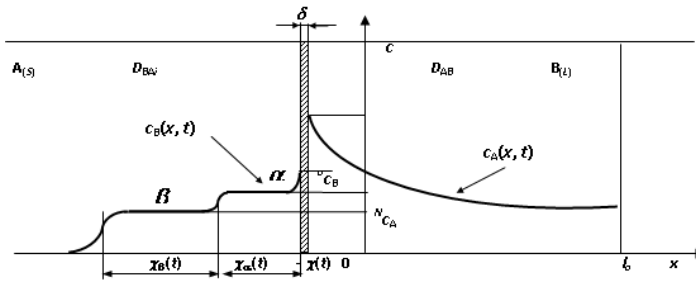


Fig. 7.1 Schematic concentration profiles $c_A(x,t), c_B(x,t)$ at reactive diffusion. $A_{(S)}$ – solid phase; $B_{(L)}$ – melt; $\chi(t)$ – interface boundary movement; δ – thickness of Nernst diffusion boundary layer; N_{CA} – saturated concentration of element A in melt B; D_A – diffusivity of atoms A in melt B; $c_A(x,t)$ – concentration profile of element A in melt B resulting from diffusion and convection; $c_B(x,t)$ – concentration profile of atoms B in solid phase; α, β – phases in metal A created at by reactive diffusion; D_{B1} – diffusivity of atoms B in solid phase A; $N_{CA} + N_{CB} = 1$; $t_2 > t_1$; $\chi_\alpha(t), \chi_\beta(t)$ – function characterizing growth of phases α, β to which correspond concentrations $c_{B\alpha}, c_{B\beta}$ of atoms in solid phase A; x – axis in the centre of concentration profile of diffusion of atoms B from phase β into metal A.

Relation (14) describes the time course-dependence of planar dissolving dissolution. The c_o is the saturated concentration of metal A in melt B and K_o is the rate constant of dissolving dissolution. In deriving neither the diffusion of atoms B of from the melt into solid phase A nor the volume changes at dissolving during dissolution were taken into account in the model. Convections in the melt will influence the rate of dissolving dissolution during the dissolving and therefore the particular-exact value K_o will partly depend on the geometry, above all mainly on the inner diameter of the capillary in which the planar dissolving dissolution takes place. The relation (1) may be used for an approximate evaluation of the rate constant of dissolving K_o under precisely defined experimental conditions. Figure. 7.2 illustrates the calculated courses-dependences $\chi(t)$ for Cu – Sn system. The

Comment [A18]: Height? I think that we speak about horizontal layout. I would prefer the word „width“

Comment [A19]: Where is 1 in the figure?

Comment [A20]: I do not understand this explanation

Comment [A21]: Is this „inner diameter“ equal to the „height“ as defined above?

values of density ratio $\rho_2 / \rho_1 \approx 0.766$ for $T = 400 \text{ }^\circ\text{C}$ and $\rho_2 / \rho_1 \approx 0.762$ for $600 \text{ }^\circ\text{C}$, $l = 1 \text{ cm}$ at $K_0 = (0.3 \div 1.2) \cdot 10^{-5} \text{ s}^{-1}$ were used in the calculations. Time dependences of the component A concentration in the melt, assuming perfect melt homogenisation, are obtained from relations (1) and (2)

$$c_A(t) = c_o (1 - e^{-K_0 t}) \quad (3)$$

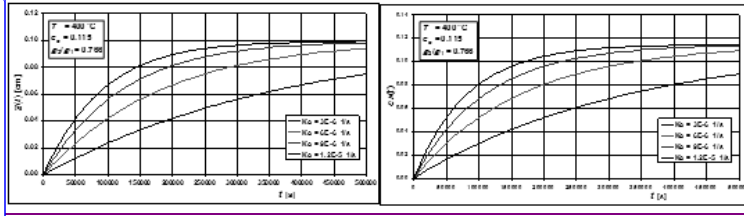
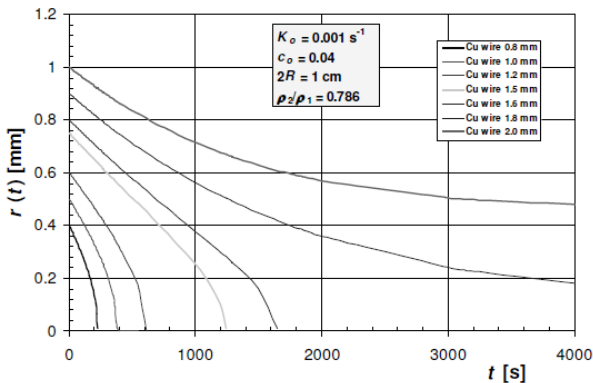


Fig. 7.2 Graphs of functions $\chi(t)$ – eq. (1) and $c_A(t)$ – eq. (3) for temperature the liquid temperature $400 \text{ }^\circ\text{C}$ – in Cu – Sn system in dependence on the rate constant of dissolving and various values of K_0 at for planar dissolution.

Cylindrical dissolving dissolution

A long cylinder of metal A, with radius r_o , is dipped into melt B in the cylindrical orifice, with radius R . During the dissolving, the The initial metal cylinder radius $r(t)$ decreases from the value r_o to $r(t_o) = 0$ during the dissolution. The final equation for decreasing decrease of the cylinder radius with time due to dissolving dissolution is obtained from relation can be calculated as:

$$\frac{r(t)}{r_o} = \sqrt{\frac{1 - c_o A (1 - e^{-K_0 t})}{1 - c_o (1 - e^{-K_0 t})}}, \quad A = \frac{\rho_2}{\rho_1} \left(\frac{R^2}{r_o^2} - 1 \right) + 1 \quad (4)$$



Comment [A22]: This should be L or LO

Comment [AK23]: The legend is not readable. It has to be radone and B&W character has to be respected.

Comment [A24]: No phase nucleation is supposed here?

Comment [A25]: Again the reference to the paper where this is developed is necessary

Fig. 7.3 Time course of dissolving of Cu wires dissolution in molten Sn at the temperature of 350 °C according to eq. (4).

Experimental observation of cylindrical Cu wires dissolving dissolution in Sn

Series of experiments of dissolving dissolution of Cu wires of with various diameters in the melt of pure liquid Sn was carried out at the temperature 350 °C. The diameters of wires were 0.8, 1.5 and 2 mm. The length of the wire dipped into the melt was always 30 mm. To ensure the results of experiment to be as accurate as possible, before the experiment the wires were covered with a layer of Sn before the experiment. Then wire was taken out of the melt after after one minute and its diameters were measured from cross sections in at two or three distances different positions from the end of the wire. The Cu content in Sn melt was established by optical emission spectrometry (OES). In the secondThe experiment was then repeated with a new Cu wire for 2, 3, ..., n minutes experiment a new Cu wire was hold in the melt of pure Sn for 2 minutes and the whole procedure was repeated. Further Cu wires were kept in the melt of pure Sn for 3, 4 up to n minutes, when until nearly the whole wire was dissolved. For diameter $\varnothing = 0.8$ mm was The value $n =$ was 4 minutes for diameter $\varnothing = 0.8$ mm, for $\varnothing = 1.5$ mm $n = 8$ for $\varnothing = 1.5$ mm minutes and 19 for $\varnothing = 2$ mm, was $n = 19$ minutes.

Fig. 7.4 presents the course of reducing decrease of the Cu wire diameter in dependence on the time spent of Cu dissolving in the melt of liquid Sn at the temperature 350 °C. The melt situated was in the graphite block with the orifice, with the 10 mm diameter 10 mm, the height of the melt was always 30 mm at the temperature 350 °C. After reaching the critical diameter of the Cu wire approx. 0.3 to 0.4 mm, the subsequent dissolution process in the upper part just under below the melt surface was very fast since and the wire divided offbroke, and itsThe lower part of the wires remains wasere found on the bottom of the graphite block in the melt lower part. The dissolving experimental dissolution of Cu wires (experiment) in Fig. 4 shows exhibits practically linear dependences (Fig. 7.4), since it was disrupted interrupted prematurely due to the melt progressive impact on the Cu wire "neck". Fig. 7.4 compares experimental results of the Cu wires dissolving dissolution with calculated dependences $r(t)$ according to relation Eq. (4) for the rate constant of dissolving $K_0 = 0.0008$ s⁻¹. There is only good agreement only for the Cu wire with diameter 0.8 mm.

Comment [A26]: Again the legend is not readable and the figure has to be adjusted to B&W

Comment [A27]: Why?

Comment [A28]: I would say, that all the dependences are similar, having only the linear part. On the other hand the agreement with the calculation is O.K up to the moment of premature end.

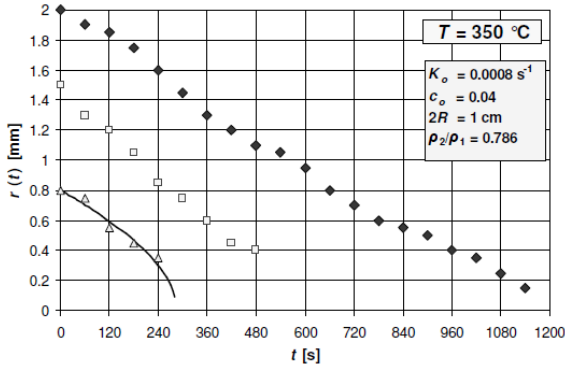


Fig. 7.4 Experimental results of dissolving of Cu dissolution in the melt liquid Sn-wires, diameters of Cu wires were 2, 1.5 and 0.8 mm, in the melt of Sn at the temperature 350 °C and comparison with theoretical calculation according to equation (14) for $K_o = 0.0008 \text{ s}^{-1}$.

Table 7.1: Times t of Cu wires dissolving in the melt of Sn at the temperature $T = 350 \text{ °C}$, values of The concentrations of Cu in the liquid Sn after various times at the temperature $T = 350 \text{ °C}$ determined from diameters of wires – part I., and from chemical analyses of the liquid – part II., and calculated values of the rate constant of dissolving-dissolution K_o for $c_o = 3.4 \text{ wt.\% Cu}$.

I.			II.		
t [s]	$c(t)$ [wt.% Cu]	$K_o \cdot 10^4$ [s ⁻¹]	t [s]	$c(t)$ [wt.% Cu]	$K_o \cdot 10^4$ [s ⁻¹]
180	0.20	3.3	180	0.195	3.3
	0.121	2		0.196	3.2
300	0.196	1.92	300	0.306	3.0
	0.24	2.35		0.194	1.9
360	0.792	6.5	360	0.77	6.3
	0.63	5.1		-	-
420	0.3	2.1	420	0.191	1.34
	0.37	2.6		0.44	3.1
	0.528	3.7		0.68	4.76
540	0.542	3.0	540	0.70	3.8
	0.63	3.4		-	-

Comment [A29]: How did you get this value? Is it the equilibrium solubility of Cu in Sn at given temp.?

Comment [A30]: What do the other lines for the same time mean? Is it the values for different diameters? Should not be the K_o similar in all cases? Why do you have two line for most times and three lines for the time 420s?

Determination of the K_o - rate constant K_o of dissolving Cu dissolution Cu in Sn

The concentrations of Cu in the liquid Sn after various times at the temperature $T = 350 \text{ °C}$ determined from diameters of wires – part I. and from chemical analyses of the liquid – part II., and calculated values of the rate constant of dissolution K_o . The measured values of Cu concentrations in the melt from the change of radius of

Formatted: Indent: First line: 1 cm

dissolving Cu wire and from spectral analysis are together with the calculated values of rate constant of dissolving K_0 are summarized in Table 7.1. The values of rate constants of dissolution K_0 were determined to be in the range of $K_0 = (3 \div 3.8) \cdot 10^{-4} \text{ s}^{-1}$.

Experimental study of growth of phases and reactive diffusion on planar specimens

The uni-directional experiment processes were realized using the by means of "sandwich" specimens. A layer of a particular tin-based solders were inserted between two Cu plates. These were five compositions types of lead-free solder alloys were used: pure Sn, Sn97Cu3, Sn95.5Ag3.8Cu0.7, Sn95Sb5 and Sn91Zn9. The plates of high-purity copper were 0.5 mm thick. The other and dimensions were 20 x 10 mm. Leaves Foils of Sn-based solders, which were inserted between the two Cu plates, were rolled down to the thickness 0.2 mm. Copper plates were covered by spread with a layer of suitable flux. Three plates of the solder alloy were used in experiments, another plate of Cu with flux was placed on them. The soldered joint was created by virtue of using a heating element. The lead-free solders sandwiches were held melted at the temperature $255 \div 285 \text{ }^\circ\text{C}$ (above liquidus) for 40 \div 120 s. Prepared The specimens prepared in this way were used for subsequently experiments during which the specimens were annealed heated at $T = 300 \text{ }^\circ\text{C}$ for and the times were opted to be $t = 18, 24, 48$ and 92 h .

The $\eta\text{-Cu}_6\text{Sn}_5$ grows into during annealing at the temperature $T = 300 \text{ }^\circ\text{C}$ on the interface with the Cu. During heating, at the contact of Cu and molten Sn phase $\eta\text{-Cu}_6\text{Sn}_5$ creates on the Cu surface at the temperature $T = 300 \text{ }^\circ\text{C}$. Copper dissolves in liquid Sn-based solder up to the state of saturation concentration about 4 at.% (2.2 wt.%) Cu. As a consequence of Sn-diffusion into solid Cu, phase η grows with time and subsequently phase ϵ (Cu_3Sn , 75 at.% Cu and 25 at.% Sn) creates appears close to the towards pure Cu. After heating time t The specimens were cooled in the air after annealing and the temperature decreasedopped relatively quickly below the eutectic temperature $227 \text{ }^\circ\text{C}$. The joint Cu/Sn95.5Ag3.8Cu0.7 is shown documented in Fig. 7.5 for after $t = 24$ hours of annealing as an example.

Comment [A31]: How did you determine this? The values in the table are from 1.3 to 6.4 which more less makes any statistics impossible. There should be some conclusion about the mason for such a great distribution

Comment [A32]: This charter should precede the chapter 7.6 as it corresponds to the organization of the theoretical sections. The second possibility is to put it immediately behind the relevant theoretical parts.

Formatted: Indent: First line: 1 cm

Comment [A33]: At least basic composition should be given here

Comment [A34]: Here I do not understand this sentence at all.

Comment [A35]: Do you really mean pure Sn or Sn-based solder

Comment [A36]: You used the value 3.5 wt.% in previous section about cylindrical growth. Why the difference?

Comment [A37]: Do really the new phases grow in to the sold Cu (on the expenses of Cu). In the previous sentence you speak about the dissolution of Cu in the solder up to the saturation. This is not quite clear, this should be clarified.

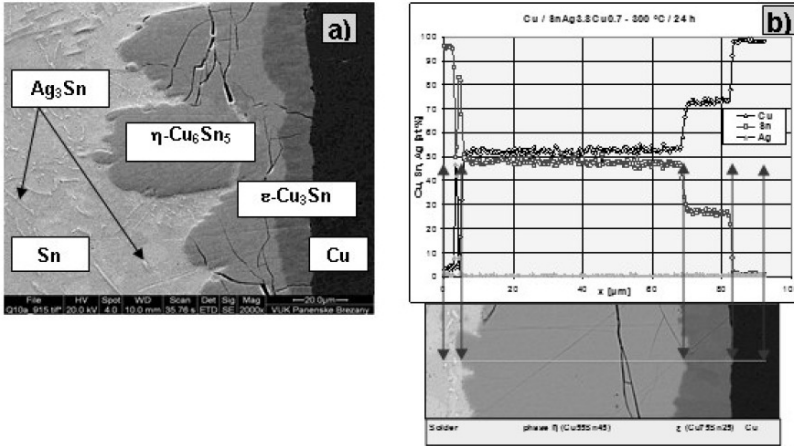


Fig. 7.5 Microstructure a) and concentration profiles b) in the joint Cu/SnAg3.8Cu0.7 annealed at 300 °C for 24 hours.

Comment [A38]: Format it as in the case of previous figures

The growth of phase ε should proceed with time according to parabolic law $\chi_\epsilon(t) = \alpha \sqrt{t}$ where $\chi_\epsilon(t)$ is the thickness of phase ε and α is the constant which characterizes the rate of phase growth. The values $\chi_\epsilon(t)$ can be obtained experimentally metallographically using the metallographic pictures from a relatively large areas. The evaluated values α from the metallography and X-ray EDX microanalysis are presented in Table 7.2. The calculated values α for joints Cu/Sn and Cu/CuSn3 joints by from EDX measurements were in very good agreement. They were determined for $t = 24$ and 48 h.

Comment [A39]: Very good agreement with what? What do you mean by Cu/Sn and Cu/CuSn3 joints? Shouldn't be Cu₃Sn? I thought that the joint were between the the solid Cu and Sn-based solder. Do you mean the interface inside the joint?

Table 7.2 Evaluation of the rate of growth of phase ε in „sandwich“ specimens at temperature $T = 300$ °C.

EDX analysis	t [h]	$10^6 \cdot \alpha$ [cm/s ^{1/2}]	$10^6 \cdot \text{mean } \alpha$ [cm/s ^{1/2}]	Metallography	t [h]	$10^6 \alpha$ [cm/s ^{1/2}]	$10^6 \text{ mean } \alpha$ [cm/s ^{1/2}]
Cu/Sn	24	3.23	3.33	Cu/Sn	18	5.84	5.57
	48	3.43			24	5.10	
	24	3.16	48		4.38		
	48	3.34	92		6.95		
Cu/Sn3	18	6.12	4.76	Cu/Sn3	18	6.50	5.41
	24	3.42			24	6.23	
	48	4.30			48	4.0	
	92	5.21			92	4.92	

Comment [A40]: Use the SI units! The mean values calculated from two measurements do not have too much sense, anyway the calculated exp. error should be shown if this value is presented.

Comment [A41]: What does it mean Cu/Sn3 Why are the comparable values obtained from EDX and metallography so different?

Cu/Sn95.5Ag 3.8Cu0.7	18	6.6	4.27
	24	3.63	
	48	2.40	
	92	4.46	

Table 2 Evaluation of the rate of growth of phase ε in „sandwich“ specimens at temperature $T = 300\text{ °C}$.

Tentative calculation of Sn diffusivities at $T = 300\text{ °C}$ based on the from growth of the phase ε into Cu at $T = 300\text{ °C}$

This tentative calculation will be were performed using according to Wagner relation [REF]. From Based on the X-ray analysis of concentration curves we will searched for the size of interval Δx , where the Sn concentration in Cu decreased nearly to zero, more precisely We can estimate the diffusivity D from the value Δx and the known time of annealing t using the equation:

$$\frac{\Delta x}{2\sqrt{Dt}} \approx 1.5; \quad \text{erfc}(1.5) = 0.034$$

From the value Δx and the known time of heating t we will estimate the diffusivity D .

Diffusion joint : Cu/Sn, $t = 48\text{ h}$, $T = 300\text{ °C}$, $\Delta x = 2.0\text{ }\mu\text{m}$, $D \approx 2.6 \cdot 10^{-14}\text{ cm}^2/\text{s}$.

Diffusion joint : Cu/SnCu3, $t = 24\text{ h}$, $T = 300\text{ °C}$, $\Delta x \approx 2\text{ }\mu\text{m}$, $D \approx 5.1 \cdot 10^{-14}\text{ cm}^2/\text{s}$.

Diffusion joint : Cu/ SnZn9, $t = 92\text{ h}$, $T = 300\text{ °C}$, $\Delta x \approx 2\text{ }\mu\text{m}$, $D \approx 1.3 \cdot 10^{-14}\text{ cm}^2/\text{s}$.

Here should be reference section

Comment [A42]: The theoretical explanation is too short

Comment [A43]: There is Cu/Sn3 in the table 2. What is the difference between these joints?

Comment [A44]: SI units!

Anyway, this is not proper form of conclusions.

8 Examination of early stage of intermetallic compound formation during interaction between liquid tin and solid copper substrates

N. Sobczak^{a,b}, A. Kudyba^a, R. Nowak^a, E. Sienicki^b, K. Pietrzak^b

^aFoundry Research Institute, Krakow, Poland

^bMotor Transport Institute, Warsaw, Poland

It is generally accepted that during soldering, the interaction between liquid solder and solid copper is influenced by two processes: 1) the dissolution of solid copper in liquid solder until the solder becomes supersaturated with Cu at the Cu/liquid solder interface and 2) the formation of intermetallic compounds (IMC) at the solder/Cu interface [04Han, 110Is]. The analysis of literature data shows that the Cu₃Sn and Cu₆Sn₅ phases are the common IMCs reported in conventional Sn-based lead-free solder joints with copper. It is believed that both phases can be formed during soldering process as well as during cooling after solidification via thermally activated solid-state diffusion mechanisms. Further development of solid-state IMC growth can take place also during operation of electronic assemblies, especially under thermal cycling conditions.

In order to understand wetting behaviour of liquid solders and factors affecting their solderability it is essential to know which IMC is formed as a first phase and what is the sequence of interfacial IMCs. However, it is not clear which phase is the first one formed due to the direct interaction between liquid solder and solid Cu because of contradicting statements in the literature on the early stage of phase transformation since both Cu₃Sn [04Son,94Mor,89Kle,06Hua,02Cho,09Gon] and Cu₆Sn₅ [04Han,110Is,91Lee,97Lee,10Par,07Sas] are named as the first formed phase in the liquid solder/Cu systems during soldering.

Although the ~~formation of~~ Cu₃Sn phase has the lowest Gibbs Energy in the Cu-Sn system and thus its formation should be more thermodynamically favorable, it is widely accepted, without any clear experimental evidence, that Cu₆Sn₅ is the first phase formed taking into account that the formation of a thick layer of Cu₆Sn₅ is well documented while the Cu₃Sn phase forms a very thin and sometimes difficult to distinguish layer. In order to explain experimental observations, Lee *et al.* [91Lee] proposed the schematic method for the prediction of the first formed IMC at the solder/Cu interface during soldering process using the driving force criterion. They illustrated that despite the fact that Cu₃Sn phase has the lowest Gibbs energy, the Cu₆Sn₅ phase has the highest driving force of the formation under the metastable equilibrium state. Although the authors highlighted that it should not be concluded that the phase with the highest driving force of the formation is always the first formed, they used this fact as a good approximation to explain the formation of an unstable phase at the beginning, as suggested by Lee *et al.* in [97Lee]. A similar approach is actually widely used for simulation of early stage of IMC formation and growth during Pb-free soldering (e.g. [10Par]). The kinetic model based on the principle of maximum degradation rate of the total system free energy proposed by Sasaki *et al* [07Sas] also predicts the Cu₆Sn₅ as the first phase formed at the Sn/Cu interface.

Comment [AK45]: Precise the affiliations

Formatted: Superscript

Experimental verification of these statements is difficult because the contact time used in all reported data on structural characterization of the Sn/Cu interfaces is a few orders of magnitude longer compared to that needed for the formation of the first monolayer of IMC. Therefore, there is little information on the initial stage of the formation of interfacial IMCs [06Yu,08Pan,09Gon]. Moreover, subsequent relatively long-term cooling history of the Sn/Cu couple may also affect the results of structural characterization because of difficulties to distinguish interfaces formed due solid-liquid and solid-solid IMC growth.

The goal of this research was to characterize the interface formed between liquid pure tin and solid copper substrate at the early stage by structural characterization of the Cu surface being in contact with liquid Sn for extremely short time [11Sob][08Now,12Sob].

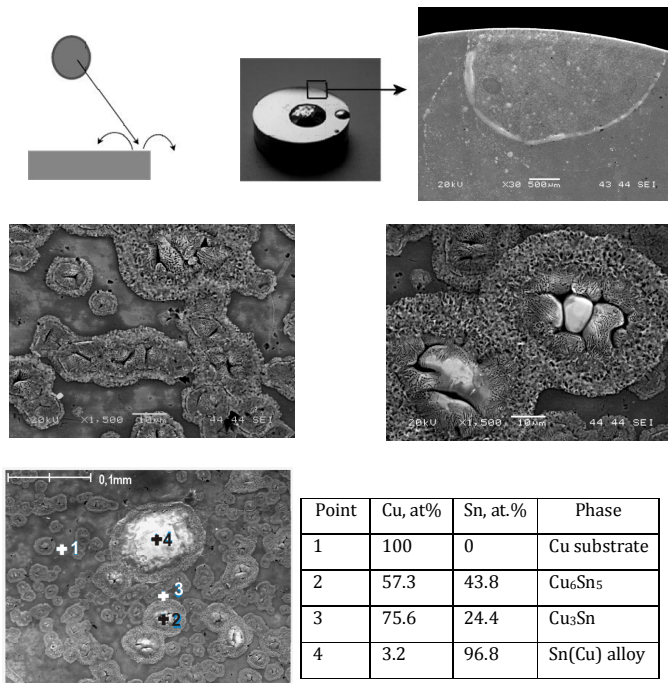


Fig. 8.1: Scheme of the deposition of liquid Sn on solder Cu substrate by shooting from a capillary resulting in the detachment of the mother drop from the substrate and the formation of a few daughter droplets and residual interfaces formed during short time contact and consequently opened due to the drop detachment. SEM images show under different magnification the interface formed between liquid pure tin and solid copper substrate at the early stage by structural characterization of the Cu surface being in contact with liquid Sn for extremely short time.

substrate surface structure being in contact with liquid Sn. Results of local chemical analysis by EDS are collected in the inserted table.

Using dispensed drop wettability set-up equipped with a dosing system [08Sob] the molten Sn droplets interacted with the Cu substrate under ultra high vacuum conditions at a temperature of 250°C. In order to eliminate any side effects the tests were done on perfectly polished Cu substrate (roughness Ra = 30 nm) and Sn liquid that was *in situ* cleaned from primary oxide film directly in a vacuum chamber by applying capillary purification technique [08Now,07Sob]. The time of contact between liquid Sn and solid Cu substrate was believed to be extremely short (milliseconds) since liquid Sn drop was fast sprayed from about 20 mm height by sudden forced action on liquid metal and its squeezing (shooting) from alumina capillary [12Sob]. After the impact on the Cu substrate surface, the mother drop detached from it and fell down outside the substrate while a few small daughter droplets were deposited on the substrate surface.

Detailed structural characterization of the substrate surface after the tests was done under different magnifications using optical microscopy (OM) and scanning electron microscopy (SEM) coupled with EDS analysis assisted with X-ray analysis.

Figures 8.1 and 8.2 show SEM top view images and corresponding EDS analyses of selected places on the substrate surface after the short contact test at 250°C . ~~Figure 8.3 illustrates OM observations of a cross-sectioned sample.~~ Structural observations evidenced that the Cu substrate surface being in contact with liquid Sn is covered with a discontinuous island-like layer of a new product. EDS analysis of such islands shows that mainly they are composed of fine Cu₃Sn precipitates while the Cu₆Sn₅ phase is occasionally noted inside bigger islands (Fig. 8.1). Moreover, inside a few of the biggest islands, the presence of Sn phase containing Cu was also evidenced as a result of the formation of bigger daughter droplets due to the detachment of the mother drop during its impact on the Cu substrate

Formatted: Font: Italic

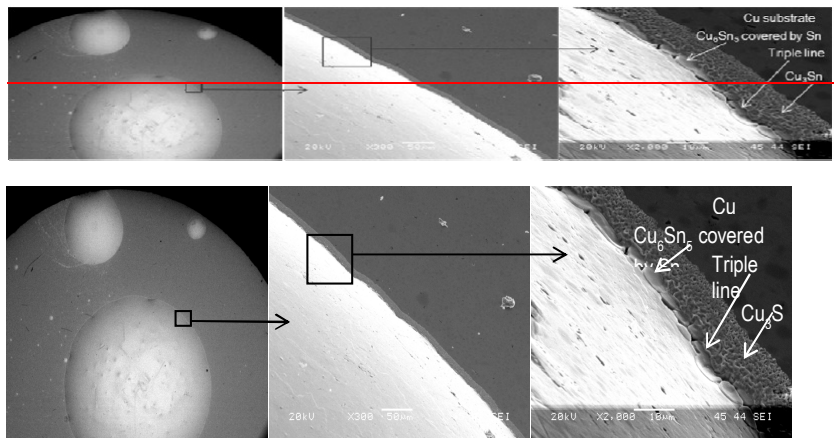


Fig. 8.2: SEM images of the top-view of the substrate surface showing three daughter droplets under magnification increased from left to right with well distinguished Cu_3Sn and Cu_6Sn_5 rings surrounding the droplets [Sob08].

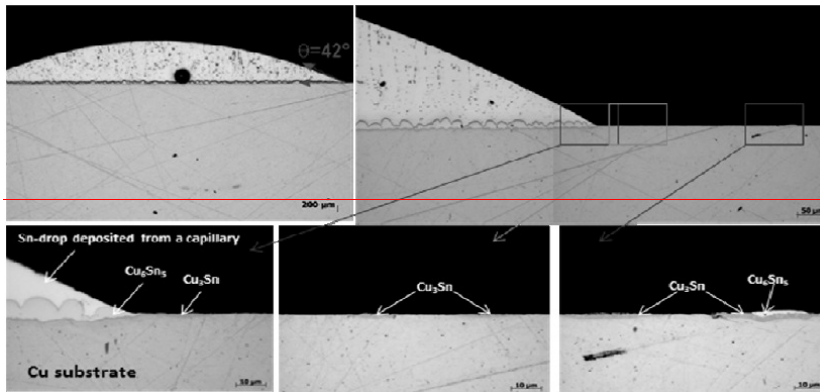


Fig. 8.3: Optical microscopy images of cross-sectioned Sn/Cu couple showing a residual bigger daughter droplet forming the contact angle of $\theta=42^\circ$ and surrounded with small daughter droplets and residual interfaces formed during short time contact and consequently opened due to the mother drop detachment.

Comment [AK46]: B&W format, please. Also, the legend on the last photo is too small to be well readable

Comment [AK47]: Both comments as above in Fig. 2; It was not possible to get good contrast in BW mode

Detailed SEM examination of the area near the biggest daughter droplets (Fig. 8.2) shows that they are surrounded with a layer identified as the Cu_3Sn phase while the Cu_6Sn_5 phase is present in the form of separated large precipitates located between the daughter droplet and the Cu_3Sn layer.

Optical microscopy (OM) analysis observations on the cross-sectioned sample under polarized light [08Now,12Sob] (Fig. 8.3) allowed us to distinguish the Cu_3Sn and Cu_6Sn_5 phases due to difference in its color (dark blue for Cu_3Sn and light blue for Cu_6Sn_5). The results obtained of color optical microscopy characterization confirmed SEM observations and EDS analysis, i.e. the thin layer surrounding the droplet corresponds to the Cu_3Sn phase and most islands also present the Cu_3Sn phase. Only occasionally inside them there are-were the residual fragments of Cu_6Sn_5 phase. Moreover, the Cu_3Sn islands grow inside the Cu substrate. The Cu_6Sn_5 phase forms a thick layer only inside the biggest droplets at its $\text{Cu}_3\text{Sn}/\text{Sn}$ interface. The biggest droplet forms the contact angle of $\theta=42^\circ$ measured at the point corresponding to triple line location and it corresponds to the contact angle formed by liquid Sn(Cu) droplet at the freshly formed Cu_3Sn surface since no extension of the Cu_6Sn_5 phase outside the droplet was noted to occur. -These observations suggest also that individual Cu_6Sn_5 precipitates noted around the droplet during SEM characterization (Fig. 8.2) were initially also located under the liquid droplet and they were opened later during cooling due to liquid metal shrinkage

~~These observations suggest also that individual Cu₆Sn₅-precipitates noted around the droplet during SEM characterization (Fig. 9.2) were initially also located under the liquid droplet and they were opened later during cooling due to liquid metal shrinkage.~~

Formatted: Indent: First line: 0 cm

~~The results of this study on structural~~The characterization of the interface formed at very short contact time and ~~made the in situ accessible~~opened observation at 250°C ~~by of~~ the detachment of the mother drop from the copper substrate under UHV conditions are believed to evidence that under ~~the considered~~ conditions of this study the Cu₃Sn phase is the first phase formed during interaction between liquid residual Sn ~~being~~ in contact with solid Cu by the reaction: 3Cu+Sn = Cu₃Sn. This process is accompanied with Cu consumption (Cu₃Sn growth inside the substrate) and the formation of two interfaces, i.e. stable Cu/Cu₃Sn interface and unstable Cu₃Sn/Sn interface. In the next stage of interaction, the freshly formed Cu₃Sn phase reacts with liquid Sn to form Cu₆Sn₅ phase resulting in Cu₃Sn consumption ~~(2Cu₃Sn+3Sn_l = Cu₆Sn₅).~~

The proposed explanations are in a good agreement with recent experimental results on investigation of the interfacial reaction in Sn/Cu system by in situ stress measurements using nanolayers of Cu-Sn films [04Son]. They are also in agreement with explanations based on experimental observations of solder joints, i.e. the Cu₆Sn₅ layers are formed preferentially when there is an excess of Sn while the Cu₃Sn phase is formed preferentially when there is an excess of Cu [94Fre, 89Kle] because the solder volume affects the interfacial reaction at the Sn/Cu interface during soldering. This explains why the Cu₃Sn phase can be only observed in the smallest bump [06Hua]. It is also in agreement with experimental results by Choi *et al.* [02Cho], who reported that the Cu₃Sn phase formed first in the Cu balls plated with ~~the smallest~~ small volume of Sn.

Comment [AK48]: What is meant by the smallest amount? It should be somehow explained.

~~But the most interesting results were published by Gong *et al* in 2009 [09Gon], i.e. after our first report on the COST MP0602 Meeting in 2008 [08Now]. Gong *et al* examined the initial formation of intermetallic compounds between Cu under-bump metallization and molten SnAgCu solder by removing the liquid solder from the substrate and rapidly cooling immediately after the interfacial phases have formed, which are test conditions comparable to ours. In their report [09Gon], the microstructure of interfacial reactants formed on Cu pads looks similar to that shown in Fig. 1. For detailed structural characterization of these reactants Gong *et al* applied transmission electron microscopy coupled with focused ion beam technique for sample preparation. They evidenced that a Cu₃Sn layer is formed ahead of the liquid solder on the Cu substrate while the liquid solder subsequently wets and spreads on this existing Cu₃Sn layer, forming a Cu₆Sn₅ layer between the liquid phase and Cu₃Sn.~~

Formatted: Subscript

Formatted: English (U.S.)

Similar ~~effect conditions for interaction in a solder/Cu couple as it was realized in the test by Gong *et al.* [09Gon]~~ can be achieved by using fast removing of excess of liquid solder by applying pressure during bonding and fast squeezing liquid phase outside the Cu/solder/Cu joints, ~~as As~~ reported in [10Ber, 83Sob], ~~it allows to produce the Cu/Cu joints with only one interfacial layer composed of Cu-rich intermetallic phase.~~

References

- [04Han] "Handbook of Lead-free Technology for Microelectronic Assembly". New York: Marcel-Dekker, 2004.
- [110ls] Olson, A.: www.stielelectronicsinc.com
- [91Lee] Lee, H.M., Allen, S.M., Grujicic, M.: Metall Trans, 1991, **22A**, 2869.
- [97Lee] Lee, B.J., Hwang, N.M., Lee, H.M.: Acta Mater, 199, **45**, 1867-1874.
- [10Par] Park, M.S., Arroyave, A.: Acta Mater., 2010, **58**, 4900-4910.
- [07Sas] Sasaki, T., Tanaka, M., Ohno, Y.: Materials Letters, 2007, **61**, 2093-2095.
- [04Son] Song, J.Y., Yu, J., Lee, T.Y.: Scripta Mater, 2004, **51**, 167-170.
- [94Fre] Frear, D.R., Burchett, S.N., Morgan, H.S., Lau, J.H. (ed): "The Mechanics of Solder alloy Interconnects", New York, Van Nostrand Reinhold, 1994, p.15.
- [89Kle] Klein Wassink, R.J.: "Soldering in Electronics", 2nd edition, Scotland-Electrochemical Publications Ltd., 1989, p. 155.
- [06Hua] Huang, Z., Conway, P.P., Jung, E., Thomson, R.C., Lui, C., Loeher, T., Minkus, M.: J Electron Mater, 2006, **35**, 1761-1772.
- [02Cho] Choi, W.K., Kang, S.K., Shih, D.Y.: J Electron Mater, 2002, **32**, 1283.
- [06Yu] Yu, C.H., Lin, K.L.: Chem. Phys. Lett. 2006, **418**, 433.
- [08Pan] Pan, C.C., Yu, C.H., Lin, K.L.: Appl. Phys. Lett., 2008, **93**, 061912.
- [09Gon] Gong, J., Liu, C., Conway, P., Silberschmidt, V.V.: Scripta Mater. 2009, **60**, 333-335.
- [08Now] Nowak, R., Sobczak, N., Radziwill, W., Kudyba, A., Sienicki, E., Pietrzak, K.: "Structural characterization of the Sn/Cu interface formed during extremely short time of contact between liquid tin and copper substrate". Abstract Book Joint Working Group Meeting COST MP0602, 21 – 22 February, Genova, Italy.
- [10Ber] Berghmans, F., Mignani, A.C., van Hoof, C.A. (ed): "Optical Sensing and Detection", Proc. SPIE Vol. 7726, 772611; doi: 10.1117/12.855752.
- [83Sob] Sobczak, N.L., Choroszajlov, V.G., Pavlova, S.N.: Trudy LPI, 1983, **395**, 19-21.
- [14Sob12Sob] Sobczak, N., Kudyba, A., Nowak, R., Sienicki, E., Pietrzak, K.: Prace Instytutu Odlewnictwa, 2012~~4~~.

Formatted: Justified, Indent: Left: 1 cm, Hanging: 1,25 cm, No bullets or numbering

Formatted: Font: Bold

Formatted: Font: Bold

Formatted: Font: Cambria

Formatted: Font: Bold

Formatted: Indent: First line: 0 cm

9 Models on surface energy

R. Novakovic

National Research Council, Inst. for Energetics and Interphases (CNR-IENI),
Genoa, Italy.

Introduction

Interfaces are an integral part of the materials structure and, due to their relatively discontinuous character, are often considered as “boundary aspects” of bulk materials. The properties of interfaces or surfaces are strongly related to the solid-vapour, liquid-vapour and solid-liquid interfacial or surface energies. Different experimental techniques have been developed to measure the surface tension [75Mur], i.e. interfacial energy of a liquid-vapour, γ_{LV} . Moreover, combined to the wetting experiments, which that determine the contact angle, θ , between a liquid alloy and a solid substrate is one of approaches that make possible can be used to estimate a the solid-liquid surface energy, γ_{SL} , the most difficult to be determined [99Eus]. To compensate the lack of experimental data on a solid-vapour surface energy, γ_{SV} , the Skapski model [56Ska] or some of models reported in [99Eust] can be used to estimate the solid-vapour surface energy, γ_{SV} .

Comment [AK49]: The whole sentence is a bit too complicated. Is it good English? I would recommend to simplify this

Formatted

9.1.1 Wetting experiments and interfacial energies

The wetting phenomena of molten alloy on solid substrate depend on the bonding characteristics of liquid alloys and solid substrates as well as on the magnitude of interactive forces at the interface. An established method for studying the interfacial phenomena is a sessile drop method that makes possible to estimate the interfacial energies [02No1]. The basic equation that describes the interfacial energies of a liquid phase in contact with a solid phase is the Young equation:

$$\gamma_{SV} = \gamma_{SL} + \gamma_{LV} \cos \theta \quad (1)$$

The work of adhesion, W_A , is defined by the Dupré equation as:

$$W_A = \gamma_{SV} + \gamma_{LV} - \gamma_{SL} \quad (2)$$

Combining Eqs.(1) and (2) the following equation is obtained:

$$W_A = \gamma_{LV} (1 + \cos \theta) \quad (3)$$

The work of adhesion and the interfacial energies can be calculated by Eqs.(1-3) using the experimental data on the contact angle and the surface tension over a composition range.

Surface energy of solid metals

Numerous attempts to calculate the surface energy of metal both on an empirical and a theoretical basis have been done, but the discrepancies between calculated and experimentally determined surface energies have been so great in

many cases, and a general formulation, valid for all metals was not found. The original theoretical formalism proposed by Skapski [56Ska] makes possible to calculate the surface energy or surface tension of solid metals as:

$$F_s = 1.2(\gamma_{LV})_m + 0.45(T_m - T) \quad (4)$$

where $(\gamma_{LV})_m$ is the liquid-metal surface energy at the melting point, T_m is the melting point and T is a temperature below the melting point.

Comment [AK50]: As before – Rada speaks about liquid-metal energy and the subscript is LV. Is it correct??? Yes, it relates the γ_{LV} with γ_{SV}

Surface energy of liquid metals and alloys

The surface properties are of great importance due to their relevance for all industrial processes that involve the presence of the liquid phase. Due to difficulties to perform surface tension measurements, in particular at high temperatures, only few reference data on liquid metals are available [84Luk, 93Kee, 06Mil]. Concerning the surface tension data on binary systems they are still only few, and in the case of complex alloys a nearly complete lack of data is evident [93lid]. The missing data can therefore be estimated by using theoretical models described in [10Egr]. ~~In the present work next sections, only the basic equations related to thermodynamic models to the calculations of the calculate surface tension are given.~~

Comment [AK51]: Where are the equation given. The section should be mentioned here.

Thermodynamic modelling of surface tension of alloys

The interactions between A and B atoms and their bond energies play a key role in elucidating the mixing behaviour in a binary alloy. From this point of view the condition when ~~hetero-coordinated~~ A-B atom pairs are energetically preferred as nearest neighbours over self-coordinated A-A or B-B, or vice versa, leads to classifying the binary alloys into either compound forming [74Bh1, 74Bh2, 95Sin] or segregating systems [97Sin]. In the last fifty years Butler's equation [32But] has been widely used to calculate the surface tension of binary and ternary liquid alloys. Thermodynamic solution models, such as the regular solution model, the subregular solution model, the compound formation model (CFM), the self-aggregating model (SAM), can be used in conjunction with Butler's equation [02No2, 74Bha1, 87Sin, 87Spe, 99Tan] to describe the surface properties of an alloy system. The choice of a model depends on the thermodynamic data on mixing and on a type of the phase diagram.

Comment [AK52]: Is this word really the best?

9.1.29.1.1 Butler's equation and its applications

In the Butler model the surface is considered as an additional thermodynamic phase in equilibrium with the bulk. Conventionally, the interface between a bulk liquid solution and its equilibrium vapour as a surface phase is assumed to be a monolayer. By applying the simplest form of the quasi-lattice theory (QLT) to the surface monolayer and directly using experimental values of the bulk activities, one can calculate the surface tension of binary alloys without the use of any adjustable parameters [52Gug]. Based on Butler's model, the surface tension of liquid binary ($i = 1, 2; j = 1$) or ternary ($i = 1, 2, 3; j = 2, 3$) alloys can be calculated by:

$$\gamma = \gamma_i + \frac{RT}{S_i} \ln \frac{X_i^s}{X_i^b} + \frac{I}{S_i} [G_i^{xs,s}(T, X_{j(j=2,3)}^s) - G_i^{xs,b}(T, X_{j(j=2,3)}^b)] \quad (5)$$

where R , T , γ_i , S_i are gas constant, temperature, surface tension of pure components and surface area, respectively. X_j^k denotes an alloy composition where the subscript j and superscript k refer to the corresponding component in the bulk and the surface phase. $G_i^{xs,b}(T, X_{j(j=2,3)}^b)$ and $G_i^{xs,s}(T, X_{j(j=2,3)}^s)$ are partial excess Gibbs energies of a component i in the bulk phase and the surface phase, respectively. Usually, the Gibbs excess free energies of binary systems are given by Redlich-Kister polynomials, in the form:

$${}^{xs}G_L^{A-B} = X_A \cdot X_B \cdot \sum_{v=0}^n L_v \cdot (X_A - X_B)^v \quad \dots \quad L_v = A_v + B_v \cdot T \quad (6)$$

Assuming that ternary interactions in the liquid phase are smaller than those which arise from the binary terms, the Gibbs excess free energies of a ternary system can be calculated combining the corresponding values of its binary subsystems [98Sau]. An example of calculations (Eqs.(5-6)) is shown Fig. 9.1.

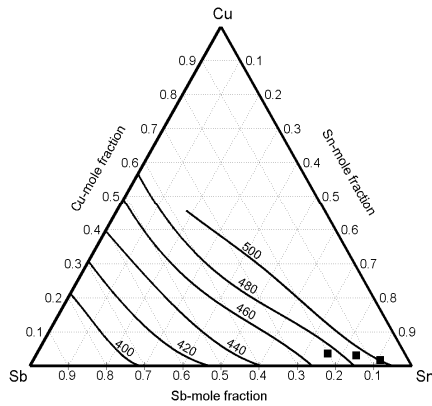


Fig. 9.1: Iso-surface tension lines of liquid Sn-Sb-Cu alloys calculated by Butler's model in the regular solution approximation at 873 K and the surface tension experimental data (in mN/m) of three lead-free solders [10Ple].

Compound Formation Model (CFM)

Many alloy systems are characterised by the formation of well-defined intermetallic compounds in the solid state. Experimental evidence has been found that such alloys exhibit a strong or weak compound forming tendency also in the liquid state [84Ste], but the compositional location of various anomalies does not correlate at all precisely with the stoichiometry of intermetallics present in the solid state. The CFM has been developed by Bhatia et al. [74Bh1, 74Bh2, 82Bh1, 82Bh2, 87Sin] in the framework of the statistical mechanical theory in conjunction with the quasi lattice theory (QLT) [52Gug]. The generalised CFM formalism treats an alloy as

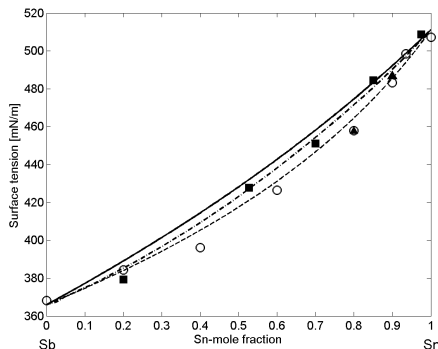
a pseudoternary mixture of A atoms, B atoms and $A_\mu B_\nu$ ($\mu, \nu = 1, 2, 3, 4$) group of clusters with the stoichiometry of an energetically favoured intermetallic phase present in the solid state, all in chemical equilibrium with one another. There are two limiting cases where appropriate approximations for strongly and weakly interacting systems allow us to approach correctly the heteroatomic interactions of atoms in alloy melts. Usually, the normalised form of the Gibbs free energy of mixing of the liquid phase at the equiatomic composition, G_M / RT , is used to “quantify” a compound formation tendency in liquid alloys. Values between -1 and -2 are characteristic for weakly interacting systems, such as the Cu-Sn [10Egr], Bi-Pb [02No2], Sb-Sn [11Nov]..., while those lower than -3 are typical for strongly interacting systems, such as the Bi-Mg [74Bh1], Au-Sn [05No2], Al-Ni [10Egr], etc. Mathematical details of the CFM formalism including the basic differences between the two approximations are summarized in [10Egr]. In a variant of the compound formation model (CFM) appropriate for weakly interacting binary alloy systems, the surface tension, γ , can be calculated by:

$$\gamma = \gamma_i + \frac{k_B T}{\alpha} \ln \frac{C_i^s}{C_i} + \frac{W}{\alpha} [p(f^s - f) - qf] + \sum_{i,j=A,B} \frac{\Delta W_{ij}}{\alpha} [p(f_{ij}^s - f_{ij}) - qf_{ij}] \quad (7)$$

and

~~$$\gamma = \gamma_B + \frac{k_B T}{\alpha} \ln \frac{(1-C^s)}{(1-C)} + \frac{W}{\alpha} [p(\phi^s - \phi) - q\phi] + \sum_{i,j=A,B} \frac{\Delta W_{ij}}{\alpha} [p(\phi_{ij}^s - \phi_{ij}) - q\phi_{ij}] \quad (8)$$~~

where k_B is the Boltzmann constant, C_i and C_i^s are the bulk and surface compositions, γ_i the surface energy of pure i ($i=A$ or B), W and W_{ij} are interaction energies, p and q are surface coordination fractions and α is surface area. ~~C and C^s are compositions~~ and f_{ij}, f_{ij}^s ($i, j = A, B$) are concentration functions for the bulk and surface phases, ~~respectively with analytical expressions as reported in [82Bha1]~~. An application of the CFM in a weak interaction approximation to calculate the surface tension is shown in Fig. 9.2.



Comment [AK53]: Are both equations necessary?

Formatted: Lowered by 6 pt

Formatted: Font: Symbol

Formatted: Subscript

Fig. 9.2: Surface tension of liquid Sb-Sn alloys at T = 905 K. (▲, ○, ■) refer to the literature [03Gas, 10Ple, 11Nov], respectively. The surface tension isotherms: the CFM (—); the regular solution model (·-·-·-); the ideal solution model (-----).

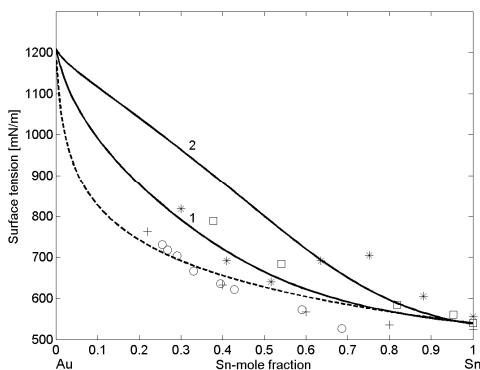
In contrast to weakly interacting alloys, strong interactions in alloy melts are described by introducing an energetic term, and the number of aggregates [05No2] in an explicit way into the total Gibbs free energy of mixing. The basic idea of the compound formation model (CFM) for strongly interacting binary alloys is directly related to the quasi lattice theory. Accordingly, the constituents of a binary liquid alloy, i.e. *A* -atoms, *B* - atoms and *A_μB_ν*- associates are located on lattice sites and can be taken as “monomers” and “(μ + ν) - mer”, respectively. The CFM approximation for strongly interacting alloys follows Butler’s concept [32But] and relates the bulk and the surface properties through the grand partition functions [52Gug] providing a relation between bulk and surface compositions in terms of surface tension, γ, as:

$$\gamma = \gamma_i + \frac{k_B T}{\alpha} \ln \frac{C_i^s}{C_i} + \frac{k_B T}{\alpha} \ln \frac{a_i^s}{a_i} \tag{9}$$

and

$$\gamma = \gamma_B + \frac{k_B T}{\alpha} \ln \frac{C_B^s}{C_B} + \frac{k_B T}{\alpha} \ln \frac{a_B^s}{a_B} \tag{10}$$

where γ_i and C_i ($i = A$ or B) are the surface tensions and atomic concentration of the pure components and atomic concentrations, respectively. a_i and a_i^s are activity coefficients of the bulk and the surface phase, respectively. An example of the application of the CFM to calculate the surface tension of strongly interacting systems such as liquid Au-Sn alloys is shown below in Fig. 9.3.



Comment [AKS4]: Again, do we need both equations here?

Formatted: Lowered by 2 pt

Fig. 9.3: The Au-Sn surface tension isotherms calculated at $T = 823$ K together with the literature data reported in [05Nov2]: 1 – the regular solution model; 2 – the CFM; ----- the ideal solution model.

Conclusion –

Maybe some very short conclusions could be placed here. Surface and interfacial energies of solid and liquid alloys are still scarce. In this chapter, the basic equations of a number of thermodynamic models for calculating the surface energy of liquid alloys are discussed. Solid-liquid interfacial energies can be estimated from the surface energies using contact angle measurements.

References

- [75Mur] Murr, L.E.: "Interfacial Phenomena in Metals and Alloys", Addison-Wesley Publishing Company, Massachusetts, 1975.
- [99Eus] Eustathopoulos, N., Nicholas, M., Drevet, B.: "Wettability at high temperatures", 1st ed., Pergamon Materials Series vol. 3, Oxford, 1999.
- [56Ska] Skapski, A.S.: Acta Met., 1956, **4**, 576-582.
- [02No1] Novakovic, R., Ricci, E., Muolo, M.L., Giuranno, D., Passerone, A.: Intermetallics, 2003, **11**, 1301-1311.
- [84Luk] Lucas, L.D. : Tension superficielle. Traité Matériaux. Métalliques. Techniques de l'Ingénieur Paris; 1984. M67.
- [93Kee] Keene B.J.: Int. Mater. Rev., 1993, **38**, 157-192.
- [06Mil] Mills, K.C., Su, Y.C.: Int. Mater. Rev., 2006, **51**, 329-351.
- [93lid] Iida, T., Guthrie, R.I.L.: "The physical properties of liquid metals", Clarendon Press, Oxford, 1993.
- [10Egr] Egrý, I., Ricci, E., Novakovic, R., Ozawa, S.: Adv. in Colloid and Interface Sci., 2010, **159**, 198–212.
- [74Bh1] Bhatia, A.B., Hargrove, W.H.: Phys. Rev. B, 1974, **10**, 3186-3196.
- [74Bh2] Bhatia, A.B., Hargrove, W.H., Thornton, D.E.: Phys Rev B, 1974, **9**, 435-444.
- [95Sin] Singh, R.N., March, N.H., Westbrook, J.H., Fleischer R.L. (eds): "Intermetallic Compounds", Principles and Practice, Vol. 1., John Wiley & Sons, Chichester, 1995. p. 661-686.
- [97Sin] Singh, R.N., Sommer, F.: Rep. Prog. Phys., 1997, **60**, 57-150.
- [32But] Butler, J.A.V.: Proc. Roy. Soc., 1932, **A135**, 348-375.
- [02No2] Novakovic, R., Ricci, E., Giuranno, D., Gnecco, F.: Surf. Sci., 2002, **515**, 377-389.
- [87Sin] Singh, R.N.: Can. J. Phys., 1987, **65**, 309-325.
- [87Spe] Speiser, R., Poirier, D.R., Yeum, K.: Scripta Metall., 1987, **21**, 687-692.
- [99Tan] Tanaka, T., Hack, K., Hara, S.: MRS Bulletin 1999, **April**, 45-50.
- [52Gug] Guggenheim, E.A.: "Mixtures", Oxford University Press, London, 1952.
- [98Sau] Saunders, N., Miodownik, A.P.: "CALPHAD (Calculation of Phase Diagrams): A Comprehensive Guide", 1st ed., Pergamon, Exeter 1998.
- [10Ple] Plevachuk, Yu., Hoyer, W., Kaban, I., Köhler, M., Novakovic, R.: J. of Mater. Sci., 2010, **45**, 2051-2056.
- [84Ste] Steeb, S., Falch, S., Lamparter P.: Z. Metallkde, 1984, **75**, 599-613.
- [82Bh1] Bhatia, A.B., Singh, R.N.: Phys. Chem. Liquid, 1982, **11**, 285-313.
- [82Bh2] Bhatia, A.B., Singh, R.N.: Phys. Chem. Liquid, 1982, **11**, 343-351.
- [11Nov] Novakovic, R., Giuranno, D., Ricci, E., Delsante, S., Li, D., Borzone, G.: Sur. Sci., 2011, **605**, 248-255.

- [05No2] Novakovic, R., Ricci, E., Gnecco, F., Giuranno, D., Borzone, G.: Surf. Sci., 2005, **599**, 230 - 247.
- [03Gas] Gąsior, W., Moser, Z., Pstruś, J.: J. of Phase Equilibria, 2003, **24**, 504-510.

10 Phase-field simulations of growth and coarsening in lead-free solder joints

N. Moelans

KU Leuven, Department of Metallurgy and Materials Engineering, Belgium.

Introduction

The phase-field approach has proven to be powerful tool for simulating the microstructure evolution during many different materials processes, such as solidification, precipitation, martensitic transformations and coarsening [08Moe]. It is characteristic for phase-field models that the interfaces are assumed to be diffuse and have a finite width. An important advantage is that phase-field models can tackle the evolution of arbitrarily complex morphologies. To reduce the computational requirements, so called ‘thin interface’ phase-field models have been developed. In these models the interfacial width is considered as a numerical parameter that can be varied within a certain range for computational reasons without affecting other system properties, such as interfacial energy, diffusion behavior or bulk thermodynamic properties. In this way, it has become feasible to perform accurate 3D simulations for realistic dimensions.

Recently, a quantitative phase-field model for growth and coarsening in multi-component multi-phase systems was developed by the author [11Moe]. The model can treat coarsening, phase transitions and diffusion in systems with an arbitrary number of phases and components and considers the effect of misorientation and inclination dependence of bulk and interfacial properties. It allows for a high controllability of the accuracy of the simulation results. In this paper, the model is applied to study growth and coarsening of IMC phases in Cu/Cu-Sn solder joints and Kirkendall voiding in 2-phase materials.

Phase-field model

Fig. 10.1 ~~Figure 10.1~~ shows schematically how the microstructure is represented by means of continuous field variables $\eta_{\rho i}(\mathbf{r}, t)$ for phases and grains and $x_k(\mathbf{r}, t)$ for spatial variations in composition [08Moe2]. The evolution of the field variables is obtained by solving numerically evolution equations derived from a free energy functional according to the principles of linear non-equilibrium thermodynamics. The total energy F of a heterogeneous system is formulated as a functional of all field variables and consists of an interfacial and bulk part

$$F(\eta_{(Cu),1}, \dots, \eta_{Cu6Sn5,i}, \dots, \eta_{\rho i}, \dots, x_{Cu}, x_{Sn}) = \int_V f_{int}(\vec{\eta}) + f_{bulk}(\vec{\eta}, \vec{x}) dV \quad (1)$$

The bulk free energy density f_{bulk} is related to the molar Gibbs energies $G_m^\rho(x_1, \dots, x_{C-1}, T^*)$ of the different phases as a function of composition for a constant temperature T^*

$$f_{bulk} = \sum_{\rho} \left(\phi_{\rho} \frac{G_m^{\rho}(x^{\rho}, T^*)}{V_m} \right), \quad (2)$$

Field Code Changed

Field Code Changed

with V_m the molar volume, $\phi_\rho = \sum_i \eta_{\rho i} / \left(\sum_i \eta_{\rho i}^2 + \sum_{\sigma \neq \rho} \sum_i \eta_{\sigma i}^2 \right)$ the local fraction

of phase ρ and $\bar{x}^\rho = (x_{Cu}^\rho, x_{Sn}^\rho)$ phase composition fields for the different phases, as defined in [11Moe].

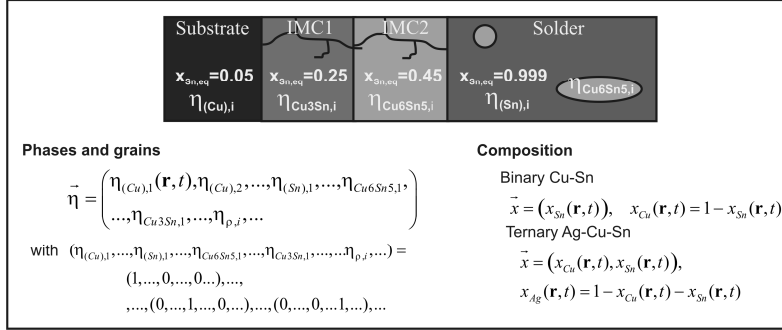


Fig. 10.1: Representation of the considered microstructure by means of phase field variables. Phases and grain orientations are represented with non-conserved order parameters $\eta_{\rho i}$ where the first index refers to the phase and the second to the grain orientation. The local composition is represented with the molar fraction fields of Cu and Sn.

The molar Gibbs energies of the different phases $G_m^\rho(\bar{x}, T^*)$ must be continuous functions of the molar fractions and defined for the complete composition domain. Such composition dependent expressions for the full composition domain are available in the SOLDERS database developed within COST 531 and COST MP0602 [08Din, 12Din] for the phases bct-(Sn), fcc-(Cu) and liquid in the Cu-Sn system. Alternatively, parabolic functions of the form

$$\frac{G_m^\rho}{V_m} = \sum_{k=1}^{C-1} \frac{A_k^\rho}{2} (x_k - x_{k,0}^\rho)^2 + C^\rho \text{ with } k=Cu, Sn \text{ and } A_k^\rho, C_k^\rho \text{ and } x_{k,0}^\rho \text{ parameters chosen}$$

so that the equilibrium compositions of the different phases at the considered temperature are obtained when applying the common tangent rule for the parabolic energy functions. The diffusion equations account for both bulk and interface or grain boundary diffusion and are of the form

$$\frac{\partial x_k}{\partial t} = \nabla \cdot \left[\left(\sum_\rho \phi_\rho M_{kk}^\rho + \sum_{\rho, \sigma, i \neq \sigma, j} M_{kk}^{int} \eta_{\rho,i}^2 \eta_{\sigma,j}^2 \right) \nabla \mu_k \right],$$

$$\text{with } M_{kk}^\rho = \frac{D_{kk}^\rho}{\partial^2 f^\rho} \text{ and } M_{kk}^{int} = 3 \left(\frac{D_{kk}^{int}}{\partial^2 f^m / \partial x_k^2} \right) \left(\frac{\delta_{gb}}{\delta_{num}} \right)$$

We refer to [11Moe] for the full description of the energy and evolution equations and for the relations between model parameters and physical phase and interface properties, such as interfacial or grain boundary energy and mobility.

For the simulations presented in sections 10.3.1-10.3.3, the interfacial energy is taken $\gamma_{int}=0.35$ J/m², the interface mobility $\mu=3\cdot 10^2$ m²s/kg and the diffuse interface width $\ell_{gb}=5\cdot 10^{-7}$ m for all interfaces. Based on the phase diagram and existing Gibbs energy expressions (SOLDERS) for $T^*=180^\circ\text{C}$, the following parameters were chosen in the parabolic free energy expressions: $A^{(\text{Cu})}=10^8$, $C^{(\text{Cu})}=0$, $x_{0,\text{Sn}}^{(\text{Cu})}=0.076$, $A^{(\text{Sn})}=10^9$, $C^{(\text{Sn})}=10^7$, $x_{0,\text{Sn}}^{(\text{Sn})}=0.979$, $A^{\text{Cu}_6\text{Sn}_5}=10^{10}$, $C^{\text{Cu}_6\text{Sn}_5}=-10^6$, $x_{0,\text{Sn}}^{\text{Cu}_6\text{Sn}_5}=0.455$. The diffusion coefficients are assumed to be independent of composition.

Simulation results and discussion

10.1.1 Growth of IMC layers

The effect of different values of the diffusion coefficients in the different phases on the growth of the IMC phases Cu_3Sn and Cu_6Sn_5 was studied by 1-dimensional phase-field simulations and considering a single grain orientation for each phase. A typical evolution of the molar fraction of Sn throughout the solder joint in time is shown in [Fig. 10.2](#)~~Figure 10.2~~. By evaluating the thickness h of the Cu_3Sn and Cu_6Sn_5 layers at different time steps, the growth coefficient k in the parabolic growth law $h=kt^{0.5}$ for steady-state IMC growth was determined for different sets of diffusion coefficients and it was found that its value is mainly determined by the diffusion coefficients of the IMC phases. The simulations with $D_{\text{Cu}_3\text{Sn}}=D_{\text{Cu}_6\text{Sn}_5}=10^{-15}$ give growth constants which are close to the experimentally measured growth constants at 180°C presented in chapter 2. For a more accurate description, however, other effects, such as grain boundary diffusion and composition dependence of the diffusion coefficient, must be considered.

10.1.2 Effect of grain boundary diffusion

Three-dimensional phase-field simulations considering both bulk and grain boundary diffusion through the IMC layers were performed. For the grain boundary diffusion coefficient and grain size considered in the simulation presented in [Fig. 10.3](#)~~Figure 10.3~~, grain boundary diffusion greatly affects the growth rate of the IMC layers. Since the effect of grain boundary diffusion is grain size dependent, it is important for further experiments to measure both the parabolic growth constant and the average grain size of the IMC layers in order to obtain more accurate information on bulk and grain boundary diffusion coefficients at temperatures below 180°C .

10.1.3 Growth and coarsening of Cu_6Sn_5 precipitates

Simulations were also performed for a Cu-substrate/Sn-0.02 at.%Cu-solder joint with Cu_6Sn_5 precipitates in the solder annealed at 180°C . The overall initial composition of the solder (including the Cu_6Sn_5 precipitates) is close to the eutectic solidification composition. Several simulation experiments were performed considering various values for the diffusion coefficients in the three phases.

Formatted: Font: Not Bold

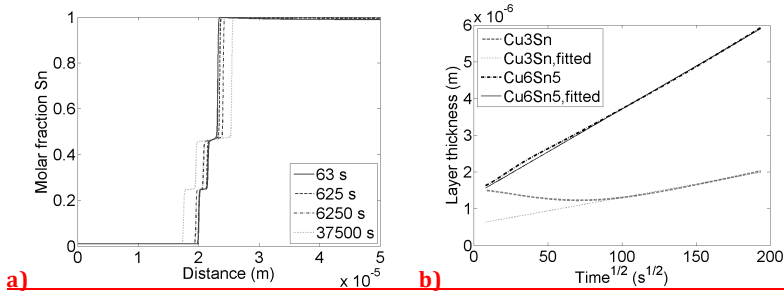


Fig. 10.2: (a) Molar fraction of Sn throughout the different phases (from left to right: (Cu)-fcc, Cu₃Sn, Cu₆Sn₅, (Sn)-bcc) of a solder joint at different time steps for T=180°C and $D_{Cu3Sn}=D_{Cu6Sn5}=10^{-15}$, $D_{(Sn)}=10^{-12}$, $D_{(Cu)}=10^{-25}$. (b) Width of the different phases as a function of the square root of time. A linear fit for Cu₆Sn₅ and Cu₃Sn gives slopes $k_{Cu6Sn5}=0.0073 \cdot 10^{-6}$ and $k_{Cu3Sn}=0.0023 \cdot 10^{-6}$.

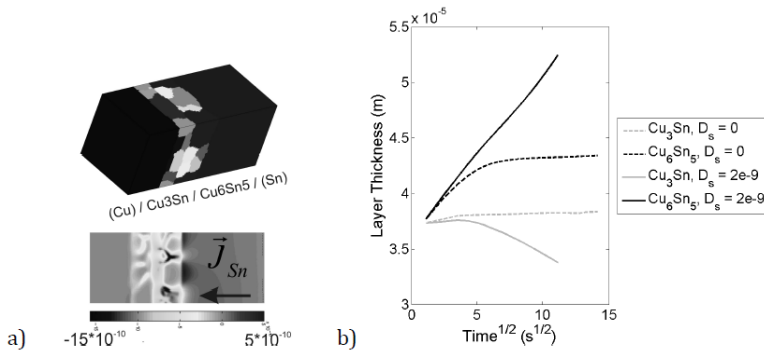
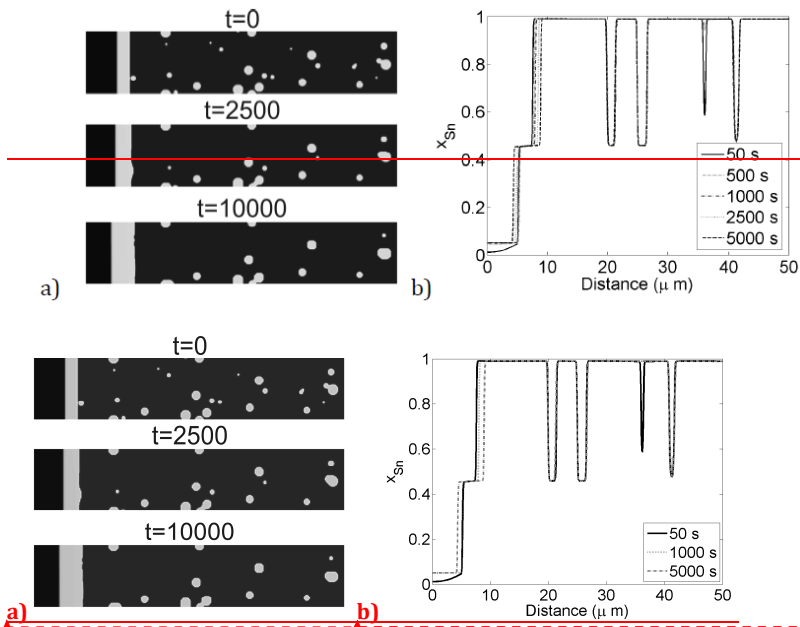


Fig. 10.3: Results of a 3-dimensional simulation of IMC growth considering grain boundary diffusion for T=180°C, $D_{Cu3Sn}=D_{Cu6Sn5}=10^{-15}$, $D_{(Sn)}=10^{-12}$, $D_{(Cu)}=10^{-25}$, $D_{surf}=10^{-9}$. (a) Considered grain structure and atomic flux of Sn (positive from right to left). (b) Comparison of the layer thickness as a function of the square root of time with and without grain boundary diffusion.

The initial compositions of the Cu₆Sn₅-phase and the (Sn)-phase are taken close to their equilibrium compositions, namely $x_{Sn} = 0.999$ and $x_{Sn} = 0.455$ respectively. The initial fraction of precipitates in a solder with composition $x_{Sn} = 0,98$ is accordingly 0.04. The initial composition of the (Cu)-phase varied between $x_{Sn} = 0.001$ (almost pure Cu substrate) and $x_{Sn} = 0.05$ (near the equilibrium composition of (Cu)) for different simulations. The presence of a Cu₃Sn layer is ignored in these simulations.

The simulation images in [Fig. 10.4](#) show how the intermetallic Cu₆Sn₅-layer grows, consuming the (Cu) and (Sn) phases, by diffusion through the

intermetallic layer. At the same time the intermetallic Cu_6Sn_5 -precipitates undergo Ostwald ripening by Cu diffusion through the Sn-matrix. The volume fraction of the precipitates decreases in time as part of the Cu-atoms dissolved in the Sn-matrix re-precipitate on the intermetallic layer (and not on a precipitate).



Formatted: Font: Cambria, Not Italic

Formatted: Font: Cambria, Not Italic

Fig. 10.4: Results of a 2-dimensional simulation of the growth and coarsening of Cu_6Sn_5 due to interdiffusion between substrate and solder for $D_{(\text{Cu})} = D_{\text{Cu}_6\text{Sn}_5} = D_{(\text{Sn})} = 0.5 \cdot 10^{-16} \text{ m}^2/\text{s}$ and initial compositions $x_{\text{Sn}} = 0.999$, $x_{\text{Sn}} = 0.455$, $x_{\text{Sn}} = 0.05$ in the solder, IMC and substrate. a) Microstructure at different time steps (blue = (Cu)-substrate, green = Cu_6Sn_5 -IMC, red = (Sn)-solder. b) Molar fraction of Sn along a horizontal line through the solder joint at different time steps.

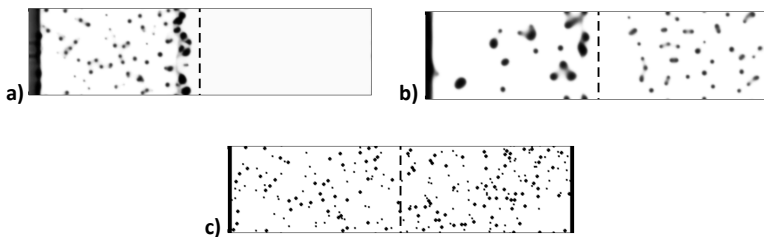


Fig. 10.5: Images of Kirkendall voiding simulations for 2-phase A-B-Va systems with α -phase on the left and β -phase on the right. The initial and final interface

are indicated with respectively a dotted and full black line. a) $D_A^\alpha = D_B^\alpha = D_A^\beta = D_B^\beta = 1e-12 \text{ m}^2/\text{s}$; $x_{Va,eq}^\alpha = 0.001$, $x_{A,eq}^\alpha = 0.999*0.5$, $x_{B,eq}^\alpha = 0.999*0.5$, $x_{Va,eq}^\beta = 0.02$, $x_{A,eq}^\beta = 0.98*0.1$, $x_{B,eq}^\beta = 0.98*0.9$; $x_{Va,0}^\alpha = 0.002$, $x_{A,0}^\alpha = 0.998*0.5$, $x_{B,0}^\alpha = 0.998*0.5$, $x_{Va,0}^\beta = 0.002$, $x_{A,0}^\beta = 0.998*0.02$, $x_{B,0}^\beta = 0.998*0.98$; b) $D_A^\alpha = D_B^\alpha = D_A^\beta = 10D_B^\beta = 1e-12 \text{ m}^2/\text{s}$; $x_{Va,eq}^\alpha = 0.001$, $x_{A,eq}^\alpha = 0.999*0.5$, $x_{B,eq}^\alpha = 0.999*0.5$, $x_{Va,eq}^\beta = 0.001$, $x_{A,eq}^\beta = 0.999*0.1$, $x_{B,eq}^\beta = 0.999*0.9$; $x_{Va,0}^\alpha = 0.002$, $x_{A,0}^\alpha = 0.998*0.45$, $x_{B,0}^\alpha = 0.998*0.55$, $x_{Va,0}^\beta = 0.002$, $x_{A,0}^\beta = 0.998*0.1$, $x_{B,0}^\beta = 0.998*0.9$; c) Initial structure. The initial fraction of voids is 0.05 in both cases (which is taken exceptionally high to make the effects obvious). A void phase is added on either side of the couple.

10.1.4 Vacancy diffusion and void formation

Finally, a basic phase-field model for vacancy diffusion and void formation in solder joints was derived starting from the model given in section 10.2, in which the 'vacancies' are considered as an extra component and the 'void'-phase as an extra phase. The equilibrium vacancy concentration of the 'void'-phase is taken close to 1, i.e. $x_{k,eq} = 0.0001$ with k all components excluding the vacancies; that of the regular phases is given a small value which can be different in the different phases. A parabolic composition dependence of the bulk energy is assumed with respect to the vacancies and all components. Diffusion equations are solved for the C components taking the vacancies as the reference component. This model allows for a systematic study of Kirkendall voiding as a function of the diffusion coefficients and solubilities of the different elements and vacancies in the different phases. Depending on the initial conditions and phase properties, voids may form at the interface or at a certain distance from the interface or randomly on one or both sides of an interface between 2 materials as illustrated in [Fig. 10.5](#) **Figure 10.5**.

Conclusions

It was shown in this paper, that the phase-field methodology allows us to study many aspects of IMC -layer and precipitate growth important during formation and further annealing or use of a solder joint. For all studies presented here, a parabolic composition dependence was assumed for the Gibbs energy and the parameters were chosen so that the phase-equilibria calculated with the SOLDERS database [08Din] are recovered in the phase field simulations. The fitting of the parabolic functions is straightforward for binary systems, however becomes prohibitively complex for ternary and higher order systems. Moreover, the compositions measured in solder joints may deviate strongly from the equilibrium phase compositions from the phase diagram. Under such conditions, the parabolic approximation of the Gibbs energy is most often no longer valid. Therefore, it would be a more general and correct approach to introduce Gibbs energy models in the thermodynamic databases which are formulated over the complete composition domain for all phases. Such Gibbs energy descriptions are also required in other diffusion models, as for example the models used in the DICTRA simulation software. Furthermore, optimized Gibbs energies as a function of the vacancy concentration as well would allow us to apply the phase-field model for vacancy diffusion and void formation for specific alloy systems.

References

- [08Din] Dinsdale, A., Watson, A., Kroupa, A., Vrestal, J., Zemanova, A., Vizdal, J.: Version 3.0 of the SOLDERS Database for Lead Free Solders, 2008
<http://resource.npl.co.uk/mtdata/soldersdatabase.htm>
- [08Moe] Moelans, N., Blanpain, B., Wollants, P.: CALPHAD -- Computer Coupling of Phase Diagrams and Thermochemistry, 2008, **32**, 268-294.
- [08Moe2] Moelans, N.: Arch. Metall. Mater., 2008, **53** (4), 1149-1156.
- [11Moe] Moelans, N.: Acta Mater, 2011, **59**, 1077-1086.
- [12Din] Dinsdale, A., Kroupa, A., Watson, A., Vrestal, J., Zemanova, A., Vizdal, J.: MP0602 Database for High-Temperature Lead Free Solders, 2008

11 Effect of elastic stresses on the growth of IMC precipitates – phase – field method coupled with micro-elasticity theory

A. Durga, and N. Moelans

KU Leuven, Department of Metallurgy and Materials Engineering, Belgium

Introduction

An important issue within the context of lead-free soldering is that, during the ageing process, internally generated elastic stresses (due to mismatch of lattice parameters between different phases) can influence the coarsening of the grain structure. The mechanical properties of the solder joint in turn are affected by the grain morphology. The reliability of the solder joint during service is determined by its mechanical response to externally applied loads and internal stresses.

The phase-field method combined with micro-elasticity theory can be used to simulate the stress evolution in such a system, giving more insights into the conditions which affect the reliability. Currently, elasticity can be included in several ways using different interpolation schemes to define the elastic properties within the diffuse interface. To develop a scheme which is consistent with the ‘thin-interface’ description (see Section 10.1) so that there is no additional contribution to the interfacial energy from the elastic energy is an active area of research.

In the present study, two available interpolation schemes for elasticity are applied to study the change in equilibrium composition of an IMC layer-solder interface in the presence of internal stresses and IMC-precipitate evolution in a Cu-Sn lead-free solder.

Phase-field model coupled with elasticity

In the present study, only binary (Cu-Sn) two-phase (Cu_3Sn — Bct_{Sn} or Cu_6Sn_5 — Bct_{Sn}) systems are considered. The total free energy functional of the phase-field model is given by:

$$F(\phi, x_{\text{Sn}}) = \int_V \{f_{\text{int}}(\phi) + f_{\text{bulk}}(\phi, x_{\text{Sn}})\} dV \quad (1)$$

where x_{Sn} is the molar fraction of Sn, ϕ is the phase-field variable, representing the phase fraction of IMC-phase and f_{int} and f_{bulk} are interfacial and bulk energy densities respectively. The microstructure is usually represented by the value of the phase-field variable ϕ .

The interfacial energy density is given by:

$$f_{\text{int}}(\phi) = \frac{\kappa}{2} (\nabla \phi)^2 + Wg(\phi) \quad (2)$$

Comment [A55]: Maybe not all the equations in this whole contribution are necessary. But this is really just a comment

where κ is the gradient energy coefficient, $g(\phi) = \phi^2(1 - \phi^2)$ the double-well function and W the depth of the double-well function.

When elasticity is included, the bulk energy density becomes:

$$f_{bulk} = f_{chem} + f_{el} \quad (3)$$

where f_{chem} is the contribution from chemical Gibbs energy and f_{el} is the elastic energy density. f_{chem} is formulated as [99Kim]:

$$f_{chem} = p(\phi) \frac{G_m^{IMC}}{V_m} + [1 - p(\phi)] \frac{G_m^{Bct}}{V_m} \quad (4)$$

where V_m is the molar volume, G_m^{IMC} and G_m^{Bct} are the molar Gibbs energies of IMC and Bct phases respectively, interpolated using a smooth interpolation function $p(\phi) = \phi^3(6\phi^2 - 15\phi + 10)$.

The temporal evolution of the molar fraction of Sn is given by:

$$\frac{\partial x_{Sn}}{\partial t} = \bar{\nabla} \cdot M \bar{\nabla} \frac{\delta F}{\delta x_{Sn}} = \bar{\nabla} \cdot M \bar{\nabla} \frac{\partial f_{chem}}{\partial x_{Sn}} \quad (5)$$

where M is the chemical mobility.

Only small strains are considered in the system. Therefore, Hooke's law is valid and the elastic energy density can be written as:

$$f_{el} = \frac{1}{2} \varepsilon_{ij} C_{ijkl} \varepsilon_{kl} \quad (6)$$

where ε_{kl} is the elastic strain and C_{ijkl} the stiffness tensor. The elastic strain (ε_{kl}) is the sum of the externally applied strains ($\bar{\varepsilon}_{kl}$), the local heterogeneous strain ($\delta\varepsilon_{kl}$) generated due to local displacements and negative eigenstrain (ε_{kl}^*) [83Kha].

$$\varepsilon_{kl} = \bar{\varepsilon}_{kl} + \delta\varepsilon_{kl} - \varepsilon_{kl}^* \quad (7)$$

By assuming that the system is always at-in mechanical equilibrium at every time step,

$$\text{i.e., } \frac{\partial \sigma_{ij}}{\partial r_j} = 0 \quad (8),$$

the elastic strain is solved using the framework developed by Hu and Chen [01Hu].

Two interpolation schemes, namely, Khachaturyan's [83Kha] and Steinbach-Apel's [06Ste] are ~~taken up~~ accepted for further study. In both the schemes, the eigenstrain at-in the interface is interpolated between the eigenstrains of the phases using $p(\phi)$.

Formatted: Space Before: 0,5 line

Comment [A56]: Do you really mean inside the interface thickness?

$$\boldsymbol{\varepsilon}_{kl}^* = p(\phi)\boldsymbol{\varepsilon}_{kl}^{*,IMC} + [1 - p(\phi)]\boldsymbol{\varepsilon}_{kl}^{*,Bct} \quad (9)$$

In the Khachaturyan's scheme, the stiffness tensor is ~~interpolated~~ obtained by interpolation between the stiffness tensors of the phases present.

$$C_{ijkl} = p(\phi)C_{ijkl}^{IMC} + [1 - p(\phi)]C_{ijkl}^{Bct} \quad (10)$$

In the Steinbach-Apel's scheme, the Reuss-Sachs condition of equal stress is used and hence, the compliance tensor is ~~interpolated~~ obtained by interpolation between the compliance tensors of the phases.

$$S_{ijkl} = p(\phi)S_{ijkl}^{IMC} + [1 - p(\phi)]S_{ijkl}^{Bct} \quad (11)$$

The temporal evolution of the phase-field variable is given by:

$$\frac{\partial \phi}{\partial t} = -L \frac{\delta F}{\delta \phi} = -L \left(\frac{\partial f_{chem}}{\partial \phi} + \frac{\partial f_{el}}{\partial \phi} + \frac{\partial f_{int}}{\partial \phi} \right) \quad (12)$$

The derivative of the elastic energy with respect to the phase-field variable is different for the two schemes. Using the Khachaturyan's scheme, we obtain

$$\frac{\partial f^{el}}{\partial \phi} = \frac{1}{2} \varepsilon_{ij} p'(\phi) (C_{ijkl}^{IMC} - C_{ijkl}^{Bct}) \varepsilon_{kl} - p'(\phi) (\varepsilon_{ij}^{*,IMC} - \varepsilon_{ij}^{*,Bct}) C_{ijkl} \varepsilon_{kl} \quad (13)$$

Using Steinbach-Apel's scheme, we obtain

$$\frac{\partial f^{el}}{\partial \phi} = -p'(\phi) \varepsilon_{ij} C_{ijkl} (\varepsilon_{kl}^{*,IMC} - \varepsilon_{kl}^{*,Bct}) - \frac{1}{2} p'(\phi) \varepsilon_{ij} C_{ijmn} (S_{mnop}^{IMC} - S_{mnop}^{Bct}) C_{opkl} \varepsilon_{kl} \quad (14)$$

From these formulations, it is not apparent which scheme would give more realistic results when implemented in the phase-field model. Further analysis needs to be performed in order to compute the interfacial energy contribution.

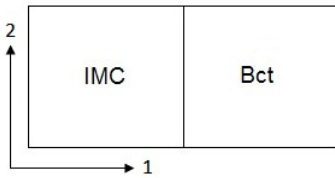


Fig. 11.1.1: Configuration of the 2-phase simulation domain: $12.8 \mu\text{m} \times 0.4 \mu\text{m}$.

Comment [A57]: I hope that this text really belongs to the caption of Fig. 1

Parabolic chemical molar Gibbs energy densities of the form $\frac{G_m^\rho}{V_m} = \frac{A^\rho}{2} (x_{Sn} - x_{Sn,0}^\rho)^2$ are assumed, where $\rho = \text{IMC, Bct}$. The constants are taken

as $A^{Cu_6Sn_5} = A^{Bct} = 10^{11} \text{ J/m}^3$, $x_{Sn,0}^{Cu_6Sn_5} = 0.455$ and $x_{Sn,0}^{Bct} = 0.999$. The chemical mobility M is assumed to be a constant $= 10^{-21} \text{ m}^3 \text{ s/kg}$ and equal for all components in all phases.

Simulation results and discussion

11.1.1 11.3.1—Change in chemical equilibrium

It is known that the chemical equilibrium of a system in the presence of stresses is different from the case of no stresses [84Cah]. In the following simulations, the change in equilibrium molar fraction of Sn in the presence of stresses is demonstrated for Cu₆Sn₅—Bct-Sn system. 2-D simulations are performed for the configuration shown in Figure 11.1 using the two schemes. The system is constrained such that there is no macroscopic deformation, i.e., $\bar{\epsilon}_{kl} = 0$.

The elastic constants of the two phases are taken from [09Che, 09Gho], which are computed using first-principles calculations. Unstrained Bct phase is taken as the reference state, leading to a non-zero dilatational eigenstrain tensor in the IMC phase: $\epsilon_{kl}^{*,IMC}$. Here, it is taken as -3%, based on the lattice parameters of the two phases. Using the boundary conditions and the assumption of mechanical equilibrium (Equation 8), the heterogeneous strain can be derived analytically as:

$$\delta \epsilon_{11}^{el,Bct} = \frac{-C_{1111}^{IMC} \epsilon_{11}^{*,IMC} - C_{1122}^{IMC} \epsilon_{22}^{*,IMC}}{C_{1111}^{IMC} + C_{1111}^{Bct}} \quad (15)$$

The heterogeneous strain in the vertical direction is zero since the system is constrained at the boundaries and the normal to the interface between the two phases is along direction 1. For the parabolic Gibbs energies, the new equilibrium molar fractions of Sn for the two phases are calculated analytically as [87]oh):

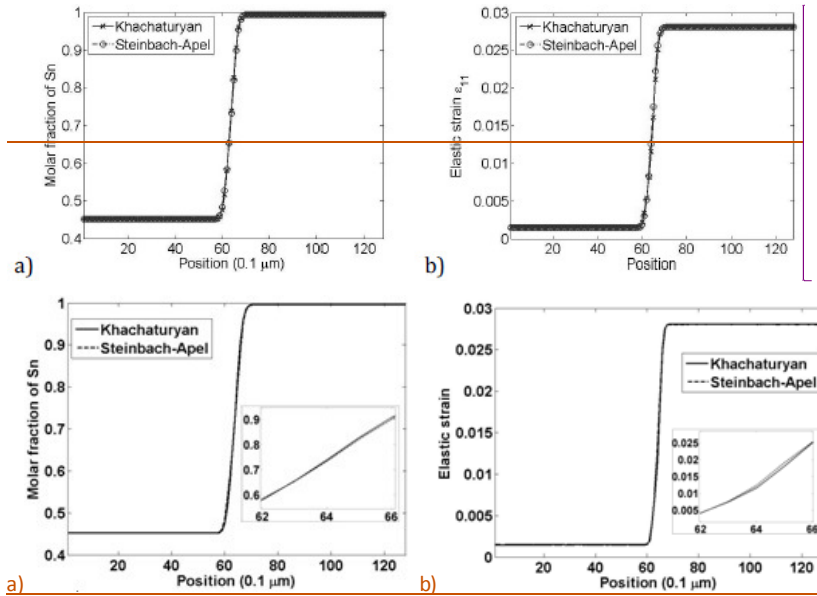
$$x_{Sn}^{\rho,e} = x_{Sn,0}^{\rho} + \frac{(\sigma_{kl}^{IMC} \epsilon_{kl}^{IMC} - \sigma_{kl}^{Bct} \delta \epsilon_{kl}^{Bct}) / 2 + (\delta \epsilon_{kl}^{Bct} - \delta \epsilon_{kl}^{IMC}) \sigma_{kl}^{Bct}}{A^{\rho} (x_{Sn,0}^{IMC} - x_{Sn,0}^{Bct})} \quad (16)$$

where $\rho = \text{IMC, Bct}$. Other parameters used in the simulation are: grid size $\Delta x = 0.1 \mu\text{m}$, time step $\Delta t = 5 \cdot 10^{-5} \text{ s}$, interface mobility $= 10^{-10} \text{ m}^2 \text{ s/kg}$, $W = 2.5 \cdot 10^5 \text{ J/m}^3$ and $\kappa = 2 \cdot 10^{-5} \text{ J/m}$. Simulations for the two schemes were performed for $6 \cdot 10^5$ time steps $= 30 \text{ sec}$. Figure 11.2(a) shows the molar fraction profiles at equilibrium obtained for the two schemes. The new bulk equilibrium compositions in the Cu₆Sn₅ and Bct phases as calculated using (16) are 0.4518 and 0.9958 respectively. This is reproduced correctly in the simulations. This shows that externally applied loads can affect the local chemical equilibrium significantly. Further analysis on this effect for different morphologies and sizes using Gibbs energies from the CALPHAD description can provide more accurate information. The elastic strains present in the two phases calculated using (15) are 0.0016 and 0.028 respectively. The simulation results match with these values for both the schemes. The variation of elastic strain component ϵ_{11} across the system is shown in Figure 11.2(b). For the values of elastic properties used in this simulation for this morphology, the choice of elastic scheme does not make a

Comment [A58]: I do not fully understand this. I thought that you developed the Eq. (16) for the use in the simulation? You claim that they are reproduced well by the simulation – but I thought that you only obtain this value by the simulation. (I do not know if I explain my confusion well).-> we tried to solve the confusion by adding the “analytically” in the previous sentences

Comment [A59]: The same as in previous comment

difference as far as the equilibrium values of bulk properties of this system are considered. However, for other morphologies and combinations of elastic properties, both schemes can give very different results as will be shown in Section 11.3.2.



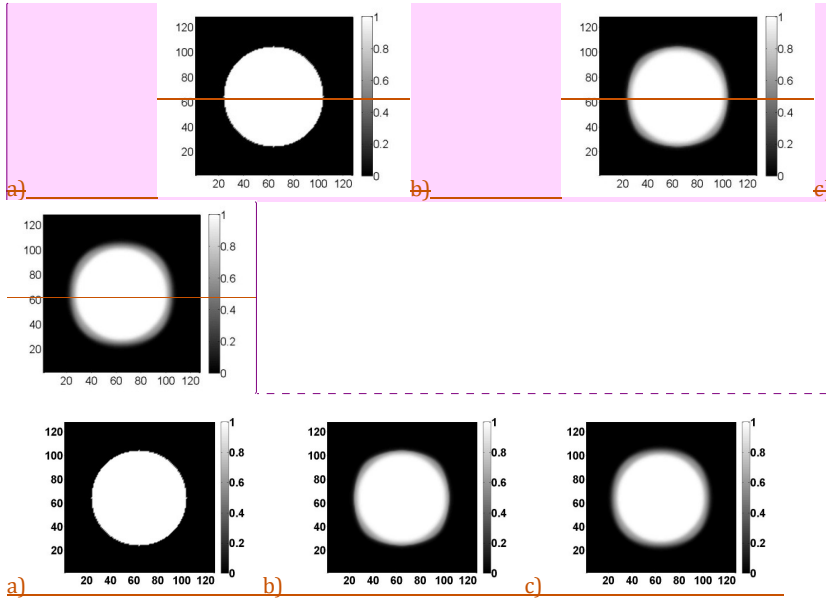
Comment [A60]: Here the points are difficult to distinguished. Is it possible to edit it a bit to make it more readable in B&W.

Fig. 11.2: Results of a 2-dimensional simulation of Cu_6Sn_5 -Bct system (configuration shown in Figure 11.1) with an inlay of a zoomed-in view of the interface. (a) Comparison of variation of molar fraction of Sn across the system for the two elastic schemes. (b) Comparison of variation of elastic strain component ϵ_{11} across the system for the two elastic schemes.

11.1.2 ~~11.3.2~~—IMC-precipitate evolution

Simulations were performed for the evolution of circular Cu_3Sn and Cu_6Sn_5 precipitates (radius $4 \mu\text{m}$) respectively in Bct-Sn solder matrix ($12.8 \mu\text{m} \times 12.8 \mu\text{m}$). The input parameters mentioned in Section 11.3.1 are used for these simulations also, excepting except of the following: $\Delta t = 2 \cdot 10^{-5} \text{ s}$, $W = 5 \cdot 10^6 \text{ J/m}^3$ and $\kappa = 10^{-6} \text{ J/m}$. For Cu_3Sn , $\chi_{\text{Sn},0}^{\text{Cu}_3\text{Sn}} = 0.25$, $A_{\text{Cu}_3\text{Sn}} = 10^{11}$, eigenstrain is taken as -2% and stiffness from [08An]. The initial configuration of the simulation domain is shown in Figure 11.3(a). Figures 11.3(b) and (c) show the ϕ field obtained for Cu_3Sn precipitate for the two schemes after $1.5 \cdot 10^6$ time steps or 30 s. As demonstrated in the previous section, the composition inside the bulk of the precipitate and the solder phases change and are 0.2493 and 0.9983 respectively at the end of the simulation for this morphology. Similar simulations were performed for Cu_6Sn_5 .

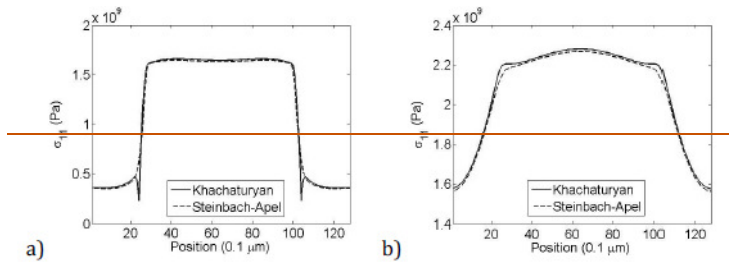
Comment [A61]: Do you mean inside the IMC precipitate?



Comment [A62]: Here the axis description should be slightly bigger for better reading

Fig. 11.3: Results of simulation of Cu_3Sn precipitate in Bct-Sn matrix. (a) Initial configuration (grid size = $0.1 \mu\text{m}$). (b) ϕ field obtained for Khachaturyan's scheme after 30 s. (c) ϵ - ϕ field obtained for Steinbach-Apel's scheme after 30 s.

The variation of elastic stress component σ_{11} in the system is shown for Cu_3Sn and Cu_6Sn_5 precipitates in Figure 11.4. For these simulations, a clear difference is observed between the two elastic schemes. Hence, it is important to identify the scheme which would give accurate results when used in the framework of phase-field modelling. Moreover, the stresses obtained from the simulations are of the order of GPa, which are very high compared to the yield stress of Cu-Sn lead-free solder, which is of the order of MPa [11ELD]. Therefore, it is important to consider plastic effects also in order to perform realistic simulations.



Comment [A63]: Again the legend should be a bit bigger.

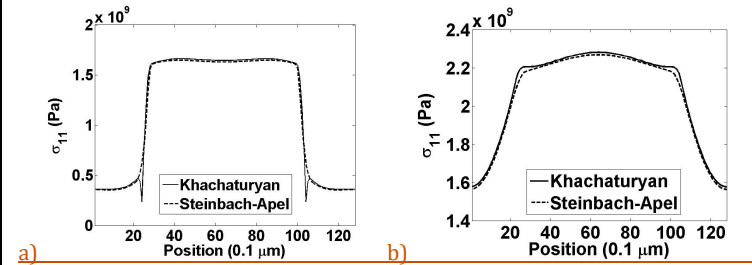


Fig. 11.4: Results of simulation of IMC-precipitate in Bct-Sn matrix. (a) Elastic stress component σ_{11} profile along a vertical line through the centre for Cu_3Sn precipitate after 30 s. (b) Elastic stress component σ_{11} profile along a horizontal line through the centre for Cu_6Sn_5 precipitate after 20 s.

Conclusions

In the present study, the importance of considering elastic effects in phase-field simulations of IMC evolution in lead-free solder joints is illustrated. The presence of stresses in the system, apart from causing morphological changes, can significantly change the equilibrium chemical compositions of the phases present. This was demonstrated by simulating a Cu_6Sn_5 -Bct system, considering the eigenstrain due to the mismatch of lattice parameters between the two phases. Simulations of Cu_3Sn and Cu_6Sn_5 precipitate evolution in Bct-Sn solder matrix were also performed. The results were shown to depend on the schemes used to interpolate the elastic properties. Considering only elasticity, the stresses developed in the system were shown to be unnaturally high. Therefore, for further studies, it is important to use a phase-field model considering plasticity, a consistent interpolation scheme for elasticity and Gibbs energy functions developed using the CALPHAD method to obtain more realistic results.

References

- [99Kim] Kim, S. G., Kim, W. T., Suzuki, T.: Phys. Rev. E, 1999, **60** (6), 7186-97.
- [83Kha] Khachaturyan, A. G.: „Theory of structural transformations in solids“, Wiley, New York, 1983.
- [01Hu] Hu, S. Y., Chen, L. Q.: Acta mater., 2001, **49**, 1879-1890.
- [06Ste] Steinbach, I., Apel, M.: Physica D, 2006, **217**, 153-160.
- [84Cah] Cahn, J. W., Larché, F.: Acta metall., 1984, **32** (11), 1915-23.
- [09Che] Chen, J., Lai, Y. S.: Microelectronics Reliability, 2009, **49**, 264–268.
- [09Gho] Ghosh, G.: Met. Mat. Trans. A, 2009, **40A**, 4–23.
- [87Joh] Johnson, W. C.: Met. Trans. A, 1987, **18A**, 233-47.
- [08An] An, R., Wang, C., Tian, Y., Wu, H.: J Electron. Mater., 2008, **37** (4), 477-82.
- [11ED] El-Daly, A. A., Hammad, A. E.: J Alloys Compd., 2011, **509**, 8554-60.

Formatted: Dutch (Belgium)

12 Phase - field simulations of IMC growth in Ag-Cu-Sn/Cu joints with full description of the composition dependence of the Gibbs energies and diffusion mobilities

Y. Guan, Durga. A. and N. Moelans

KU Leuven, Department of Metallurgy and Materials Engineering, Belgium.

Introduction

In this work, the evolution of the IMCs at the interface between a Cu substrate and Sn-Ag-Cu (SAC) solder alloys was studied by means of computer simulations based on the phase-field method. The complete evolution of the IMCs is described by the simulations. The model was applied to study the influence of the atomic mobilities on the diffusion behavior of the different elements in the different phases. Furthermore, the effect of system configuration was studied by means of a 2D simulation of the growth of Cu_6Sn_5 at the interface between a circular Fcc-Cu particle and a Bct-Sn matrix.

Model implementation and validation

In this work, the phase-field model and the full description of the energy and evolution equations [11Moe], as presented and described in Chapter 10.2, is used, but with a full thermodynamic description of the Gibbs energy expressions for a multicomponent system obtained from thermodynamic databases using the CALPHAD method. A schematic overview of the relation between the phase-field method and the CALPHAD method is shown in Figure 12.1. The diffusion equation and order parameter evolution equation are implemented using the phase-field method with the diffusion data from literature [11Pau]. The Gibbs energy expressions are obtained from the SOLDERS thermodynamic database [08Din]. The interdiffusion potential used in the diffusion equation is related to the first derivative of the Gibbs energy with respect to the molar fraction of component i . The interdiffusion mobilities together with the second derivative of the Gibbs energy with respect to the molar fraction of component i and j used in the diffusion equation are related to the interdiffusion

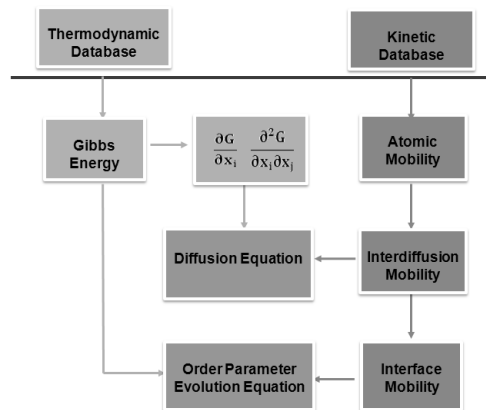


Fig. 12.1: Schematic overview of the relation between the phase-field method and the CALPHAD method.

coefficients obtained from experimental data. The interface mobility used in the order parameter evolution equation is calculated from the interdiffusion mobilities to obtain diffusion controlled growth.

In the current model, a ternary system (Sn-Ag-Cu system) with two independent components and the phases Fcc, Cu₃Sn, Cu₆Sn₅ and Bct is focused on. The thermodynamic expressions for Fcc and Bct phases are obtained directly from the SOLDERS database. For the Cu₃Sn and Cu₆Sn₅ phase, a sublattice model [07Luk] with two sublattices is used. The notation of the model is (Ag, Cu, Sn)_{a1}(Ag, Cu, Sn)_{a2} with a₁ equal to 0.75 and a₂ equal to 0.25 for Cu₃Sn, and a₁ equal to 0.545 and a₂ equal to 0.455 for Cu₆Sn₅. The formation energy of the end-members for Cu₃Sn and Cu₆Sn₅ phase are listed Table 12.1, with all the other parameters which are not listed taken as 0.

Table 12.1: Thermodynamic parameters of Cu₃Sn and Cu₆Sn₅ phase in the Sn-Ag-Cu ternary system.

Phases	Thermodynamic parameters ¹ (298.15-3000K)
Cu ₃ Sn	Model (Ag, Cu, Sn) _{0.75} (Ag, Cu, Sn) _{0.25} $G_{Ag:Ag}^0 = \text{GHSERAG} + 5000$ $G_{Cu:Cu}^0 = \text{GHSERCU} + 20000$ $G_{Sn:Sn}^0 = \text{GHSERSN} + 35000$ $G_{Cu:Sn}^0 = 0.75 \cdot \text{GHSERCU} + 0.25 \cdot \text{GHSERSN} + 8194.2 - 0.2043T$ $G_{Sn:Cu}^0 = 0.75 \cdot \text{GHSERSN} + 0.25 \cdot \text{GHSERCU} + 61694.2 + 0.2043T$
Cu ₆ Sn ₅	Model (Ag, Cu, Sn) _{0.545} (Ag, Cu, Sn) _{0.455} $G_{Ag:Ag}^0 = \text{GHSERAG} + 5000$ $G_{Cu:Cu}^0 = \text{GHSERCU} + 8500$ $G_{Sn:Sn}^0 = \text{GHSERSN} + 20000$ $G_{Cu:Sn}^0 = 0.545 \cdot \text{GHSERCU} + 0.455 \cdot \text{GHSERSN} - 7129.7 + 0.4059T$ $G_{Sn:Cu}^0 = 0.545 \cdot \text{GHSERSN} + 0.455 \cdot \text{GHSERCU} - 35629.7 - 0.4059T$

The diffusion equations for the Sn-Ag-Cu ternary system are

$$\frac{\partial x_B}{\partial t} = -\nabla \cdot J_B = \nabla [M_{BB} \nabla \tilde{\mu}_B + M_{BC} \nabla \tilde{\mu}_C] \quad (1)$$

$$\frac{\partial x_C}{\partial t} = -\nabla \cdot J_C = \nabla [M_{BC} \nabla \tilde{\mu}_B + M_{CC} \nabla \tilde{\mu}_C] \quad (2)$$

with $\tilde{\mu}_B = \mu_B - \mu_A$ the interdiffusion potential of B and μ_B and μ_A are the chemical potentials of B (the dependent component) and A, respectively. Similarly, $\tilde{\mu}_C = \mu_C - \mu_A$. For a ternary system, the interdiffusion mobilities are related to atomic mobilities M_s^0 as [92And]

$$M_{BB}^0 = x_B(1 - x_B)M_\rho \quad (3)$$

$$M_{BC}^0 = -x_B x_C M_\rho \quad (4)$$

$$M_{CC}^0 = x_C(1 - x_C)M_\rho$$

¹ The molar Gibbs free energy of constituent Ag, Cu and Sn in their SER state are taken from SOLDERS database

(5)

The M_p are the atomic mobilities of the elements in the different phases and they are independent of composition. To simplify the parameters here, it is assumed that all elements have the same atomic mobility in a certain phase. The interdiffusion mobilities M_{AA} , M_{BB} and M_{AB} , however, are composition dependent through relations (3) to (5). The atomic mobilities for the different phases are specified in the input file and the interdiffusion mobilities are calculated as a function of the local concentrations by the phase-field program at every time step and position.

It is validated for different combinations of phases that the phase-field model evolves towards the correct phase equilibria as compared to calculations according to the CALPHAD approach using the SOLDERS database at 450K.

1D simulation of the growth of IMCs in a Cu/SAC solder joint

The phases selected in the simulations at 450K are the Cu-rich face-centered-cubic (Fcc) phase to represent the Cu substrate, the phases Cu_3Sn and Cu_6Sn_5 to represent the IMCs and a Sn-rich body-centered tetragonal (Bct) phase to represent the SAC solder alloy.

The initial compositions are listed in Table 12.2. They are chosen based on two-point calculation by one point in the Fcc+ Cu_3Sn two-phase region and another point in the Cu_6Sn_5 +Bct two-phase region in the isothermal section at 450 K. In this way, so that the intermetallic phases are in equilibrium with their neighbouring end phase at the beginning of the simulation, and they will not immediately dissolve or disappear. But the intermetallic phases Cu_3Sn and Cu_6Sn_5 are thus however not in equilibrium, and also Fcc is not in equilibrium with Bct, etc. Therefore, the whole system will evolve and finally reach thermodynamic equilibrium after a long time of simulation.

Table 12.2: Initial compositions of Fcc, Cu_3Sn , Cu_6Sn_5 and Bct phase using Pandat.

	x(Cu)	x(Sn)	x(Ag)
Fcc	0.974224	0.025744	3.15442e-5
Cu_3Sn	0.749988	0.25	1.17739e-5
Cu_6Sn_5	0.54497	0.455028	1.92497e-6
Bct	5.19144e-5	0.999578	3.70319e-4

The simulation is performed for a 1D simulation domain of 15.2 μm using a grid spacing Δx with $1 \cdot 10^{-7}$ m. The interfacial free energy are taken equal to 0.05 Jm^{-2} and the interfacial width² as $l_{\text{int}} = 400$ nm for all interfaces in all simulations.

12.1.1 1D simulation for four phases with equal mobilities

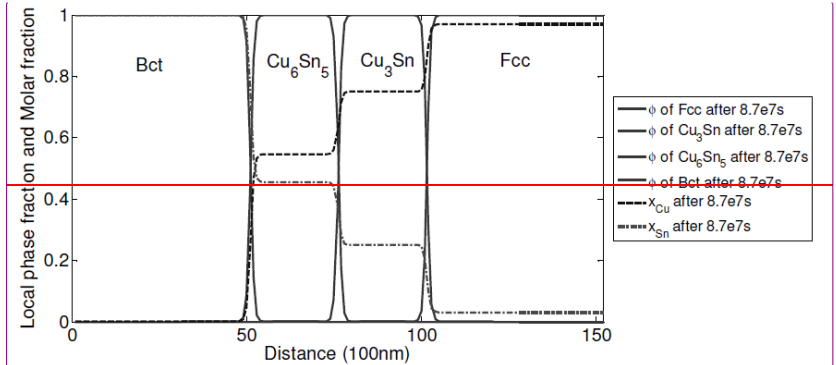
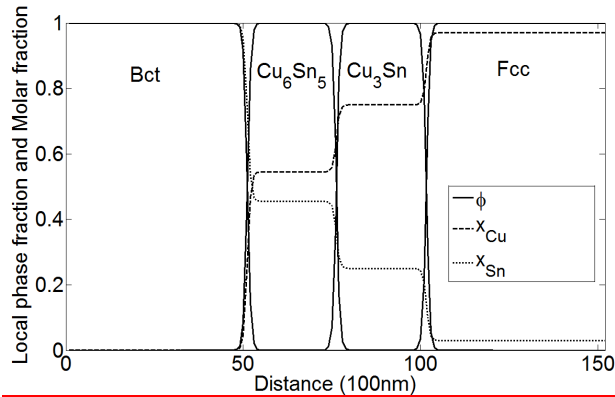
In this simulation, it is assumed that the atomic mobilities M_p are equal to $1 \cdot 10^{20} \text{ m}^3 \text{ J}^{-1} \text{ s}^{-1}$ for all elements in each phase. The calculated interface mobility is equal to $1.67 \cdot 10^{-16} \text{ m}^3 \text{ J}^{-1} \text{ s}^{-1}$.

² This is the width of the phase-field properties, it is not related to the physical width.

The simulation result is shown in Figure 12.2. It can be observed that the sharp changes of the concentration profile are in the same positions as the cross points of the ϕ - ϕ profiles (which represent the local phase fractions as introduced in section 10.2), showing that the phase boundaries follow the evolution of the concentration profile is in accordance with the evolution of the local phase fraction file, which means that the phase transitions in the simulation are diffusion controlled.

Comment [A64]: I would add here the reference to the previous charter, where this profile was introduced.

Formatted: Centered



Comment [A65]: It is very difficult to distinguish particular curves here. I would recommend to redraw this figure and differentiate more clearly particular curves.

Fig.12.2: Local phase fraction of Fcc, Cu₃Sn, Cu₆Sn₅ and Bct phase and molar fraction of Cu and Sn after $8.7 \cdot 10^{-7}$ s.

In order to see the growth of the intermetallic phases, the width of the intermetallic phases is plotted as a function of the square root of time in Figure 12.3. Initially, in the transition stage, the width of Cu₃Sn phase is increasing while Cu₆Sn₅ phase remains constant. After $5.5 \cdot 10^{-7}$ s, both phases are growing and the width evolves linearly with the square root of time, indicating parabolic growth behavior. The fitted straight line of Cu₃Sn and Cu₆Sn₅ phase are also plotted in the Figure 12.3.

Since it is assumed that the phase transitions are diffusion controlled, the relation between the thickness of the IMC phase formed at the interface and the

evolution time can then be expressed by the equation $d = (Kt)^{1/2} + d_0$, with d the thickness of the IMC layer, K the growth rate coefficient, t the aging time, d_0 the initial thickness. The growth-rate coefficients K calculated from the slope for Cu_3Sn and Cu_6Sn_5 phase are $3.249e-19$ and $1.296e-19$ cm^2/s , respectively.

12.1.2 1D simulation for four phases with non-equal mobilities

The atomic mobilities used for the four phases Fcc, Cu_3Sn , Cu_6Sn_5 and Bct are listed in the Table 12.3 and the accordingly calculated interface mobilities are listed in the Table 12.4.

The evolution of the intermetallic phase change is plotted in Figure 12.4. It can be seen that the width of Cu_3Sn phase is decreasing while the width of Cu_6Sn_5 phase is increasing. However, the simulations evolve much slower; this is mainly due to the large variation in the interdiffusion mobilities for different phases and interface mobilities for different interfaces.

Comparison with experimental data

The kinetics of the formation of Cu-Sn intermetallic compounds (IMCs) in the Sn-Ag-Cu ternary system was studied using diffusion multiple technique (DM) extended by reflow soldering experiments as indicated in Chapter 2.

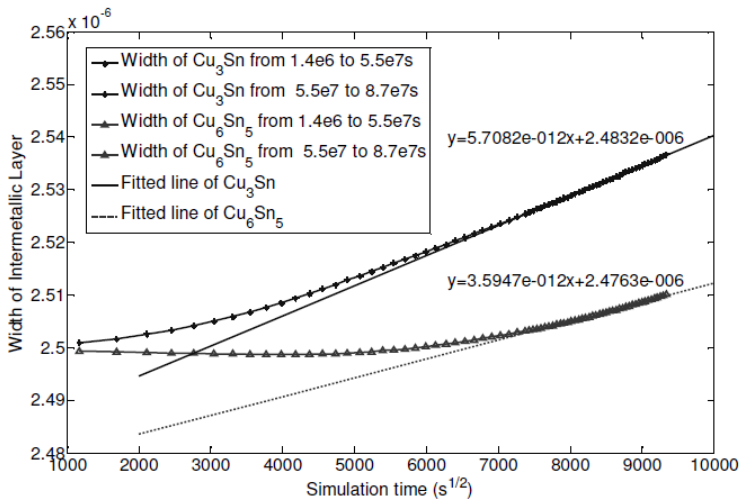


Fig. 12.3: Width of the intermetallic layer as a function of the square root of time with equal mobilities for each phase in the simulation and the fitted linear relation of the thickness of Cu_3Sn and Cu_6Sn_5 phase.

Table 12.3: The calculated value of atomic mobility for Fcc, Cu_3Sn , Cu_6Sn_5 and Bct phase

Phase	Fcc	Cu_3Sn	Cu_6Sn_5	Bct
-------	-----	----------	------------	-----

Atomic mobility ($\text{m}^2\text{mol}^{-1}\text{s}^{-1}$)	1.64e-29	5.34e-23	4.04e-21	2.84e-16
--	----------	----------	----------	----------

Table 12.4: The calculated value of interface mobility

Interface	Interface mobility ($\text{m}^3\text{J}^{-1}\text{s}^{-1}$)
Fcc/ Cu_3Sn	1.67e-19
Fcc/ Cu_6Sn_5	1.67e-18
Fcc/Bct	1.67e-13
$\text{Cu}_3\text{Sn}/\text{Cu}_6\text{Sn}_5$	1.67e-18
$\text{Cu}_3\text{Sn}/\text{Bct}$	1.67e-13
$\text{Cu}_6\text{Sn}_5/\text{Bct}$	1.67e-13

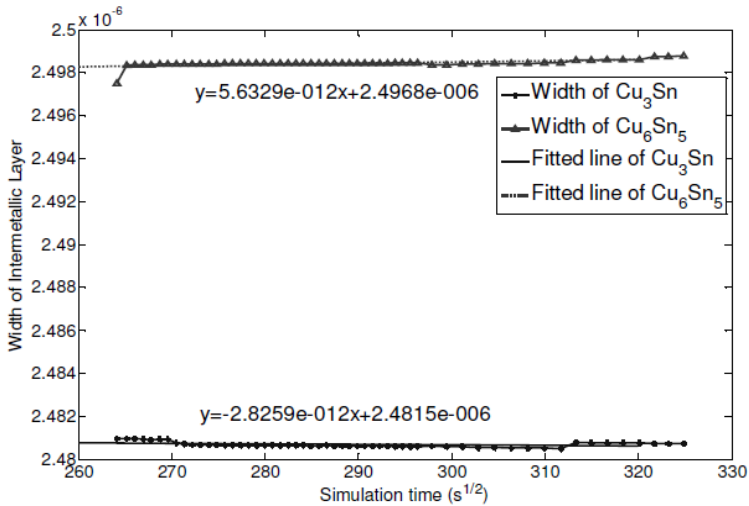


Fig. 12.4: Width of the intermetallic layer as a function of the square root of time with non-equal mobilities for each phase in the simulation and the fitted linear relation of the thickness of Cu_3Sn and Cu_6Sn_5 phase.

The growth-rate coefficients K obtained for Cu_3Sn and Cu_6Sn_5 phase at 180°C in the experiment are $4.91 \cdot 10^{-14}$ and $4.29 \cdot 10^{-13}$ cm^2/s , respectively, and they are five orders of magnitude larger than the ones calculated from the phase-field simulation. The variation may be due to the different initial compositions. Another possible factor may be the Gibbs energy expressions used for the IMC phases.

2D simulation of Cu₆Sn₅ growth at the interface between an Fcc-Cu particle and a Bct-Sn matrix

The phase-field model of microstructure evolution is applied to a 2D simulation of the growth of Cu₆Sn₅ at the interface between a circular Fcc-Cu particle and a Bct-Sn matrix. The configuration of the system is shown in Figure 12.5.

The simulation result in Figure 12.5 shows that the concentration profile is evolving simultaneously with the evolution of the order parameter profile, which means that the value used for the interdiffusion mobilities and interface mobilities in the simulation result in diffusion controlled growth.

The result also shows that the IMC Cu₆Sn₅ is enlarging into Fcc phase, indicating that the Cu particle is shrinking by transforming into Cu₆Sn₅ phase. The evolution of the IMC layer also follows a parabolic growth behaviour.

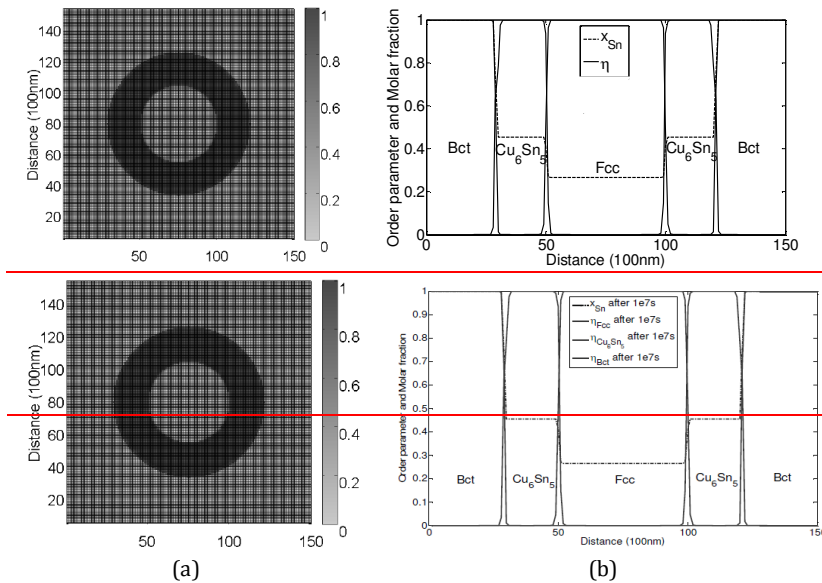


Fig. 12.5: (a) Configuration of Cu particle surrounded by Cu₆Sn₅ layer in the Sn-rich matrix by visualizing $\eta_{Cu_6Sn_5}$ after $1e-3s$ in the simulation; (b) Order parameter and molar fraction of Fcc, Cu₆Sn₅ and Bct phase after $1 \cdot 10^{-7} s$.

Conclusions

The results presented in the 1D simulations of the IMC phase in the Cu/SAC solder joint showed that the growth behavior of the IMC phases in the simulations is very sensitive to the Gibbs energy model and the values of the interdiffusion mobilities. The simulation was also reproduced for a 2D simulation of Cu₆Sn₅ growth

Comment [A66]: It is very difficult to distinguish particular curves here. I would recommend to redraw this figure and differentiate more clearly particular curves. Also the legend is a bit small for easy reading

at the interface between an Fcc_Cu particle and a Bct_Sn matrix. However, due to the limitation of computer processing ability, it would take quite a long time to see the result of several particles present in the system. The way to find an optimal distribution of the particles still needs to be further studied in the future.

References

- [08Din] Dinsdale, A., Watson, A., Kroupa, A., Vrestal, J., Zemanova, A., Vizdal, J.: Version 3.0 of the SOLDERS Database for Lead Free Solders, 2008
<http://resource.npl.co.uk/mtdata/soldersdatabase.htm>
- [11Moe] Moelans, N.: Acta Materialia, 2011, **59**, 1077-1086.
- [11Pau] Paul, A., Ghosh, C., Boettinger, W.: Metallurgical and Materials Transactions A, 2011, **42A**, 953-963.
- [07Luk] Lukas, H.L., Fries, S., Sundman, B.: "Computational thermodynamics: The CALPHAD Method" Cambridge, 2007.
- [92And] Andersson, J., Agren, J.: Journal of Applied Physics, 1992, **72**, 4.

13 Multiscale modelling of deformation and characterization of interfacial damage in lead-free solder joints

M, Maleki, J.Cugnoni, J.Botsis
LMAF-EPFL-Lausanne. The Switzerland

Introduction

The main scope of our contribution to COST MP0602 HISOLD project was developing the methodology and tools for the multi-scale modelling of the deformation and simulation of interfacial damage in lead-free solder joints for high-temperature/high-performance applications. To achieve this goal, Sn-4.0Ag-0.5Cu alloy was selected as the test material since it presents a complex microstructure as well as considerable microstructural evolution during service life. The first part of the work aimed at developing macroscopic models of the behaviour of solder joints with a special focus on the modelling of viscoplastic response in the solder and the progressive failure at the Inter Metallic Compound interface layers. The results of this part lead to better understanding of the failure mechanism and the effects of strain rate and viscoplastic deformation on the development of interfacial damage. The second part of the project focused on the development of experimental methods and micromechanical-based models for analyses of the deformation in solder joints at the microstructural level. The main scope of this part is characterization of microstructural changes and their effects on the mechanical response of lead-free solder joint.

Characterization and simulation of interfacial fracture in lead-free solder joints

13.1.1 Summary

In this part, the interfacial failure of the solder joint was characterized and modelled taking into account the viscoplastic response of bulk solder. For this purpose, the viscoplastic behavior of solder was characterized in shear and the constitutive parameters related to Anand's viscoplastic model [REF289Bro] were identified. Fracture tests were performed on soldered tapered double cantilever beam specimen (TDCB) showing that increasing strain rate significantly increases the tendency to develop an interfacial failure and reduces the maximum load capability of the joint. The damage progression and consequent crack growth at the interface of the TDCB joint were simulated in details by employing the identified Anand's parameters and identifying a cohesive zone damage model. It was shown that the main energy dissipation mechanism at the lower testing speed is the viscoplastic deformation of the bulk solder, while, when increasing the strain rate, the portion of dissipated interfacial damage energy increases significantly. The mutual effects of viscoplastic deformation and interfacial fracture were clarified.

Comment [A67]: As I am not an expert in mechanical properties, many model names are unknown to me. So maybe a bit more references would be useful throughout the chapter.

13.1.2 Shear testing and viscoplastic response of the solder joint

As premature failure of the interface tends to significantly affect the result of tensile test, shear testing was chosen for the characterization of the viscoplastic behaviour of the solder independently from the interfacial fracture mode. The single lap shear specimen design as presented in [09Siv] was utilized here. Shear tests were performed at different imposed displacement rates and a digital image correlation technique (DIC) was used to measure the strain distribution in the solder joint. The dotted line in Fig. 13.1 (a) shows the equivalent stress versus the equivalent inelastic strain curves obtained from the analyses of the shear tests at five different strain rates from 0.07 to 0.24 ($\%/s^{-1}$) at room temperature. Anand's model [89Bro] was employed to characterize the constitutive inelastic response of SAC405 solder joint based on experimental results [3]. Solid lines in Fig. 13.1 (a) show the predicted responses of the solder joints based on Anand's model.

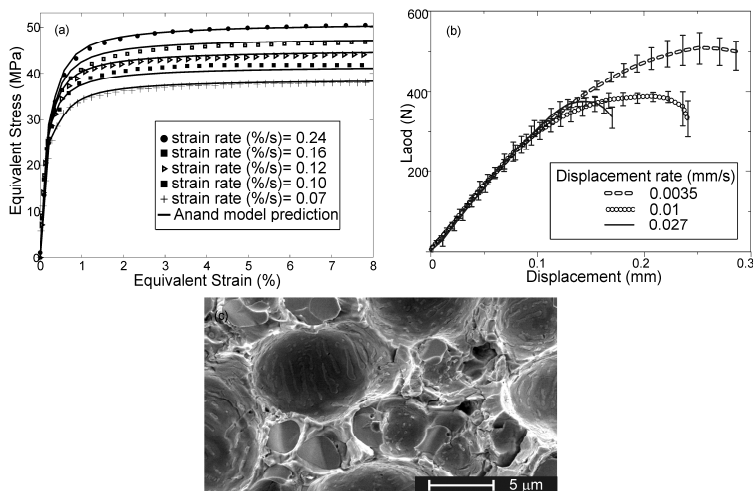


Fig. 13.1: (a) Stress-strain curve obtained from shear tests of SAC405/Cu solder joints, (b) Load-displacement responses of TDCB specimens obtained from traction tests at different displacement rates, (c) SEM micrograph of fracture surface showing mixture of facets and dimpled surface

13.1.3 Stable fracture tests at different strain rates

A tapered double cantilever beam specimen (TDCB) design [REF297Ber] was optimized and employed in the present study for characterization of interfacial fracture of SAC405 solder joints in a wide range of strain rates. Such a configuration allowed acquiring data during damage and crack progression which is valuable for identification of an interfacial damage model. The geometry of soldered TDCB specimen and details of designing procedure as well as fabrication method were reported in [11Mal]. The TDCB specimens were pulled to failure at three different

displacement rates (0.0035, 0.01 and 0.027 mm/s). Fig. 13.1 (b) shows load-displacement curves obtained from the traction tests of soldered TDCB specimens. The result indicated that the interfacial crack growth behaviour in the performed TDCB fracture tests is obviously a function of the imposed displacement rate, such that with increasing displacement rate, both crack initiation and final failure occur at lower displacements. Moreover, the data in Fig. 13.1 (b) demonstrate that by increasing the displacement rate, the maximum load capacity of the joints decreases. Results of fracture surface analyses showed that crack typically grows near the interface of IMC and bulk solder and may go inside the brittle interfacial intermetallic (Cu_6Sn_5 and Cu_3Sn) or bulk solder during its propagation in TDCB tests, so that the fracture surfaces were composed of a mixture of facets and dimple structures (Fig. 13.1 (c)).

13.1.4 Cohesive modelling of interfacial damage

A bilinear traction-separation cohesive model [REF203Cam] was employed for modelling the interfacial damage progression in the TDCB tests. According to the model, the cohesive traction linearly increases with the slope of E . Once the traction in the cohesive zone reaches the value of T_{D0} , material damage initiates. Upon further loading, evolution of damage from initiation to complete failure is defined based on the energy which is dissipated as a result of the damage process, showed as G_i . To identify T_{D0} and G_i values, a three dimensional FE model was constructed in Abaqus according to the actual geometry of the TDCB joint. To reflect the viscoplastic behaviour of the lead-free solder, the identified Anand's constitutive model was implemented in the FE model. A layer of cohesive element with a thickness of 10 μm and unknown cohesive parameters was implemented at the interface of solder and Cu substrates (Fig. 13.2 (a)). Results of simulations were compared with the corresponding experimental results of the TDCB tests and T_{D0} and G_i were tuned in an identification loop in a way to obtain the same load-displacement curves as in Fig. 13.1 (b) and corresponding interfacial crack lengths during propagations for all strain rates simultaneously. Fig 13.2 (b) shows the load-displacement curves obtained by FE simulations in comparison with traction tests, indicating the capability of the identified cohesive parameters ($G_i=0.95$ N/mm, $T_{D0}=69$ MPa) and viscoplastic model for simulation of interfacial fracture in TDCB tests [11Mal].

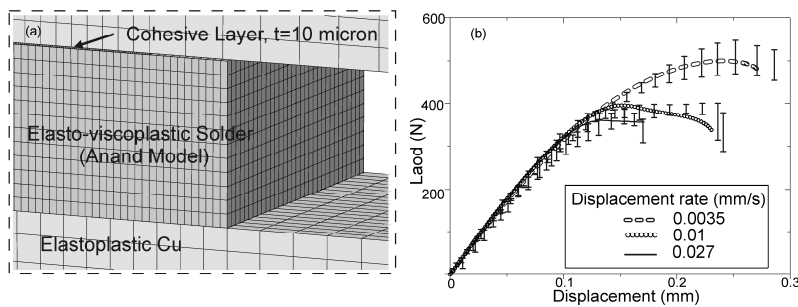


Fig. 13.2: (a) Part of 3D FE model of TDCB showing implemented cohesive layer and mesh quality around solder area. (b) Comparison of load-displacement curves obtained by FE simulations and traction tests of TDCB specimens.

13.1.5 Discussion and Conclusion

Employing the developed FE model, the allotment of the external work during the tests of the TDCB specimens was computed. The results indicated that the main dissipation mechanism at the lowest rate is viscoplastic deformation of solder. However, by increasing the testing rate, the role of the interfacial damage increases significantly. The simulations shows that for the case of loading at the lower rate, considerable inelastic deformation occurred around the middle of bulk solder; so that less deformation were transmitted to the interface and accordingly less traction were generated in the cohesive layer. However, at the higher loading rate, the inelastic deformation developed in the bulk solder is obviously ~~less~~smaller, while the interfacial crack were initiated and propagated (Fig. 13.3). The results of current study indicated that the mutual effects of the viscoplastic behaviour of the bulk solder and the interfacial damage progression are not generally negligible which confirms the necessity of considering both processes in the reliability analyses of solder joints. It was shown that at low strain rate, the viscoplastic solder acts as a stress concentration damper for the interface. In contrary, at a high loading rate, the creep strain rate of the bulk solder becomes negligible compared to the applied strain rate and thus the developed stresses at the interfaces become significantly higher which in turn initiates the development of the interfacial failure.

Comment [A68]: Maybe the correct word is „smaller“?

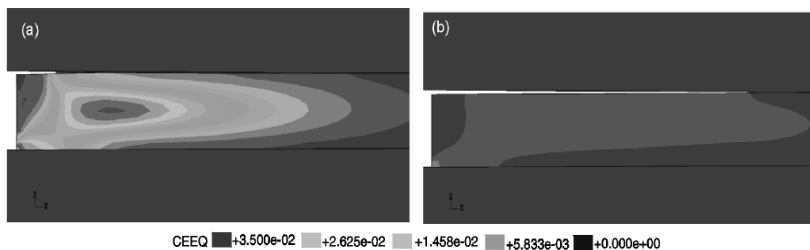


Fig. 13.3: Distribution of equivalent inelastic strain in the solder after 0.15 mm of displacement at the loading rates of (a) 0.0035 mm/s and (b) 0.027 mm/s.

Three dimensional visualization of microstructural evolution in SAC solder and microstructural-based modeling of deformation

13.1.6 Summary

In this part, microstructural evolutions happening due to isothermal ageing in near eutectic SnAgCu solder were visualized and characterized by employing focused-ion-beam/scanning-electron-microscopy and synchrotron X-ray tomography techniques. The obtained 3D microstructural data were used to generate micromechanical FE models. Performing several simulations, representative volume

element (RVE) size was determined and the constitutive behaviour of the eutectic mixture in as-soldered and aged condition was identified. The influences of the microstructural changes on the mechanical properties of the eutectic mixture were and characterized. The homogenized properties were compared with nanoindentation results.

13.1.7 Tomography of intermetallic particles

Three dimensional configurations of Ag_3Sn and Cu_6Sn_5 intermetallics in the eutectic phase of as-soldered and thermally-aged SAC405 were visualized by employing FIB/SEM tomography technique. The method consists of performing serial sectioning by FIB through the selected volume and imaging of the cross-section surface after each milling step by SEM [04Kub].

The Cu_6Sn_5 and Ag_3Sn particles in the 2D images were segmented and visualized in 3D [11Mal2]. Examples of reconstructed images of Ag_3Sn and Cu_6Sn_5 intermetallics in a region of $6 \times 6 \times 6 \mu\text{m}$ of ternary eutectic mixture in as-soldered and aged conditions (144h at 150°C) were shown in Fig. 4 (a) and (b), respectively. While the high resolution (voxel size of $10 \times 10 \times 10 \text{ nm}^3$) of FIB/SEM tomography gives the opportunity to visualize thin and long intermetallics in the eutectic mixture, it is only applicable to the tomography of small volumes. To fully understand the overall 3D morphology of larger phases like $\beta\text{-Sn}$ dendrites and study the coarsening behaviour of intermetallics, synchrotron X-ray tomography was employed. Distribution of coarsened intermetallic precipitated at the boundary of eutectic grains as well as $\beta\text{-Sn}$ dendrites in the aged SAC405 solder were shown in Fig. 13.4 (c).

Comment [A69]: Voxel? It may be useful to explain this term. Is „pixel“ a better word? A voxel is a volumetric pixel. We think it is not necessary to define this.

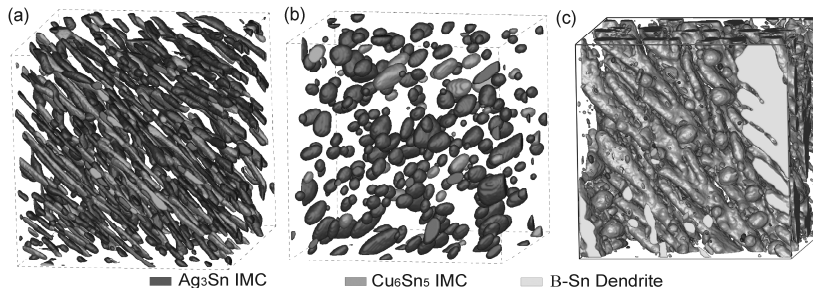


Fig. 13.4: (a) and (b) 3D reconstruction of intermetallics in a cube of $6 \times 6 \times 6 \mu\text{m}$ of eutectic mixture in as-soldered and aged conditions (c) distribution of Sn dendrites and coarsened intermetallics in a cube of $150 \times 150 \times 150 \mu\text{m}$ of aged SAC405.

13.1.8 Quantitative and qualitative analyses of tomography results

The volume, surface, length and diameter of large number of intermetallic particles in the eutectic mixture of SAC405 were determined individually using a set of quantification tools. The results obtained from quantitative analyses were summarized in Table 13.1. The D1, M and D9 related to each specification in the Table 13.1 represent the first decile, median and ninth decile obtained from

descriptive statistical analyses of the corresponding data. The results in Table 13.1 show that both types of particles have obviously needle shape structures in as-soldered condition with the median aspect ratio of 4. In this condition, overall, Ag_3Sn needles are bigger and longer than Cu_6Sn_5 intermetallics. The obtained results show that generally by ageing the aspect ratio of both intermetallics decreases significantly or in other word spheroidizing happens. Accordingly, the particles become like spherical structures after ageing as shown in Fig. 13.4 (b). The results show that the spheroidizing rate is higher in Cu_6Sn_5 intermetallics in comparison with Ag_3Sn needles (Table 13.1). Moreover, the obtained data indicate significant increase of inter-particle spatial distance in both types of needles after ageing (especially Cu_6Sn_5 particles) which can be described by coarsening phenomenon.

The visualization results indicate that intermetallic needles in as-soldered condition follow a preferred solidification direction (Fig. 13.4 (a)). The preferred growth direction of both types of intermetallics in each eutectic grain was determined and compared. The analyses showed that the preferred orientation of needles could be obviously dissimilar in neighbouring grains. Total volume fractions of intermetallics in as-soldered and aged conditions were computed to be 8.5% and 3.7%, respectively [11Mal2].

Table 13.1: Summary of 3D quantitative analyses of intermetallic particles in as-soldered and aged conditions.

Particle type		Ag_3Sn (init.)	Cu_6Sn_5 (init.)	Ag_3Sn (aged)	Cu_6Sn_5 (aged)
Particle density ($\#/\mu\text{m}^3$)		1.6	1.3	1.3	0.3
Particle volume (μm^3)	D1	0.005	0.003	0.005	0.004
	M	0.022	0.012	0.019	0.019
	D9	0.096	0.041	0.058	0.058
Particle length (μm)	D1	0.38	0.33	0.35	0.30
	M	0.82	0.64	0.56	0.52
	D9	3.09	1.59	0.99	0.84
Particle diameter (μm)	D1	0.15	0.12	0.18	0.16
	M	0.22	0.18	0.27	0.26
	D9	0.26	0.24	0.37	0.37
Particle aspect-ratio	D1	1.81	2.05	1.52	1.49
	M	4.06	3.41	1.98	1.79
	D9	15.3	8.09	3.48	3.18
Minimal spatial distance (μm)	D1	0.13	0.14	0.22	0.33

	M	0.26	0.28	0.44	0.70
	D9	0.43	0.50	0.65	1.40

13.1.9 Finite element simulation of deformation in eutectic solder

13.1.9.1 FE model generation

In this step, the tomography results were directly employed to generate a 3D finite element model to simulate the deformation behaviour of the eutectic mixture considering its real microstructural morphology. For this reason, a set of meshing tools was developed by which the 3D tomography results, such as in Fig. 13.4, can be directly meshed, as shown in Fig. 13.5 (a). Ignoring the rate-dependent behaviour of tin matrix, the elastic-rate independent plastic behaviour of different phases were extracted from literature [04Den] and assigned to each microstructure in the finite element model.

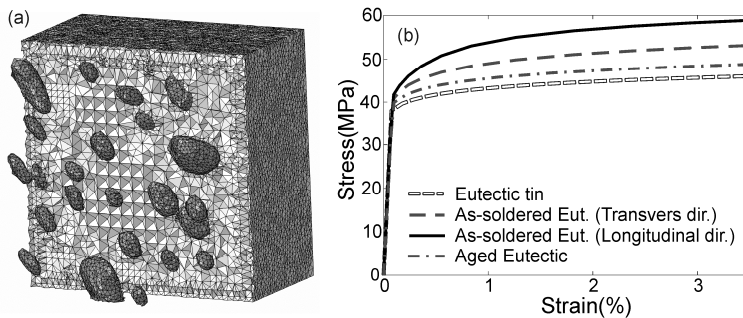


Fig. 13.5: (a) microstructural-based FE model, (b) stress-strain behaviour of pure Sn, as-soldered and thermally aged eutectic mixture obtained by homogenization.

13.1.9.2 Determination of Constitutive behaviour by homogenization

As tomography result showed, the intermetallic particles in each eutectic grain before ageing follow a preferred growth direction. Thus, transverse isotropic deformation behaviour is expected in each grain. To determine the macroscopic constitutive behaviour of the eutectic mixture in the direction of needles as well as transverse directions, firstly, the representative volume element (RVE) size is required to be determined. Comparison of the FE simulation results showed that a cube with the dimension of 3.6x3.6x3.6 μm represents the constitutive behaviour of the mixture i.e. by increasing the volume of interest, the overall response of the cube remains constant. The dark full and dashed lines in Fig. 13.5 (b) indicate the constitutive responses of the as-soldered eutectic mixture in two described directions. Employing the same method, the RVE size and constitutive response of thermally aged eutectic mixture (144h at 150 $^{\circ}\text{C}$) were determined. The dot-dashed line in Fig. 13.5 (b) shows the stress-strain behaviour of aged eutectic solder.

13.1.10 Characterization of mechanical properties of phases by nanoindentation

The elastic-plastic behaviour of the eutectic mixture as well as eutectic tin was experimentally determined by nanoindentation. For this purpose, the indentation tests were performed at the rate of 0.05 mN/s to the maximum load of 15mN (Fig. 13.6 (a)). The elastic modulus and plastic parameters (hardening and initial yield strength) of phases was calculated by Oliver-Pharr and Dao models [[REF2040li.01Dao](#)] respectively. The obtained stress-strain behaviours were shown in Fig. 13.6 (b).

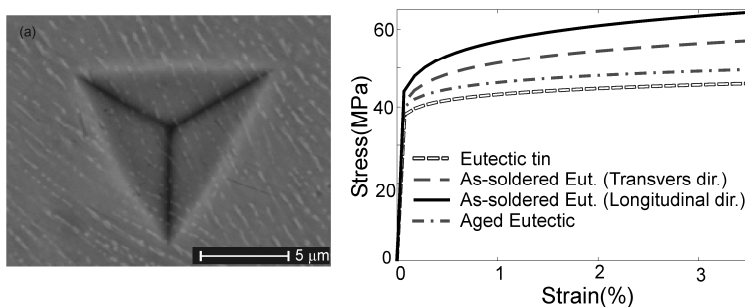


Fig. 13.6: (a) typical indentation point and (b) stress-strain behaviour of phases obtained by nanoindentation tests.

13.1.11 Conclusions

The evolutions in constitutive behaviour of SAC405 solder was determined by employing a microstructural-based FE model and homogenization. The results show that, due to the strengthening effect of intermetallic particles, the ultimate strength of the eutectic mixture (as-soldered and aged) is higher than pure Sn. However, the lower volume fraction of the intermetallics in aged eutectic solders leads to its lower ultimate strength. It was shown that the marked preferred direction in solidified intermetallics induces a significant anisotropy in the mechanical response of as-soldered eutectic mixture. However, the stress-strain behaviours of the thermally aged eutectic mixture of solder joint in different directions are the same. The results of homogenization were showed to be in good agreement with the nanoindentation results.

References

- [09Siv] Sivasubramaniam, V., Galli, M., Cugnoni, J., Janczak-Rusch, J., Botsis, J.: J. Electron. Mater., 2009, **38**, 2122-2131.
- [89Bro] Brown, S.B., Kim, K.H., Anand, L.: Int. J. Plasticity, 1989, **5**, 95-130.
- [97Ber] Beres, W., Koul, K.K., Thamburaj, R.: J. Test. Eval., 1997, **25**, 536-542.
- [11Mal] Maleki, M., Cugnoni, J., Botsis, J.: J. Electron. Mater., 2011, in press.
- [03Cam] Camanho, P.P., Dávila, C.G., de Moura M.F.S.F.: J. Compos. Mater., 2003, **37**, 1415-1438.

Formatted: Font: Bold

Formatted: Font: Bold

[04Kub] Kubis, A.J., Shiflet, G.J., Dunn, D.N., Hull, R.: Metallurgical and Materials Transactions A: Physical Metallurgy and Materials Science, 2004, **35 A**, 1935-1943.

[11Mal2] Maleki, M., Cugnoni, J., Botsis, J.: 2011, in press.

[04Den] Deng, X., Chawla, N., Chawla, K.K., Koopman, M.: Acta Mater., 2004, **52**, 4291-4303.

[04Oli] Oliver, W.C., Pharr, G.M.: J. Mater. Res., 2004, **19**, 3-20.

[01Dao] Dao, M., Chollacoop, N., Van Vliet K.J., Venkatesh, T.A., Suresh, S.: Acta Mater., 2001, **49**, 3899-3918.

Formatted: Font: Bold

Formatted: Dutch (Belgium)

Formatted: Font: Bold

Formatted: Dutch (Belgium)

~~14 Study of mechanical properties of SAC lead-free solders and related soldered joints~~
~~Marian Drienovský, Maroš Martinkovič and Jozef Janovec;~~
~~Slovak University of Technology, Faculty of Materials Science and Technology, Trnava, Slovakia~~
~~Experimental~~
~~For the utilization of lead-free solders it is necessary to know their mechanical properties. Therefore, three eutectic or near-eutectic SAC lead-free solders (Sn-3.5Ag, Sn-0.7Cu, and Sn-3.5Ag-0.7Cu, bulk contents of elements are given in wt. %) and two hypoeutectic solder alloys Sn-3.0Ag-0.5Cu and Sn-0.3Ag-0.7Cu were tested.~~

Comment [A70]: Here are just mechanical properties of SAC alloys – as Trnava group has already 2 chapters here, I would think about cutting this from the book.

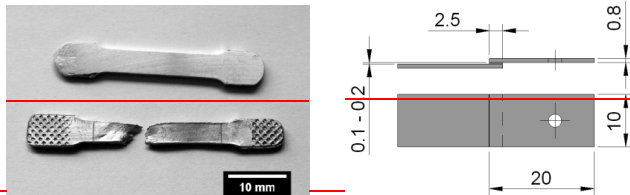
Formatted: Heading 1, Left, Indent: Left: 1 cm, Hanging: 1 cm, Space Before: 0 pt, After: 0 pt

Formatted: Heading 1, None, Indent: Left: 1 cm, Hanging: 1 cm

Formatted: Heading 1, Left, Indent: Left: 1 cm, Hanging: 1 cm, Space Before: 0 pt, After: 0 pt

~~The solder alloys Sn-3.5Ag, Sn-0.7Cu, and Sn-3.5Ag-0.7Cu were prepared from Sn, Ag, and Cu of the 99.99 wt.% purity by melting in induction furnace. The other two solders—(Sn-3.0Ag-0.5Cu, Sn-0.3Ag-0.7Cu)—were bought from commercial seller. The melting point of each solder was verified experimentally using DSC. Two kinds of specimens were prepared for mechanical testing, bulk solders and solder joints. Bulk solder specimens were produced by casting of solder alloys to reach dimensions of 40x5x2 mm. Then they were machined into the shape showed in Fig. 14.1a. Cross section areas of the bulk solder specimens were about 8 mm² and the gauge length 18 mm. Free surfaces of the specimens were carefully polished before mechanically tested to determine values of tensile strength [MPa], ductility [%], and toughness (energy of fracture) [m]/mm³. Solder joints for the determination of shear strength [MPa] were prepared between two copper sheets to obtain the final dimension of joint approximately 10x2.5x0.2 mm (Fig. 14.1b). Copper sheets of 20 x 10 x 0.8 mm were cut, shortly polished on P1200 SiC abrasive paper and cleaned in alcohol. To prepare the soldered joints, the solder alloy and the flux were placed between two copper sheets and heated on the hot plate. To ensure immobility during the soldering process a special facility made from aluminium was used. Soldering temperatures exceeded the liquid temperatures of 40–50°C for particular alloys and the soldering time was about 10 seconds. Two kinds of fluxes were used at the soldering; the corrosive water soluble flux based on zinc chloride and ammonium chloride and the KOH containing no-clean flux. The former is suitable for soldering copper tubes for potable water and the latter is suitable for the wave soldering.~~

~~(a) (b)~~



- ~~Fig. 14.1: Bulk solder specimen before and after tensile test (a); scheme showing soldered lap-shear joint (b)~~
- ~~For testing of tensile strength and shear strength a FPZ 100/1 Universal Testing Machine was used. All the specimens were tested at room temperature using strain (deformation) rate of 2 mm/min. Additionally, some solder joints were aged for 200 hours at 150°C. At least 5 specimens per type and alloy were tested.~~
- ~~Mechanical properties of bulk solders~~
- ~~The values of Ultimate Tensile Strength [MPa] of selected solders (Fig. 14.2) were determined by dividing the maximum force [N] applied in the tensile test by the original cross-section area of the tested bulk solder specimen [mm²]. The testing machine drew Force-Extension diagrams (N-mm), the values of relative toughness [m]/mm³ (Fig. 14.3a) were determined as area under the recorded loading curve. The ductility (Fig. 14.3b) was determined from gauge length before and after the test.~~
- ~~The highest values of UTS were determined for the Sn-9Zn alloy (Fig. 14.2) having also the highest level of alloying. On the other hand, the low-alloy ternary Sn-0.3Ag-0.7Cu solder showed the worst mechanical properties (Figs. 14.2 and 14.3).~~

Formatted: Heading 1, None, Indent: Left: 1 cm, Hanging: 1 cm

Formatted: Heading 1, Left, Indent: Left: 1 cm, Hanging: 1 cm, Space Before: 0 pt, After: 0 pt

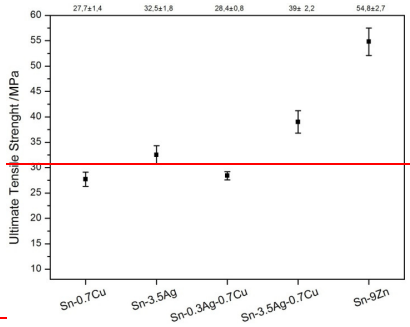


Fig. 14.2: Values of Ultimate Tensile Strength for selected bulk solder specimens (currently investigated and earlier tested [1, 2])

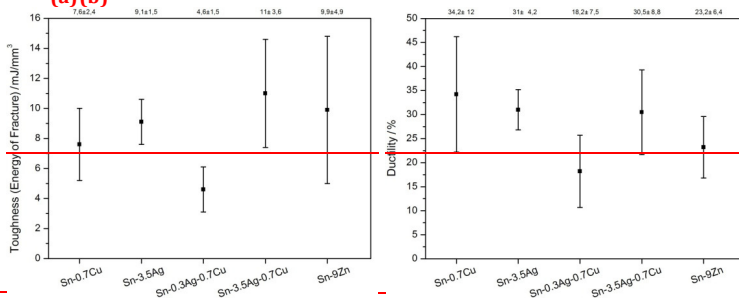


Fig. 14.3: Calculated Toughness (a) and Ductility (b) for selected bulk solder specimens (currently investigated and earlier tested [1, 2])

Mechanical properties of solder joints

Comment [A71]: The legend is too small, not readable

Comment [A72]: Wrong format of the Reference

Comment [A73]: dtto

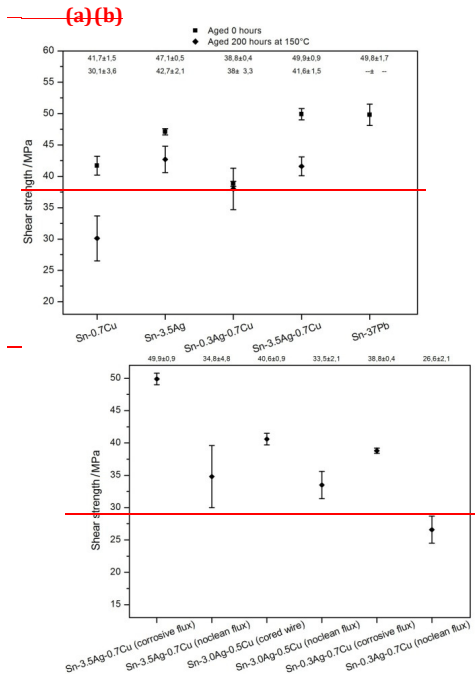
Comment [A74]: wrong format of reference

Formatted: Heading 1, Indent: Left: 1 cm, Hanging: 1 cm

Formatted: Heading 1, None, Indent: Left: 1 cm, Hanging: 1 cm

~~Mechanical testing of soldered joints was aimed at the measurement of shear strength [MPa]. Soldered joints made with corrosive water soluble flux were aged for 200 hours at 150°C (Fig. 14.4a). After ageing the specimens exhibited lower values of shear strength and a wider intermetallic layer between the copper substrate and the solder [06Sun,06Li,09Liu,11Hod]. Some solder joints with ternary lead-free solder alloys were made using no-clean type of flux. The comparison of values of shear strength for solder joints prepared using different fluxes is illustrated in Fig. 14.4. The use of no-clean type of flux lead to the significant decrease in shear strength of solder joints, but it was partly compensated with less residues of flux after soldering [98Yan,02Doy].~~

Formatted: Heading 1, Left, Indent: Left: 1 cm, Hanging: 1 cm, Space Before: 0 pt, After: 0 pt



~~Fig. 14.4: Values of shear strength for original and aged soldered joints prepared using the corrosive water soluble flux (a) or the no-clean flux (b)~~

~~References~~

- ~~[10Mar] Martinkovič, M., Drienovský, M.: Acta Metallurgica Slovaca, 2010, 1, 277-280.~~
- ~~[10Dri] Drienovský, M., Martinkovič, M., Janovec, J.: International Doctoral Seminar, 2010, 119-125.~~
- ~~[06Sun] Sundelin, J. J., Nurmi, S. T., Lepistö, T. K., Ristolainen, E. O.: Mater. Sci. Eng., 2006, A 420, 55-62.~~
- ~~[06Li] Li, G. Y., Shi, X. Q.: Trans. Nonferrous Met. Soc. China, 2006, 16, 739-743.~~
- ~~[09Liu] Liu, P., Yao, P., Liu, J.: J. Alloys Compd., 2009, 486, 474-479.~~
- ~~[11Hod] Hodúlová, E., Palcut, M., Lechovič, E., Šimeková, B., Ulrich K.: J. Alloys Compd., 2011, 509, 7052-7059.~~
- ~~[98Yan] Yang, C. J., Srihari, K., DiLella, J.: Computers Ind. Engng., 1998, 35, 57-60.~~
- ~~14 [02Doy] Doyle, C., Brown, N., Bardizeh, M.: Metal Finishing, 2002, 100, 10-12.~~

Formatted: Heading 1, None, Indent: Left: 1 cm, Hanging: 1 cm

Formatted: Heading 1, Indent: Left: 1 cm, Hanging: 1 cm, Space Before: 0 pt, Add space between paragraphs of the same style, Tab stops: Not at 1,6 cm